2020

THE PION FORM FACTOR AND MOMENTUM AND ANGULAR MOMENTUM FRACTIONS OF THE PROTON IN LATTICE QCD

Gen Wang
University of Kentucky, genwang27@gmail.com
Author ORCID Identifier:
https://orcid.org/0000-0003-3104-1211
Digital Object Identifier: https://doi.org/10.13023/etd.2020.406

STUDENT AGREEMENT:

I represent that my thesis or dissertation and abstract are my original work. Proper attribution has been given to all outside sources. I understand that I am solely responsible for obtaining any needed copyright permissions. I have obtained needed written permission statement(s) from the owner(s) of each third-party copyrighted matter to be included in my work, allowing electronic distribution (if such use is not permitted by the fair use doctrine) which will be submitted to UKnowledge as Additional File.

I hereby grant to The University of Kentucky and its agents the irrevocable, non-exclusive, and royalty-free license to archive and make accessible my work in whole or in part in all forms of media, now or hereafter known. I agree that the document mentioned above may be made available immediately for worldwide access unless an embargo applies.

I retain all other ownership rights to the copyright of my work. I also retain the right to use in future works (such as articles or books) all or part of my work. I understand that I am free to register the copyright to my work.

REVIEW, APPROVAL AND ACCEPTANCE

The document mentioned above has been reviewed and accepted by the student's advisor, on behalf of the advisory committee, and by the Director of Graduate Studies (DGS), on behalf of the program; we verify that this is the final, approved version of the student's thesis including all changes required by the advisory committee. The undersigned agree to abide by the statements above.

Gen Wang, Student

Dr. Keh-Fei Liu, Major Professor

Dr. Christopher Crawford, Director of Graduate Studies

THE PION FORM FACTOR AND MOMENTUM AND ANGULAR MOMENTUM FRACTIONS OF THE PROTON IN LATTICE QCD

DISSERTATION

A dissertation submitted in partial
fulfillment of the requirements for
the degree of Doctor of Philosophy
at the University of Kentucky

By
Gen Wang
Lexington, Kentucky

Director: Dr. Keh-Fei Liu, Professor of Physics and Astronomy
Lexington, Kentucky

2020

https://orcid.org/0000-0003-3104-1211

ABSTRACT OF DISSERTATION

THE PION FORM FACTOR AND MOMENTUM AND ANGULAR MOMENTUM FRACTIONS OF THE PROTON IN LATTICE QCD

Lattice Quantum Chromodynamics (QCD) provides a way to have a precise calculation and a new way of understanding the hadrons from first principles. From this perspective, this dissertation focuses first on a precise calculation of the pion form factor using overlap fermions on six ensembles of 2+1-flavor domain-wall configurations generated by the RBC/UKQCD collaboration with pion masses varying from 137 to 339 MeV. Taking advantage of the fast Fourier transform, low-mode substitution (LMS) and the multi-mass algorithm to access many combinations of source and sink momenta, we have done a simulation with various valence quark masses and with a range of space-like Q^2 up to 1.0 GeV^2. With a z-expansion fitting of our data, we find the pion mean square charge radius to be $\langle r^2 \rangle_\pi = 0.433(9)(13)\text{fm}^2$, which agrees well with the experimental result, and includes the systematic uncertainties from chiral extrapolation, lattice spacing, and finite volume dependence. We also find that $\langle r_\pi^2 \rangle$ depends on both the valence and sea quark masses strongly and predict the pion form factor up to $Q^2 = 1.0$ GeV^2 which agrees with experiments very well. The second topic is the lattice calculation of proton momentum and angular momentum fractions. As confirmed from experiment and lattice QCD calculation, the total helicity contribution from quarks is about $\sim 30\%$ of the proton spin. Determination of the rest of the contributions from quarks and gluons to the proton spin is a challenging and important problem. On the lattice side, one way to approach this problem is to use the nucleon matrix element of the traceless, symmetric energy-momentum tensor (EMT) to determine the momentum and angular momentum distributions of up, down, strange and glue constituents. Since the EMT of each parton species are not separately conserved, we summarized their final angular momentum fractions by considering mixing and non-perturbative renormalization at $\overline{\text{MS}}(\mu = 2$ GeV) and use the momentum and angular momentum sum rules to normalize them. In order to have a complete picture of these quantities, we have calculated both the connected and disconnected insertions with an extrapolation to physical pion mass. We also use various techniques to improve the results, such as LMS and new three-point function contractions using fast Fourier transform for the connected insertions.

KEYWORDS: Lattice QCD, Hadron Structure

Gen Wang

September 9, 2020

THE PION FORM FACTOR AND MOMENTUM AND ANGULAR MOMENTUM FRACTIONS OF THE PROTON IN LATTICE QCD

By
Gen Wang

Keh-Fei Liu
Director of Dissertation

Christopher Crawford
Director of Graduate Studies

September 9, 2020
Date

Dedicated to my parents, sister and my beloved Zhaohui.

ACKNOWLEDGMENTS

I would like to thank various people for their help, advice and guidance to my PhD study. It would be an impossible task for me without their support. First, I would like express my deep gratitude to my adviser Prof. K. F. Liu for providing endless support and guidance. His continuous advising and training kept me in focus and on the right track every day. He also provided me a lot of opportunities to attend summer schools and conferences around the world which helped in shaping my understanding of physics. It has been a great pleasure to work with him. I would like also to thank Prof. T. Draper for his helpful hints and detailed suggestions. His thorough reading of my presentations and drafts taught my the way to have scientific discussions and communications. I gratefully thank Dr. Yibo Yang who taught me Lattice QCD simulations right from the beginning, and his efforts on tutorial training and suggestions helped me throughout my PhD research. I have learned a lot of knowledge and experience from Dr. Jian Liang. He is always so kind about my naive questions every day and explains to me patiently until I fully understand. I thank Dr. Raza Sabbir Sufian for his helpful explanations and career suggestions. I wish to acknowledge the suggestions, corrections, and encouragements from my other committee members, Prof. W. Korsch and Prof. C. Srinivasan. In addition, I have also benefited a lot from constructive discussions about physics ideas and algorithms with Luchang Jin. At the end, I wish to thank my parents, my sister and my beloved Zhaohui who are always willing to share my complaints and frustrations. Their assistance and encouragement supports me to pursue my interests.

TABLE OF CONTENTS

LIST OF TABLES

LIST OF FIGURES

Chapter 1 Introduction

Quarks and color degrees of freedom were introduced to study hadron structure and the strong interaction around sixty years ago. Later on, Quantum Chromodynamics (QCD), an $SU(3)$ gauge theory, formulated with quarks and gluons as the basic degrees of freedom to describe the hadronic interactions. Since the strong coupling constant of QCD at large energy scales is small which is known as asymptotic freedom, perturbation theory has been successfully predicting phenomena involving large momentum transfers. Whereas, at small energy scales of the hadron world, the coupling constant is of order unity and the physical properties of hadrons are governed by nonpeturbative effects such as confinement. Due to this reason, it is still challenging to quantify the hadron structure. On the other hand, with more than three decades of developments, lattice QCD has been proven to be a reliable tool to calculate the hadronic spectrum and matrix elements from first principles. Moreover, lattice QCD is also able to tackle problems like QCD at finite temperature, confinement, chiral symmetry breaking and topology.

The discretized Euclidean space time of lattice QCD provides an ultraviolet cutoff at π/a to regularize the theory and remove infinities, with a the lattice spacing. And in the continuum limit $a \to 0$, the renormalized physical quantities should be finite which guaranties a well defined limit. The successful discretization of gauge theories in Euclidean space time enables simulation of QCD on a computer using Monte Carlo integration of the Euclidean path integral. Lattice QCD results have had great achievements in controlling its statistical and systematic errors with recent advancements of numberical analysis and computational technology. And these results have already served as basic inputs for a lot of phenomenological studies such as quark masses, CKM matrix elements, low energy constants and form factors.

In this dissertation, we will focus on two topics in hadronic physics. The first one is the calculation of the pion form factor using overlap fermions on six ensembles of 2+1-flavor domain-wall configurations with pion masses varying from 137 to 339 MeV. We will report on the pion form factor up to $Q^2 = 1.0$ GeV^2 and the charge radius of the pion $\langle r_\pi^2 \rangle$, both at the physical limit (physical pion mass, continuum and infinite volume limit). Since the experimental determination of $\langle r_\pi^2 \rangle$ from πe scattering is very precise and the pion is relatively simple to handle on the lattice, it provides a stringent test for lattice QCD calculations to demonstrate complete control over the statistical and systematic errors in estimates of the relevant pionic matrix element in order to enhance confidence in their reliability to calculate other hadronic matrix elements where lattice calculations can produce error estimates smaller than those of experiments or make useful and timely predictions.

The quark model which successfully describes a lot of properties of hadrons predicted that all the proton spin is carried by its three valence quarks. Whereas, as confirmed from experiment and lattice QCD calculations, the total helicity contribution from quarks is just about $\sim 30\%$ of the proton spin of $\frac{1}{2}\hbar$. Thus, determination of the remaining contributions from quarks and gluons to the nucleon (i.e., proton or

neutron) spin is a challenging and important problem which is the second topic of this dissertation. We will use overlap fermions on a $32^3 \times 64$ domain-wall lattice at near the physical pion mass to calculate the nucleon matrix element of the traceless, symmetric energy-momentum tensor (EMT) in order to have a complete decomposition of the angular momentum fractions of the nucleon. The final renormalized results are reported in the last section.

Chapter 2 QCD on the lattice

2.1 Path integrals on the lattice

In order to calculate Quantum Chromodynamics (QCD) on a space-time lattice, we use a path integral representation analytically continued to imaginary times, $t \to -ix_4$, in which x_4 is a real number. The vacuum expectation of an operator $\mathcal{O}$ in the continuum Euclidean space is

$$\langle \mathcal{O} \rangle = \frac{\int \mathcal{D}[\psi, \bar{\psi}] \psi \mathcal{D}A \mathcal{O}(\psi, \bar{\psi}, A) \exp^{-(S_G[A] + S_F[\psi, \bar{\psi}, A])}}{\int \mathcal{D}[\psi, \bar{\psi}] \mathcal{D}A \exp^{-(S_G[A] + S_F[\psi, \bar{\psi}, A])}}, \tag{2.1.1}$$

where $S_G[A]$ is the gauge action and $S_F[\psi, \bar{\psi}, A]$ is the fermion action. The gauge fields $A_\mu(x)$ are defined as

$$A_\mu(x) = \sum_{i=1}^{8} A_\mu^i(x) T_i, \tag{2.1.2}$$

where $A_\mu^i(x)$ are real-valued fields, $T_i,\ i = 1, \ldots, 8$ are a basis of traceless hermitian 3×3 matrices which are the generators of the $SU(3)$ group satisfies the commutation relations

$$[T_i, T_j] = i f_{ijk} T_k, \tag{2.1.3}$$

in which f_{ijk} are the structure constants. These generators are given by $T_i = \frac{1}{2}\lambda_i$ with the Gell-Mann matrices λ_i

$$\begin{aligned}
\lambda_1 &= \begin{pmatrix} 0 & 1 & 0 \\ 1 & 0 & 0 \\ 0 & 0 & 0 \end{pmatrix}, \lambda_2 = \begin{pmatrix} 0 & \text{-i} & 0 \\ \text{i} & 0 & 0 \\ 0 & 0 & 0 \end{pmatrix}, \lambda_3 = \begin{pmatrix} 1 & 0 & 0 \\ 0 & \text{-1} & 0 \\ 0 & 0 & 0 \end{pmatrix}, \\
\lambda_4 &= \begin{pmatrix} 0 & 0 & 1 \\ 0 & 0 & 0 \\ 1 & 0 & 0 \end{pmatrix}, \lambda_5 = \begin{pmatrix} 0 & 0 & \text{-i} \\ 0 & 0 & 0 \\ \text{i} & 0 & 0 \end{pmatrix}, \lambda_6 = \begin{pmatrix} 0 & 0 & 0 \\ 0 & 0 & 1 \\ 0 & 1 & 0 \end{pmatrix}, \\
\lambda_7 &= \begin{pmatrix} 0 & 0 & 0 \\ 0 & 0 & \text{-i} \\ 0 & \text{i} & 0 \end{pmatrix}, \lambda_8 = \frac{1}{\sqrt{3}} \begin{pmatrix} 1 & 0 & 0 \\ 0 & 1 & 0 \\ 0 & 0 & \text{-2} \end{pmatrix}.
\end{aligned} \tag{2.1.4}$$

Using these matrices, we define the field strength tensor as $F_{\mu\nu}(x) = \sum_{i=1}^{8} F_{\mu\nu}^i(x) T_i$ with

$$F_{\mu\nu}^i = \partial_\mu A_\nu^i - \partial_\nu A_\mu^i - f_{ijk} A_\mu^j A_\nu^k. \tag{2.1.5}$$

Then the gauge action $S_G[A]$ can be evaluated as

$$S_G(A) = \frac{1}{2g_0^2} \mathrm{Tr} \int d^4x F_{\mu\nu} F_{\mu\nu}, \tag{2.1.6}$$

with g_0 the bare coupling constant.

The fermion action, $S_F[\bar{\psi}, \psi, A]$, is given by the expression

$$S_F[\bar{\psi}, \psi, A] = \int d^4x \bar{\psi}(x)(\gamma_\mu \mathcal{D}_\mu + m)\psi(x), \tag{2.1.7}$$

where $\mathcal{D}_\mu$ is the covariant derivative

$$\mathcal{D}_\mu = \partial_\mu - iA_\mu, \tag{2.1.8}$$

which ensures local $SU(3)$ symmetry defined as

$$\begin{aligned} A_\mu(x) \to A'_\mu(x) &= \Omega(x)A_\mu(x)\Omega(x)^\dagger + i(\partial_\mu \Omega(x))\Omega(x)^\dagger \\ \mathcal{D}_\mu \to \mathcal{D}'_\mu(x) &= \partial_\mu + iA'_\mu(x) = \Omega(x)D_\mu(x)\Omega(x)^\dagger \end{aligned} \tag{2.1.9}$$

with $\Omega(x)$ the $SU(3)$ matrix which satisfies $\Omega(x)^\dagger = \Omega(x)^{-1}$ and $\mathrm{Det}[\Omega(x)] = 1$.

The Euclidean γ matrices are hermitian, $\gamma_\mu^\dagger = \gamma_\mu$, and satisfy the commutation relations $\{\gamma_\mu, \gamma_\nu\} = 2\delta_{\mu\nu}$. This dissertation adopts the Euclidean Pauli-Sakurai γ matrices convention as

$$\begin{aligned} \gamma_1 &= \begin{pmatrix} 0 & 0 & 0 & -\mathrm{i} \\ 0 & 0 & -\mathrm{i} & 0 \\ 0 & \mathrm{i} & 0 & 0 \\ \mathrm{i} & 0 & 0 & 0 \end{pmatrix}, \gamma_2 = \begin{pmatrix} 0 & 0 & 0 & -1 \\ 0 & 0 & 1 & 0 \\ 0 & 1 & 0 & 0 \\ -1 & 0 & 0 & 0 \end{pmatrix}, \gamma_3 = \begin{pmatrix} 0 & 0 & -\mathrm{i} & 0 \\ 0 & 0 & 0 & \mathrm{i} \\ \mathrm{i} & 0 & 0 & 0 \\ 0 & -\mathrm{i} & 0 & 0 \end{pmatrix}, \\ \gamma_4 &= \begin{pmatrix} 1 & 0 & 0 & 0 \\ 0 & 1 & 0 & 0 \\ 0 & 0 & -1 & 0 \\ 0 & 0 & 0 & -1 \end{pmatrix}, \gamma_5 = \begin{pmatrix} 0 & 0 & -1 & 0 \\ 0 & 0 & 0 & -1 \\ -1 & 0 & 0 & 0 \\ 0 & -1 & 0 & 0 \end{pmatrix}. \end{aligned} \tag{2.1.10}$$

In order to numerically solve the system, which has an infinite number of degrees of freedom in the continuum, we discretize the gauge and fermion fields on a cubic lattice to reduce the degrees of freedom. This introduces a cut-off in momentum, i.e., the largest momentum is $p = \frac{\pi}{a}$, where a is the lattice spacing. This will regulate the field theory and allows for renormalization.

2.2 Gauge fields on the lattice

We replace gauge fields $A_\mu(x)$ with $SU(3)$ matrices $U_\mu(n)$ (gauge links)

$$U_\mu(n) \equiv e^{iaA_\mu(n+\frac{\hat{\mu}}{2})}. \tag{2.2.1}$$

Under a gauge transformation $\Omega(n)$, the gauge links transform as

$$U_\mu(n) \to U'_\mu(n) = \Omega(n)U_\mu(n)\Omega(n+\hat{\mu})^\dagger, \tag{2.2.2}$$

in which $U_\mu(n)$ connects site n and site $n+\hat{\mu}$ to preserve the local $SU(3)$ transformation in Eq. (2.2.2), where $\hat{\mu}$ is a unit vector in the x_μ direction, a is the lattice

spacing between two nearest neighbouring sites and n is the integer label of position $x = an$.

The gauge links in the reverse direction is $U_{-\mu}(n+\hat{\mu}) = U_\mu^\dagger(n)$. The simplest gauge invariant and nontrivial closed loop on the lattice is plaquette $U_{\mu\nu}(n)$,

$$U_{\mu\nu}(n) = \mathrm{Tr}\left[U_\mu(n)U_\nu(n+\hat{\mu})U_\mu(n+\hat{\nu})^\dagger U_\nu(n)^\dagger\right]. \tag{2.2.3}$$

In order to connect $U_{\mu\nu}(n)$ with the continuum theory, we perform a Taylor expansion of $U_{\mu\nu}(n)$ by using the Campbell-Hausdorff formula [19, 20]

$$\exp(A)\exp(B) = \exp\left(A + B + \frac{1}{2}[A,B]\right), \tag{2.2.4}$$

to obtain

$$\begin{aligned} U_{\mu\nu}(n) =& \exp\Bigg(iaA_\mu(n+\frac{\hat{\mu}}{2}) + iaA_\nu(n+\hat{\mu}+\frac{\hat{\nu}}{2}) - iaA_\mu(n+\hat{\nu}+\frac{\hat{\mu}}{2}) - iaA_\nu(n+\frac{\hat{\nu}}{2}) \\ &- \frac{a^2}{2}[A_\mu(n+\frac{\hat{\mu}}{2}), A_\nu(n+\hat{\mu}+\frac{\hat{\nu}}{2})] - \frac{a^2}{2}[A_\mu(n+\hat{\nu}+\frac{\hat{\mu}}{2}), A_\nu(n+\frac{\hat{\nu}}{2})] \\ &+ \frac{a^2}{2}[A_\mu(n+\frac{\hat{\mu}}{2}), A_\mu(n+\hat{\nu}+\frac{\hat{\mu}}{2})] + \frac{a^2}{2}[A_\nu(n+\hat{\mu}+\frac{\hat{\nu}}{2}), A_\nu(n+\frac{\hat{\nu}}{2})] \\ &+ \frac{a^2}{2}[A_\mu(n+\frac{\hat{\mu}}{2}), A_\nu(n+\frac{\hat{\nu}}{2})] + \frac{a^2}{2}[A_\nu(n+\hat{\mu}+\frac{\hat{\nu}}{2}), A_\mu(n+\hat{\nu}+\frac{\hat{\mu}}{2})] + \mathcal{O}(a^3)\Bigg). \end{aligned} \tag{2.2.5}$$

Expanding the gauge fields in the above formula around $n + \frac{\hat{\mu}+\hat{\nu}}{2}$ using

$$A_\mu(n+\frac{\hat{\mu}}{2}) = A_\mu(n+\frac{\hat{\mu}+\hat{\nu}}{2}) - \frac{1}{2}a\partial_\nu A_\mu(n+\frac{\hat{\mu}+\hat{\nu}}{2}) + \mathcal{O}(a^2) \tag{2.2.6}$$

in which $\partial_\nu A_\mu = \frac{\partial A_\mu}{\partial x_\nu}$ and defining $n' = n + \frac{\hat{\mu}+\hat{\nu}}{2}$, Eq. (2.2.5) reduces to

$$\begin{aligned} U_{\mu\nu}(n) &= \exp[ia^2(\partial_\mu A_\nu(n') - \partial_\nu A_\mu(n') + i[A_\mu(n'), A_\nu(n')]) + \mathcal{O}(a^3)] \\ &= \exp(ia^2 F_{\mu\nu}(n') + \mathcal{O}(a^3)) \end{aligned} \tag{2.2.7}$$

Thus the gauge action can be written with the real parts of the plaquette

$$\frac{1}{2}\left(U_{\mu\nu}(n) + U_{\mu\nu}^\dagger(n)\right), \tag{2.2.8}$$

as

$$\begin{aligned} S_G[U] &= \frac{6}{g_0^2}\sum_n\sum_{\mu<\nu}\mathrm{Tr}\frac{1}{3}\left[1 - \frac{1}{2}\left(U_{\mu\nu}(n) + U_{\mu\nu}^\dagger(n)\right)\right] \\ &= \frac{a^4}{2g_0^2}\sum_n\sum_{\mu\nu}\mathrm{Tr}[F_{\mu\nu}(n+\frac{\hat{\mu}+\hat{\nu}}{2})^2] + \text{terms higher order in } a, \end{aligned} \tag{2.2.9}$$

which gives the continuum action up to discretization errors. The lattice calculations are mostly presented in terms of couplings constant $\beta = \frac{6}{g_0^2}$ which is the only variable in the gauge action part.

2.3 Fermions on the lattice

A "naive" discretization of the fermion on the lattice with hermicity is

$$\partial_\mu \psi(x) \to \frac{1}{2a}[\psi(n+\hat{\mu}) - \psi(n-\hat{\mu})], \tag{2.3.1}$$

which leads to the fermion action

$$\begin{aligned} & S_F[\bar{\psi}, \psi, U] \\ & = a^4 \sum_n \bar{\psi}(n) \left(\sum_{\mu=1}^{4} \gamma_\mu \frac{U_\mu(n)\psi(n+\hat{\mu}) - U_{-\mu}(n)\psi(n-\hat{\mu})}{2a} + m\psi(n) \right) \\ & = a^4 \sum_{m,n} \bar{\psi}(m) D_{m,n} \psi(n), \end{aligned} \tag{2.3.2}$$

where

$$D_{m,n} = m\delta_{m,n} + \frac{1}{2a} \sum_{\mu=1}^{4} \gamma_\mu \left[U_\mu(m)\delta_{m,n-\hat{\mu}} - U_{-\mu}(m)\delta_{m,n+\hat{\mu}} \right]. \tag{2.3.3}$$

However, this "naive" discretization will give rise to $2^d = 16$ flavors rather than one lattice quark flavor in the continuum. This is called the "fermion doubling problem" as 15 unphysical poles arise at the boundaries of the Brillouin zone. In order to remove the doublers, Wilson [21] proposed a possible solution by adding an extra second derivative term which vanishes in the continuum limit as

$$-raD_\mu^2 \psi(n) = -ra \sum_{\mu=1}^{4} \frac{1}{2a^2} [U_\mu(n)\psi(n+\hat{\mu}) - 2\psi(n) + U_{-\mu}(n)\psi(n-\hat{\mu})], \tag{2.3.4}$$

in which r is the "Wilson coefficient", which is normally set to 1. Then the Wilson fermion action is

$$\begin{aligned} S_F^W &= a^4 \sum_{m,n} \bar{\psi}(m) D_{m,n}^W \psi(n). \\ D_{m,n}^W &= (m + r\frac{4}{a})\delta_{m,n} - \frac{1}{2a} \sum_{\mu=1}^{4} [(r-\gamma_\mu)U_\mu(m)\delta_{m,n-\hat{\mu}} + (r+\gamma_\mu)U_{-\mu}(m)\delta_{m,n+\hat{\mu}}]. \end{aligned} \tag{2.3.5}$$

Under a conventional rescaling of quark fields $\psi \to \frac{1}{\sqrt{2\kappa}}\psi$ with $\kappa = \frac{1}{2(4r+ma)}$, $D_{m,n}^W$ is

$$D_{m,n}^W = \frac{1}{a}\delta_{m,n} - \kappa \frac{1}{a} \sum_{\mu=1}^{4} [(r-\gamma_\mu)U_\mu(m)\delta_{m,n-\hat{\mu}} + (r+\gamma_\mu)U_{-\mu}(m)\delta_{m,n+\hat{\mu}}]. \tag{2.3.6}$$

By analysing the Wilson Dirac operator in momentum space, it can be shown that the unphysical poles have an extra contribution $2/a$ which becomes very heavy and decouples from the theory in the limit $a \to 0$. Whereas the additional term in

Eq.(2.3.4) explicitly breaks the chiral symmetry of the theory at the zero mass limit. A chiral rotation on the fermion fields is defined as

$$\psi \to \psi' = e^{i\alpha\gamma_5}\psi, \bar{\psi} \to \bar{\psi}' = \bar{\psi}e^{i\alpha\gamma_5}. \tag{2.3.7}$$

It is easy to show that the massless QCD Lagrangian $\mathcal{L} = \bar{\psi}\gamma_\mu\mathcal{D}_\mu\psi$ is invariant under the chiral rotation because of the anti-commutation of γ_μ and γ_5 as $\{\gamma_\mu, \gamma_5\} = 0$. This is equivalent to having the massless Dirac operator $\mathcal{D}$ satisfy

$$\mathcal{D}\gamma_5 + \gamma_5\mathcal{D} = 0. \tag{2.3.8}$$

However, the additional term of Wilson fermion in Eq.(2.3.4) does not anti-commute with γ_5. In other words, the massless Wilson Dirac operator $\mathcal{D}^W$ is not chiral since

$$\mathcal{D}^W\gamma_5 + \gamma_5\mathcal{D}^W = -2raD_\mu^2\gamma_5. \tag{2.3.9}$$

In continuum theory, chiral symmetries are important in the spectrum and phenomenology of the standard model. In order to have chiral symmetry on the lattice, Ginsparg and Wilson [22] proposed a lattice version of Eq. (2.3.8) as

$$\mathcal{D}\gamma_5 + \gamma_5\mathcal{D} = a\mathcal{D}\gamma_5\mathcal{D}, \tag{2.3.10}$$

with the associated chiral rotation at finite lattice spacing a as

$$\psi \to \psi' = e^{i\alpha\gamma_5(\mathbb{1}-\frac{a}{2}\mathcal{D})}\psi, \bar{\psi} \to \bar{\psi}' = \bar{\psi}e^{i\alpha(\mathbb{1}-\frac{a}{2}\mathcal{D})\gamma_5}. \tag{2.3.11}$$

A solution of the Ginsparg-Wilson equation [23] is the overlap operator defined as

$$\mathcal{D}_{ov} = \frac{1}{a}(1 + \gamma_5\text{sign}(H_w(\rho))), H_w(\rho) \equiv \gamma_5\mathcal{D}_w(\rho), \tag{2.3.12}$$

where $\text{sign}(H_w) = H_w/\sqrt{H_w^2}$ is the matrix sign function which can be approximated through the Chebyshev polynomials [23], and H_w is the hermitian Wilson Dirac operator with a negative mass parameter $\rho = -(\frac{1}{2\kappa} - 4)$, in which $\kappa_c < \kappa < 0.25$ with κ_c the critical hopping parameter obtained by a linear extrapolation to the zero pion mass. We use $\kappa = 0.2$ in our calculation which corresponds to $\rho = 1.5$ so that there are no zero modes in H_w. Since H_w is hermitian, the matrix sign function is well-defined through the spectral theorem. In order to show the overlap operator D_{ov} satisfies the Ginsparg-Wilson relation in Eq (2.3.10), we first prove the following relation,

$$\begin{aligned}
\mathcal{D}_{ov}\mathcal{D}_{ov}^\dagger &= \frac{1}{a^2}(1 + \gamma_5\text{sign}(H_w))(1 + \text{sign}(H_w)\gamma_5) \\
&= \frac{1}{a^2}(1 + \gamma_5\text{sign}(H_w) + \text{sign}(H_w)\gamma_5 + 1) \\
&= \frac{1}{a}(\mathcal{D}_{ov} + \mathcal{D}_{ov}^\dagger).
\end{aligned} \tag{2.3.13}$$

Also, we have

$$\mathcal{D}_{ov}^\dagger = 1 + \text{sign}(H_w(\rho))\gamma_5^\dagger = \gamma_5\mathcal{D}_{ov}\gamma_5. \tag{2.3.14}$$

Combining Eq. (2.3.13) and Eq. (2.3.14), we have

$$\mathcal{D}_{ov}\gamma_5 + \gamma_5\mathcal{D}_{ov} = (\mathcal{D}_{ov} + \mathcal{D}_{ov}^\dagger)\gamma_5 = a(\mathcal{D}_{ov}\mathcal{D}_{ov}^\dagger)\gamma_5 = a\mathcal{D}_{ov}\gamma_5\mathcal{D}_{ov}, \tag{2.3.15}$$

which is Eq (2.3.10). The associated massive overlap Dirac operator is defined as

$$\begin{aligned} D_m &= \frac{1}{a}[\rho D_{ov}(\rho) + m\left(1 - \frac{aD_{ov}(\rho)}{2}\right)] \\ &= \frac{1}{a}[\rho + \frac{m}{2} + \left(\rho - \frac{ma}{2}\right)\gamma_5 \mathrm{sign}(\gamma_5 D_w(\rho))]. \end{aligned} \tag{2.3.16}$$

2.4 Numerical simulations

The discretized gluon and fermion measure is a product on each of the lattice points as

$$\mathcal{D}U \to \prod_{n,\mu} dU_\mu(n),\ \mathcal{D}[\psi,\bar{\psi}] \to \prod_n d\psi(n) \prod_m d\bar{\psi}(m). \tag{2.4.1}$$

With a rescaling of fermions and quark mass as

$$\psi \to \frac{1}{a^{3/2}}\psi,\ \bar{\psi} \to \frac{1}{a^{3/2}}\bar{\psi},\ m \to \frac{1}{a}m, \tag{2.4.2}$$

we can absorb all the lattice spacing a factors in the action. Along with the fermion and gluon actions on the lattice, we can re-write Eq. (2.1.1) as

$$\langle\mathcal{O}\rangle = \frac{\int \prod_n d\psi(n) \prod_m d\bar{\psi}(m) \prod_{k,\mu} dU_\mu(k) \mathcal{O}(\bar{\psi},\psi,U) e^{-S_G[U]-S_F[\bar{\psi},\psi,U]}}{\int \prod_n d\psi(n) \prod_m d\bar{\psi}(m) \prod_{k,\mu} dU_\mu(k) e^{-S_G[U]-S_F[\bar{\psi},\psi,U]}}. \tag{2.4.3}$$

By using Grassmann algebra of the fermion fields, we can integrate out the fermion degrees of freedom to have

$$\langle\mathcal{O}\rangle = \frac{\int \prod_{k,\mu} dU_\mu(k) (\prod_f \mathrm{Det}[\mathcal{D}_f]) \mathcal{O}(U) e^{-S_G[U]}}{\int \prod_{k,\mu} dU_\mu(k) (\prod_f \mathrm{Det}[\mathcal{D}_f]) e^{-S_G[U]}}, \tag{2.4.4}$$

in which f is the flavor of quarks we consider in our simulation such as up, down and strange quark, and $\mathrm{Det}[\mathcal{D}_f]$ is the determinant of the fermion action matrix. The γ_5-hermiticity of the Dirac operator $\mathcal{D}$ gives us

$$\mathrm{Det}[\mathcal{D}_f] = \mathrm{Det}[\gamma_5\mathcal{D}_f\gamma_5] = \mathrm{Det}[\mathcal{D}_f^\dagger] = \mathrm{Det}[\mathcal{D}_f]^*, \tag{2.4.5}$$

thus $\mathrm{Det}[\mathcal{D}_f]$ is real. For an even number of mass-degenerate quarks, the fermion determinant is raised to an even power and the combined weight factor is nonnegative. For a fermion which obeys the Ginsparg-Wilson equation, the eigenvalues of massless Dirac operator come in complex conjugate pairs [22]; thus the determinant is real and non-negative even with odd powers of the fermion determinant and the determinant is positive if one introduces a mass term as in Eq. 2.3.16. And we know $e^{-S_G[U]}$ is positive as $S_G[U]$ is shown to be real in Eq. 2.2.9. Thus we can evaluate Eq. (2.4.3)

by treating the positive value $\prod_f \mathrm{Det}[\mathcal{D}_f]e^{-S_G[U]}$ (which is only a function of gauge links) as a Boltzmann factor to have

$$\langle \mathcal{O} \rangle = \sum_{i \epsilon G} \frac{1}{N} \mathcal{O}(U_i), \tag{2.4.6}$$

in which G is an ensemble of gauge configurations generated with Monte Carlo methods with the distribution probability $\prod_f \mathrm{Det}[\mathcal{D}_f]e^{-S_G[U]}$, and N is the number of gauge configurations.

The remaining problem of calculating the operator $\mathcal{O}(U)$ in Eq. (2.4.4) from operator $\mathcal{O}(\bar{\psi}, \psi, U)$ in Eq. (2.4.3) requires an evaluation of quark propagator in each of the background gauge configurations as

$$\mathcal{D}^{-1}(y, x) = \langle \psi(y)\bar{\psi}(x) \rangle = \langle \mathcal{D}^{-1}(y, x; U) \rangle \,, \tag{2.4.7}$$

in which x and y are any space-time positions on the lattice. Such a propagator satisfies γ_5-hermiticity as

$$\mathcal{D}^{-1} = \langle \mathcal{D}^{-1} \rangle = \langle (\gamma_5 \mathcal{D}^\dagger \gamma_5)^{-1} \rangle = \gamma_5 \mathcal{D}^{\dagger -1} \gamma_5. \tag{2.4.8}$$

It is practically impossible to get this propagator for all combinations of x and y. Instead, we will calculate a propagator from a single point source at x_0 with $S(x) = \delta_{x,x_0}$ which satisfies

$$\sum_y \mathcal{D}(x, y)\mathcal{D}^{-1}(y, x_0) = S(x) = \delta_{x,x_0}. \tag{2.4.9}$$

This will need a linear matrix solver to numerically calculate the inverse of $\mathcal{D}$. For the general cases such as extended sources, we will need a propagator $\mathcal{D}^{-1}(y, S)$ from a source vector S which has different complex values at different lattice positions and satisfies

$$\sum_y \mathcal{D}(x, y)\mathcal{D}^{-1}(y, S) = S(x). \tag{2.4.10}$$

Defining the complex numbers at different lattice positions w as $f(w)$, with $S = f(w)$, then

$$\sum_y \mathcal{D}(x, y)(\sum_w f(w)\mathcal{D}^{-1}(y, w)) = \sum_w f(w)\delta_{x,w} = S(x). \tag{2.4.11}$$

Thus, the general propagator is a sum of point source propagators from single point w as

$$\mathcal{D}^{-1}(y, S) = \sum_w f(w)\mathcal{D}^{-1}(y, w). \tag{2.4.12}$$

It is worth noting that we only need one inversion of the Dirac operator to reach this general propagator.

To accommodate the chiral transformation in Eq. (2.3.10), it is usually convenient to use the chirally regulated field $\hat{\psi} = (1 - \frac{1}{2}\mathcal{D}_{ov})\psi$ in lieu of ψ in the interpolation field and the currents [24, 25, 26, 27, 28]. This turns out to be equivalent to leaving unchanged the unmodified interpolation field and currents and adopting instead the effective propagator which also serves to filter out the unphysical eigenmode at $\lambda = 2\rho$ which can be calculated as

$$\mathcal{D}_{eff}^{-1} \equiv \left(1 - \frac{\mathcal{D}_{ov}}{2}\right)\mathcal{D}_m^{-1} = \frac{1}{\mathcal{D}_c + m}, \tag{2.4.13}$$

where $\mathcal{D}_c = \frac{\rho\mathcal{D}_{ov}}{1-\mathcal{D}_{ov}/2}$ and is non-local. This effective propagator has the same form as that in the continuum. $\mathcal{D}_c$ can be proven to be chiral as

$$\mathcal{D}_c\gamma_5 + \gamma_5\mathcal{D}_c = 0. \tag{2.4.14}$$

In order to solve Eq. (2.4.12) for the effective massive propagator in Eq. (2.4.13), we generate the eigenvectors v_i for the massless overlap Dirac operator $\mathcal{D}_{ov}$ operator and the corresponding eigenvalues λ_i to some cutoff λ_n which starts from the lowest eigenvalue to the cutoff λ_n [29]. Notice that since D_{ov} satisfies Eq. (2.3.14), the eigenvectors will come in pairs as v_i and $\gamma_5 v_i$ with eigenvalues λ_i and λ_i^* respectively as

$$\mathcal{D}_{ov}v_i = \lambda_i v_i, \mathcal{D}_{ov}\gamma_5 v_i = \lambda_i^*\gamma_5 v_i. \tag{2.4.15}$$

By using this eigensystem, we first separate the source vector S into high-mode and low-mode parts defined as

$$S^L = \sum_i^n \left[v_i(v_i^\dagger S) + \gamma_5 v_i(\gamma_5 v_i^\dagger S)\right](1 - \frac{1}{2}\delta_{\lambda_i,0}),\ S^H = S - S^L, \tag{2.4.16}$$

where the factor $\delta_{\lambda_i,0}$ takes care of the zero modes are either left-handed or right-handed vector. We define the corresponding high-mode propagator P^H and low-mode propagator P^L as

$$D(m,\rho)P^H = S^H,\ D(m,\rho)P^L\ = S^L, \tag{2.4.17}$$

with the total propagator $P = P^H + P^L$. The low-mode propagator can be constructed using eigenvectors v_i as

$$\begin{aligned} P^L = \sum_i^n \left[\frac{1 - \frac{\lambda_i}{2}}{\rho\lambda_i + m(1 - \frac{\lambda_i}{2})}v_i(v_i^\dagger S^L) + \frac{1 - \frac{\lambda_i^*}{2}}{\rho\lambda_i^* + m(1 - \frac{\lambda_i^*}{2})}\gamma_5 v_i(\gamma_5 v_i^\dagger S^L)\right] \\ \times (1 - \frac{1}{2}\delta_{\lambda_i,0}). \end{aligned} \tag{2.4.18}$$

Then we can use conjugate gradient solver (CGNE) [30, 31] for $\mathcal{D}(m)\mathcal{D}(m)^\dagger$ as a multi-mass inverter to get the high-mode propagator P^H at different quark masses in one stroke with the multi-shift algorithm [32, 33].

Chapter 3 Correlation functions

3.1 Two-point correlation functions

Hadron spectroscopy is categorized by the combination of quantum numbers such as spin, parity, flavor content, etc. By using an operator with the same quantum numbers as the hadron studied, Lattice QCD is able to reproduce the hadron masses measured by experiment. In this section, we will focus on the two-point correlation functions of a meson (charged pion) and a baryon (nucleon). The first step of these calculations is the identification of hadron interpolators $\hat{\mathcal{O}}, \hat{\mathcal{O}}^\dagger$ which correspond to the annihilation and creation of the particle states.

Pion two-point functions

A hadron interpolator is constructed with gauge-invariant color singlets made from quarks and gluons, such as the local meson interpolators,

$$\mathcal{O}_M(x) \equiv \bar{\psi}^{f_1}(x)\Gamma\psi^{f_2}(x), \tag{3.1.1}$$

contracted from an anti-quark with flavor f_1 and a quark with flavor f_2, where $f_1 \neq f_2$, Γ matrix is a multiplication of Dirac gamma matrices which are chosen so that $\mathcal{O}_M(x)$ has the same symmetry as the desired particle state, and $x = na$ is the discrete position on the lattice. The corresponding interpolator $\bar{\mathcal{O}}_M$, which generates the meson state from the vacuum is the conjugate of the interpolator (3.1.1), satisfies

$$(\bar{\psi}^{f_1}\Gamma\psi^{f_2})^\dagger \;\; = -\psi^{f_2\dagger}\Gamma^\dagger\bar{\psi}^{f_1\dagger} = -\bar{\psi}^{f_2}\gamma_4\Gamma^\dagger\gamma_4\psi^{f_1} = \pm\bar{\psi}^{f_2}\Gamma\psi^{f_1}. \tag{3.1.2}$$

The first minus sign comes from the interchange of the fermion fields and the last step reflects the interchange of gamma matrices as $\gamma_4\Gamma^\dagger\gamma_4 = \pm\Gamma$. Thus up to a possible overall sign, $\bar{\mathcal{O}}_M$ is

$$\bar{\mathcal{O}}_M = \bar{\psi}^{f_2}\Gamma\psi^{f_1}. \tag{3.1.3}$$

Combining these two interpolators we can have two-point correlation functions

$$\langle\mathcal{O}_M(y)\bar{\mathcal{O}}_M(x)\rangle \tag{3.1.4}$$

to be calculated with propagators as (summation convention is used for all duplicated indices below),

$$\begin{aligned}
\langle\mathcal{O}_M(y)\bar{\mathcal{O}}_M(x)\rangle &= \langle\bar{\psi}^{f_1}(y)\Gamma\psi^{f_2}(y)\bar{\psi}^{f_2}(x)\Gamma\psi^{f_1}(x)\rangle \\
&= \langle\bar{\psi}^{f_1}(y)^{c_1}_{\alpha_1}\Gamma_{\alpha_1\beta_1}\psi^{f_2}(y)^{c_1}_{\beta_1}\bar{\psi}^{f_2}(x)^{c_2}_{\alpha_2}\Gamma_{\alpha_2\beta_2}\psi^{f_1}(x)^{c_2}_{\beta_2}\rangle \\
&= -\Gamma_{\alpha_1\beta_1}\Gamma_{\alpha_2\beta_2}\langle\psi^{f_2}(y)^{c_1}_{\beta_1}\bar{\psi}^{f_2}(x)^{c_2}_{\alpha_2}\psi^{f_1}(x)_{\beta_2,c_2}\bar{\psi}^{f_1}(y)_{\alpha_1,c_1}\rangle \\
&= -\Gamma_{\alpha_1\beta_1}\Gamma_{\alpha_2\beta_2}D^{-1}_{f_2}(y|x)^{c_1c_2}_{\beta_1\alpha_2}D^{-1}_{f_1}(x|y)^{c_2c_1}_{\beta_2\alpha_1} \\
&= -\mathrm{Tr}[\Gamma D^{-1}_{f_2}(y|x)\Gamma D^{-1}_{f_1}(x|y)],
\end{aligned} \tag{3.1.5}$$

in which we denote the color indices with $c_1, c_2 \in \{1,2,3\}$ as superscripts, the Dirac indices with $\alpha_1, \alpha_2, \beta_1, \beta_2 \in \{1,2,3,4\}$ as subscripts, the trace Tr is over color and spin, $D^{-1}_{f_2}(y|x)$ is the propagator from position x to y with quark flavor f_2 and $D^{-1}_{f_1}(x|y)$ is the propagator from position y to x with quark flavor f_1. For the case of the pion, ψ^{f_1} and ψ^{f_2} correspond to up quark u and down quark d. The u and d quarks differ only by the value of the mass parameter within QCD and the small mass difference between them is often ignored in current lattice QCD simulations with the u and d quark Dirac operators are equivalent, $D_u = D_d$, i.e., we have exact isospin symmetry. We can also utilize γ_5-hermiticity of the propagator to relate the two propagators in Eq. (3.1.5) as

$$\gamma_5 D^{-1}\gamma_5 = D^{-1\dagger} \rightarrow (\gamma_5)_{\alpha\alpha'} D^{-1}(x|y)^{cd}_{\alpha'\beta'} (\gamma_5)_{\beta'\beta} = D^{-1}(y|x)^{dc\,*}_{\beta\alpha}. \tag{3.1.6}$$

Thus for the case of charged pion with interpolator $\mathcal{O}_{\pi^+} = \bar{d}\gamma_5 u$ and $\mathcal{O}^\dagger_{\pi^+} = \bar{\mathcal{O}}_{\pi^+} = \bar{u}\gamma_5 d$ the correlation function $C_{\pi^+}(y,x)$ from position x to position y is

$$\begin{aligned} C_{\pi^+}(y,x) &\equiv \langle \mathcal{O}_{\pi^+}(y)\mathcal{O}^\dagger_{\pi^+}(x)\rangle = \mathrm{Tr}[\gamma_5 D^{-1}(y|x)\gamma_5 D^{-1}(x|y)] \\ &= \mathrm{Tr}[\gamma_5 D^{-1}(y|x)\gamma_5\gamma_5 D^{-1}(y|x)^*\gamma_5] = \sum_{\alpha\beta,cd} |D^{-1}(y|x)^{cd}_{\alpha\beta}|^2. \end{aligned} \tag{3.1.7}$$

The hadron states with definite momentum $\vec{p}$ can be obtained with a Fourier transformation on the correlation function at position $y = (\vec{y}, t)$ (assuming position $x = (\vec{0}, 0)$) as

$$C_{\pi^+}(\vec{p}, t, 0) = \sum_{\vec{y}\in\Lambda_3} e^{-i\vec{y}\cdot\vec{p}} \left\langle \mathcal{O}_{\pi^+}(\vec{y}, t)\mathcal{O}^\dagger_{\pi^+}(\vec{0}, 0)\right\rangle, \tag{3.1.8}$$

in which $\Lambda_3 = \{\vec{n} = (n_1, n_2, n_3) | n_i \in [0, L_i - 1]\}$ is the spatial volume, L_i is the spatial length in ith direction, and $p_i = \frac{2\pi n_i}{L_i a}$ is the lattice momenta. In order to interpret this correlation function, we introduce the normalization of states as

$$\begin{aligned} \langle n, \vec{p}\,|n', \vec{p}\,'\rangle &= (La)^3 \frac{2E^n_p}{2m}\delta_{n,n'}\delta_{\vec{p},\vec{p}'} \\ \mathcal{I} &= |0\rangle\langle 0| + \sum_n \sum_{\vec{p}} \frac{2m}{(La)^3 2E^n_p} |n, \vec{p}\rangle\langle n, \vec{p}| \end{aligned} \tag{3.1.9}$$

in which n and n' are the labels of a hadron ground state, such as pion or nucleon, and its excited states which vanishes at large t and T with T the total number of time slices of the lattice, $\langle n, \vec{p}|$ is the hadron with momentum $\vec{p}$, $|n', \vec{p}\,'\rangle$ is the hadron with $\vec{p}\,'$, E^n_p is the energy of the n^{th} hadron state at momentum $\vec{p}$, and m is the ground state energy at zero momentum which is the mass of the hadron. Also we can express $\mathcal{O}_{\pi^+}(x)$ with

$$\mathcal{O}_{\pi^+}(x) = e^{+i\hat{p}x}\mathcal{O}_{\pi^+}(0)e^{-i\hat{p}x} = e^{\hat{H}t}e^{-i\hat{\vec{p}}\cdot\vec{x}}\mathcal{O}_{\pi^+}(0)e^{-\hat{H}t}e^{i\hat{\vec{p}}\cdot\vec{x}}, \tag{3.1.10}$$

due to translational invariance, in which $\hat{H}$ is the Hamiltonian of the system and $\hat{\vec{p}}$ is the momentum operator. $\mathcal{O}_{\pi^+}(0)$ and $\mathcal{O}^\dagger_{\pi^+}(0)$ could annihilate and create a $\pi^+(\vec{p})$

state from the vacuum, respectively, as

$$\begin{aligned} \langle 0|\,\mathcal{O}_{\pi^+}(0)\,|\pi^+(\vec{p})\rangle = Z_p, \quad \langle \pi^+(\vec{p})|\,\mathcal{O}^\dagger_{\pi^+}(0)\,|0\rangle = Z_p^*, \\ \langle \pi^-(\vec{p})|\,\mathcal{O}_{\pi^+}(0)\,|0\rangle = Z_p^*, \quad \langle 0|\,\mathcal{O}^\dagger_{\pi^+}(0)\,|\pi^-(\vec{p})\rangle = Z_p, \end{aligned} \tag{3.1.11}$$

in which Z_p is the overlap matrix element at momentum $\vec{p}$. The second matrix element comes from $\mathcal{O}^\dagger_{\pi^+}(0) = \mathcal{O}_{\pi^-}(0)$ under isospin symmetry. Insert the complete set of normalized energy eigenstates of Eq. (3.1.9) into Eq. (3.1.8) and use Eq. (3.1.10) and Eq. (3.1.11) to get

$$\begin{aligned} C_{\pi^+}(\vec{p},t,0) &= \sum_x e^{-i\vec{p}\cdot\vec{x}}\,\langle \mathcal{O}_{\pi^+}(x,t)\mathcal{O}^\dagger_{\pi^+}(0,0)\rangle \\ &= \sum_x e^{-i\vec{p}\cdot\vec{x}} \sum_{n',\vec{p_2}} \frac{2m}{(La)^3 2E^{n'}_{p_2}} \sum_{n,\vec{p_1}} \frac{2m}{(La)^3 2E^{n}_{p_1}} \\ &\quad \langle n',p_2|\,e^{-\hat{H}T}\mathcal{O}_{\pi^+}(x,t)\,|n,p_1\rangle\langle n,p_1|\,\mathcal{O}^\dagger_{\pi^+}(0,0)\,|n',p_2\rangle\,, \end{aligned} \tag{3.1.12}$$

under periodic boundary conditions. Let us first look at the last line of the equation,

$$\begin{aligned} &\langle n',p_2|e^{-\hat{H}T}\mathcal{O}_{\pi^+}(x,t)\,|n,p_1\rangle\,\langle n,p_1|\,\mathcal{O}^\dagger_{\pi^+}(0,0)\,|n',p_2\rangle \\ &\quad = \langle n',p_2|\,e^{-\hat{H}(T-t)}e^{-i\hat{\vec{q}}\cdot\vec{x}}\mathcal{O}_{\pi^+}(0)e^{-\hat{H}t}e^{i\hat{\vec{q}}\cdot\vec{x}}\,|n,p_1\rangle\,\langle n,p_1|\,\mathcal{O}^\dagger_{\pi^+}(0)\,|n',p_2\rangle \\ &\quad \xrightarrow{t\gg 1} e^{-E^{n'}_{p_2}(T-t)}e^{-i\vec{p}_2\cdot\vec{x}}\,\langle n',p_2|\,\mathcal{O}_{\pi^+}(0)\,|0\rangle\,\langle 0|\,\mathcal{O}^\dagger_{\pi^+}(0)\,|n',p_2\rangle \\ &\qquad + e^{-E^{n}_{p_1}t}e^{i\vec{p}_1\cdot\vec{x}}\,\langle 0|\,\mathcal{O}_{\pi^+}(0)\,|n,p_1\rangle\,\langle n,p_1|\,\mathcal{O}^\dagger_{\pi^+}(0)\,|0\rangle \\ &\quad = |Z_{p_2}|^2 e^{-i\vec{p}_2\cdot\vec{x}}e^{-E^{n'}_{p_2}(T-t)} + |Z_{p_1}|^2 e^{i\vec{p}_1\cdot\vec{x}}e^{-E^{n}_{p_1}t}. \end{aligned} \tag{3.1.13}$$

Thus we have

$$\begin{aligned} C_{\pi^+}(\vec{p},t,0) &\xrightarrow{t\gg 1} \sum_x e^{-i\vec{p}\cdot\vec{x}} \sum_{n',\vec{p_2}} \frac{2m}{(La)^3 2E^{n'}_{p_2}} \frac{1}{(La)^3} |Z_{p_2}|^2 e^{-i\vec{p}_2\cdot\vec{x}} e^{-E^{n'}_{p_2}(T-t)} \\ &\quad + \sum_x e^{-i\vec{p}\cdot\vec{x}} \sum_{n,\vec{p_1}} \frac{2m}{(La)^3 2E^{n}_{p_1}} \frac{1}{(La)^3} |Z_{p_1}|^2 e^{i\vec{p}_1\cdot\vec{x}} e^{-E^{n}_{p_1}t} \\ &= \sum_{n',\vec{p_2}} \frac{2m}{(La)^3 2E^{n'}_{p_2}} \delta_{\vec{p},-\vec{p}_2} |Z_{p_2}|^2 e^{-E^{n'}_{p_2}(T-t)} \\ &\quad + \sum_{n,\vec{p_1}} \frac{2m}{(La)^3 2E^{n}_{p_1}} \delta_{\vec{p},\vec{p}_1} |Z_{p_1}|^2 e^{-E^{n}_{p_1}t}. \end{aligned} \tag{3.1.14}$$

Combining the results, we have

$$C_{\pi^+}(\vec{p},t,0) \xrightarrow{t\gg 1} \frac{|Z_p|^2(2m)}{(La)^3 2E_p}(e^{-E_p t} + e^{-E_p(T-t)})(1+\mathcal{O}(e^{-t\Delta_E})), \tag{3.1.15}$$

in which $\mathcal{O}(e^{-t\Delta_E})$ represent the contributions from excited states and $|Z_p|^2$ is the spectral weight. From the free fermion lattice propagator in momentum space, one

can identify the pole at momentum $\vec{p}$ and find the lattice dispersion relation ($c = 1$ in our units) [34],

$$\cosh(aE_p) = \cosh(am) + \sum_{k=1}^{3}(1 - \cos(ap_k)), \tag{3.1.16}$$

which at vanishing a approaches the continuum relation $E_p = \sqrt{m^2 + \vec{p}^2}$.

Proton two-point functions

A typical nucleon (i.e., proton or neutron) interpolator with a given spinor index α constructed from three quarks is [35]

$$\mathcal{O}_N(x)_\alpha \equiv \epsilon_{abc} u(x)^a_\alpha (u(x)^b_\beta \widetilde{\mathcal{C}}_{\beta\gamma} d(x)^c_\gamma), \tag{3.1.17}$$

in which $\mathcal{C} \equiv \gamma_2\gamma_4$ is the charge conjugation operator with $\widetilde{\mathcal{C}} = \mathcal{C}\gamma_5$ and ϵ_{abc} is the three dimension Levi-Civita symbol with $\epsilon_{abc} = 1$ if (a, b, c) is an even permutation of $(1, 2, 3)$, -1 if it is an odd permuation, and 0 if any index is repeated. The corresponding creation operator is

$$\bar{\mathcal{O}}_N(x)_\alpha \equiv -\epsilon_{abc}(\bar{u}(x)^c_\gamma \widetilde{\mathcal{C}}_{\gamma\beta} \bar{d}(x)^b_\beta)\bar{u}(x)^a_\gamma. \tag{3.1.18}$$

With these two interpolators, the nucleon correlation function contraction is

$$\begin{aligned}
\langle \mathcal{O}_N(y)_\gamma \bar{\mathcal{O}}_N(x)_{\gamma'} \rangle &= \langle \epsilon_{abc}\epsilon_{a'b'c'} \left(u(x)_{\gamma,c} (u(x)^T_a \widetilde{\mathcal{C}} d(x)_b) \right) \left((\bar{u}(x)^T_{a'} \widetilde{\mathcal{C}} \bar{d}(x)^T_{b'}) u(x)_{\gamma',c'} \right) \rangle \\
&= \epsilon_{abc}\epsilon_{a'b'c'} \widetilde{\mathcal{C}}_{\alpha'\beta'} \widetilde{\mathcal{C}}_{\alpha\beta} D_d^{-1}(y|x)^{b'b}_{\beta'\beta} \times \\
&\quad \left(D_u^{-1}(y|x)^{a'a}_{\alpha'\alpha} D_u^{-1}(y|x)^{c'c}_{\gamma'\gamma} - D_u^{-1}(y|x)^{a'c}_{\alpha'\gamma} D_u^{-1}(y|x)^{c'a}_{\gamma'\alpha} \right), \\
&= \epsilon_{abc}\epsilon_{a'b'c'} \mathrm{Tr} \left[\widetilde{\mathcal{C}} D_d^{-1}(y|x)^{b'b} (D_u^{-1}(y|x)^{a'a} \widetilde{\mathcal{C}})^T \right] D_u^{-1}(y|x)^{c'c}_{\gamma'\gamma} \\
&\quad - \epsilon_{abc}\epsilon_{a'b'c'} \left[(D_u^{-1}(y|x)^{a'c})^T \widetilde{\mathcal{C}} D_d^{-1}(y|x)^{b'b} (D_u^{-1}(y|x)^{c'a} \widetilde{\mathcal{C}})^T \right]_{\gamma\gamma'} \\
&= \epsilon_{abc}\epsilon_{a'b'c'} \mathrm{Tr} \left[\underline{D_d^{-1}(y|x)^{b'b}} D_u^{-1}(y|x)^{a'a} \right] D_u^{-1}(y|x)^{c'c}_{\gamma'\gamma} \\
&\quad + \epsilon_{abc}\epsilon_{a'b'c'} \left[D_u^{-1}(y|x)^{c'c} \underline{D_d^{-1}(y|x)^{b'b}} D_u^{-1}(y|x)^{a'a} \right]_{\gamma'\gamma}
\end{aligned} \tag{3.1.19}$$

in which $(\cdots)^T$ is transpose over Dirac index, $\mathrm{Tr}[\cdots]$ is over Dirac index only, the free index γ or γ' corresponds to the free Dirac index of initial or final nucleon, respectively, and define the Dirac space the quantity $\underline{Q} \equiv (\widetilde{\mathcal{C}} Q \widetilde{\mathcal{C}}^{-1})^T$ for an arbitrary matrix Q. We have used the commutation relations of γ matricies $\{\gamma_\mu, \gamma_\nu\} = 2\delta_{\mu\nu}$ and exchange of color index $a \longleftrightarrow c$ for the last step. With a Fourier transform at position y and fixed $x = 0$, the nucleon correlation function with momentum $\vec{p}$ is

$$G_{NN,\gamma,\gamma'}(\vec{p}, t) = \sum_y e^{-\vec{p}\cdot\vec{x}} \langle \mathcal{O}_N(y)_\gamma \bar{\mathcal{O}}_N(0)_{\gamma'} \rangle . \tag{3.1.20}$$

In order to expand this equation with the energy states of the nucleon, we first consider the equation of motion of the nucleon, which is a spin-$\frac{1}{2}$ particle, as

$$\begin{cases} (\not{p} - im)u(p,s) = 0 \\ \bar{u}(p,s)(\not{p} - im) = 0 \end{cases} \tag{3.1.21}$$

The solution of equation under current γ matrix convention in Eq. (2.1.10) is,

$$\begin{aligned} u(p,s) &= \sqrt{\frac{E_p + m}{m}} \begin{pmatrix} I \\ \frac{\vec{\sigma}\cdot\vec{p}}{E_p+m} \end{pmatrix} \chi_s \\ \bar{u}(p,s) &= \sqrt{\frac{E_p + m}{m}} \chi_s^\dagger \begin{pmatrix} I \\ (-1)\frac{\vec{\sigma}\cdot\vec{p}}{E_p+m} \end{pmatrix}, \end{aligned} \tag{3.1.22}$$

in which $\chi_1 \equiv \chi_2' \equiv \begin{pmatrix} 1 \\ 0 \end{pmatrix}$ and $\chi_2 \equiv \chi_1' \equiv \begin{pmatrix} 0 \\ 1 \end{pmatrix}$, and $\vec{\sigma}$ is the Pauli matrices

$$\sigma_1 = \begin{pmatrix} 0 & 1 \\ 1 & 0 \end{pmatrix}, \ \sigma_2 = \begin{pmatrix} 0 & \text{-i} \\ \text{i} & 0 \end{pmatrix}, \ \sigma_3 = \begin{pmatrix} 1 & 0 \\ 0 & \text{-1} \end{pmatrix}. \tag{3.1.23}$$

The spinors u and $\bar{u}$ satisfy the normalization conditions $\bar{u}(p,s)u(p,s') = \delta_{s,s'}$ and $\sum_s u(p,s)\bar{u}(p,s) = \frac{-i\not{p}+m}{2m}$. Then we have

$$\begin{aligned} \langle 0| \mathcal{O}_N(x) |N_P(\vec{p},s,+)\rangle &= \lambda_+ u(\vec{p},s,+)e^{-ipx} \\ \langle N_P(\vec{p},s,+)| \bar{\mathcal{O}}_N(x) |0\rangle &= \lambda_+^* \bar{u}(\vec{p},s,+)e^{+ipx} \end{aligned} \tag{3.1.24}$$

in which + denotes positive parity state (i.e., the proton), and λ is the coupling strength. In the same way, we can write down the coupling to the negative parity state (i.e., S_{11}) as

$$\begin{aligned} \langle 0| \mathcal{O}_N(x) |N_P(\vec{p},s,-)\rangle &= \lambda_-(\gamma_5) u(\vec{p},s,-)e^{-ipx} \\ \langle N_P(\vec{p},s,-)| \bar{\mathcal{O}}_N(x) |0\rangle &= \lambda_-^* \bar{u}(\vec{p},s,+)(-\gamma_5)e^{+ipx}. \end{aligned} \tag{3.1.25}$$

With an insertion of complete set of states into Eq. (3.1.20), we have

$$G_{NN,\gamma,\gamma'}(\vec{p},t) = \sum_{n,s} \frac{m_n}{(La)^3 E_p^n} e^{-E_p^n t} \langle 0| \mathcal{O}_N(0)_\gamma |n\vec{p}s\rangle\langle n\vec{p}s| \bar{\mathcal{O}}_N(0)_{\gamma'} |0\rangle . \tag{3.1.26}$$

Using Eq. (3.1.24) and Eq. (3.1.25), we can split the sum into even parity part and odd parity part of states $|(n,+),s\rangle$ and $\langle(n,-),s|$, respectively. Let us consider the even parity part first as

$$\begin{aligned} &\sum_{(n,+),s} e^{-E_p^{n,+}t} \frac{m_{n,+}}{(La)^3 E_p^{n,+}} \langle 0| \mathcal{O}_N(0)_\gamma |(n,+)\vec{p}s\rangle\langle(n,+)\vec{p}s| \bar{\mathcal{O}}_N(0)_{\gamma'} |0\rangle \\ &= \frac{m_{n,+}}{(La)^3 E_p^{n,+}} \left[\sum_{n,s} e^{-E_p^{n,+}t} \lambda_+ u(\vec{p},s,+)\lambda_+^* \bar{u}(\vec{p},s,+) \right]_{\gamma\gamma'} \\ &= \frac{m_{n,+}}{(La)^3 E_p^{n,+}} \left[\lambda_+\lambda_+^* e^{-E_p^{n,+}t} \frac{-i\not{p} + m_{n,+}}{2m_{n,+}} \right]_{\gamma\gamma'}. \end{aligned} \tag{3.1.27}$$

Repeating the same steps for the odd parity part, we have

$$\begin{aligned} G_{NN}(\vec{p},t) = &\sum_{n_+} |\lambda_{n,+}|^2 e^{-E_p^{n,+}t} \frac{m_{n,+}}{(La)^3 E_{n,+}} \frac{-i\not{p} + m_{n,+}}{2m_{n,+}} \\ &- \sum_{n_-} |\lambda_{n,-}|^2 e^{-E_p^{n,-}t} \frac{m_{n,-}}{(La)^3 E_{n,-}} \frac{i\not{p} + m_{n,-}}{2m_{n,-}}, \end{aligned} \tag{3.1.28}$$

in which $E_{n,+}$ and $E_{n,-}$ correspond to the energy of even parity states and odd parity states at momentum $\vec{p}$ respectively. In order to project to definite parity, we use parity projection operator $\Gamma_\pm$ which is defined as

$$\Gamma_\pm = \frac{1}{2}\left(1 \pm \frac{m_\mp}{E_p^\mp}\gamma_4\right). \tag{3.1.29}$$

Consider the Γ_+ projection and only the ground state contribution to Eq. (3.1.28) as

$$\begin{aligned} \mathrm{Tr}[\Gamma_+ G_{NN}(\vec{p},t)] = &|\lambda_+|^2 e^{-E_p^+ t} \frac{m_+}{(La)^3 E_+} \frac{\mathrm{Tr}\left[\frac{1}{2}\left(1 + \frac{m_-}{E_p^-}\gamma_4\right)(-i\not{p} + m_+)\right]}{2m_+} \\ &- |\lambda_-|^2 e^{-E_p^- t} \frac{m_-}{(La)^3 E_p^-} \frac{\mathrm{Tr}\left[\frac{1}{2}\left(1 + \frac{m_-}{E_p^-}\gamma_4\right)(i\not{p} + m_-)\right]}{2m_-}, \end{aligned} \tag{3.1.30}$$

in which we have ignored label the $n = 0$ for the mass $m_{0,\pm}$ and energy $E_p^{0,\pm}$. By taking the trace of γ matrices, we have

$$\begin{aligned} \mathrm{Tr}[\Gamma_+ G_{NN}(\vec{p},t)] =&4|\lambda_+|^2 e^{-E_p^+ t} \frac{\frac{1}{2}(m_+ + \frac{m_-}{E_p^-}E_p^+)}{2(La)^3 E_p^+} - 4|\lambda_-|^2 e^{-E_p^- t} \frac{\frac{1}{2}(m_- - \frac{m_-}{E_p^-}E_p^-)}{2(La)^3 E_p^-} \\ =&(+)\frac{|\lambda_+|^2}{(La)^3}\left(\frac{m_+}{E_p^+} + \frac{m_-}{E_p^-}\right)e^{-E_p^+ t}. \end{aligned} \tag{3.1.31}$$

With the same steps, we have the Γ_- projection as

$$\begin{aligned} \mathrm{Tr}[\Gamma_+ G_{NN}(\vec{p},t)] =&4|\lambda_+|^2 e^{-E_p^+ t} \frac{\frac{1}{2}(m_+ - \frac{m_+}{E_p^+}E_p^+)}{2(La)^3 E_p^+} - 4|\lambda_-|^2 e^{-E_p^- t} \frac{\frac{1}{2}(m_- + \frac{m_+}{E_p^+}E_p^-)}{2(La)^3 E_p^-} \\ =&(-)\frac{|\lambda_-|^2}{(La)^3}\left(\frac{m_-}{E_p^-} + \frac{m_+}{E_p^+}\right)e^{-E_p^- t}. \end{aligned} \tag{3.1.32}$$

It can be seen from positive parity projection Eq. (3.1.31) and negative parity projection Eq. (3.1.32) that $\Gamma_\pm$ will completely project out the positive parity states and negative parity states, respectively. Whereas, $\Gamma_\pm$ depend on the mass $m_\pm$ and energy $E_\pm$ which is unknown for specific lattice simulation except for the zero momentum case. Thus, in practice we will always use $P_\pm$ which is defined as

$$P_\pm \equiv \frac{1}{2}(1 \pm \gamma_4), \tag{3.1.33}$$

and satisfies $P_\pm^2 = P_\pm$. With P_+ we have

$$\begin{aligned}\mathrm{Tr}[P_+ G_{NN}(\vec{p},t)] = &\sum_{n_+} \frac{\lambda_{n,+}\lambda^*_{n,+}}{(La)^3} e^{-E_{n,+}t} \frac{m_{n,+}}{E_{n,+}} \frac{E_{n,+}+m_{n,+}}{m_{n,+}} \\ &+ \sum_{n_-} \frac{\lambda_{n,-}\lambda^*_{n,-}}{(La)^3} e^{-E_{n,-}t} \frac{m_{n,-}}{E_{n,-}} \frac{E_{n,-}-m_{n,-}}{m_{n,-}}.\end{aligned} \tag{3.1.34}$$

Thus at zero momentum, only even parity contributes at large t. Nucleon with non-zero momentum will still have some contaminations from the negative parity states. This contamination is exponentially suppressed in the long time range as the negative parity state has higher mass and energy than the positive parity counterpart. Thus, if we ignore the negative parity part, we will have the main contribution as

$$\mathrm{Tr}[P_+ G_{NN}(\vec{p},t)] \xrightarrow{t\gg 1} \frac{E_p^{0,+}+m_{0,+}}{m_{0,+}} \frac{|\lambda_{0,+}|^2}{(La)^3} e^{-m_{0,+}t} \times (1+\mathcal{O}(e^{-t\Delta_E})). \tag{3.1.35}$$

From this correlation function, we can define the nucleon effective mass as

$$E_{eff} = \ln \frac{\mathrm{Tr}[P_+ G_{NN}(\vec{p},t)]}{\mathrm{Tr}[P_+ G_{NN}(\vec{p},t+1)]}. \xrightarrow{t\gg 1} E_p^{0,+} \tag{3.1.36}$$

3.2 Extended sources

In order to have better signals for correlation functions, we need to optimize the interpolation fields. Although any operator with the correct quantum numbers will project onto the physical state, the overlap can be improved significantly by considering the more realistic spatial wave functions. One way of doing so is using extended sources or so-called smeared fermions such as

$$\begin{aligned}\psi_1(\vec{x},t)^a_\alpha &\equiv \sum_{\vec{y}} S_1(\vec{x},\vec{y})^{a,b}_{\alpha,\beta} \psi(\vec{y},t)^b_\beta \\ \bar{\psi}_2(\vec{x},t)^a_\alpha &\equiv \sum_{\vec{y}} S_2(\vec{x},\vec{y})^{a,b}_{\alpha,\beta} \bar{\psi}(\vec{y},t)^b_\beta,\end{aligned} \tag{3.2.1}$$

in which S_1 and S_2 are the smearing functions which can be different. They satisfy the relationships $S_1^\dagger S_1 = \mathcal{I}$ and $S_2^\dagger S_2 = \mathcal{I}$ to keep gauge invariance. The propagator with these two smearing functions is

$$\begin{aligned}\mathcal{D}_S^{-1}(y,x)^{ba}_{\beta\alpha} &\equiv \langle \psi_1(y)^b_\beta \bar{\psi}_2(x)^a_\alpha \rangle \\ &= \langle (\sum_{\vec{z}_1} S_1(\vec{y},z_1)^{b,c_1}_{\beta,\gamma_1} \psi(\vec{z}_1,y_t)^{c_1}_{\gamma_1}) (\sum_{\vec{z}_2} S_2(\vec{x},\vec{z}_2)^{a,c_2}_{\alpha,\gamma_2} \bar{\psi}(\vec{z}_2,x_t)^{c_2}_{\gamma_2}) \rangle \\ &= \sum_{\vec{z}_1,\vec{z}_2} \mathcal{D}^{-1}(\{\vec{z}_1,y_t\},\{\vec{z}_2,x_t\})^{c_1,c_2}_{\gamma_1\gamma_2} S_2(\vec{x},\vec{z}_2)^{a,c_2}_{\alpha,\gamma_2} S_1(\vec{y},z_1)^{b,c_1}_{\beta,\gamma_1}\end{aligned} \tag{3.2.2}$$

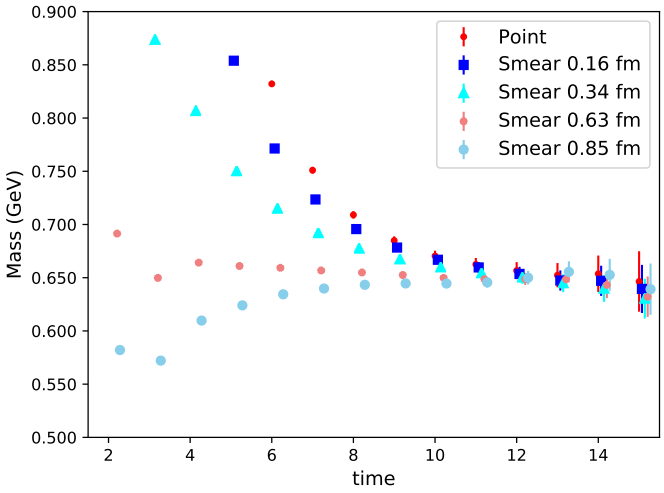

Figure 3.1: Example plot of the nucleon effective masses at zero momentum with several smearing sizes as a function of time. The "Smear" label in the plot gives the smearing size $\langle r^2 \rangle^{1/2}$. These calculations used overlap fermions on a $2+1$ flavor RBC/UKQCD domain wall $24^3 \times 64$ ensemble with $a = 0.111$ fm and $m_\pi = 339$ MeV.

in which $x = \{\vec{x}, x_t\}$ and $y = \{\vec{y}, y_t\}$. From the computational side, we will construct the propagator from a smeared source S_2 to a point-like sink propagator first as

$$\mathcal{D}_{S_2}^{-1}(\{\vec{z}_1, y_t\}, \{\vec{x}, x_t\}) \equiv \sum_{\vec{z}_2} \mathcal{D}^{-1}(\{\vec{z}_1, y_t\}, \{\vec{z}_2, x_t\})_{\gamma_1\gamma_2}^{c_1,c_2} S_2(\vec{x}, \vec{z}_2)_{\alpha,\gamma_2}^{a,c_2} \tag{3.2.3}$$

Then we can apply the sum at the sink point using smearing function S_1 as

$$\mathcal{D}_S^{-1}(y, x)_{\beta\alpha}^{ba} = \sum_{\vec{z}_1} S_1(\vec{y}, \vec{z}_1)_{\beta,\gamma_1}^{b,c_1} \mathcal{D}_{S_2}^{-1}(\{\vec{z}_1, y_t\}, \{\vec{x}, x_t\})_{\gamma_1\gamma_2}^{c_1,c_2} \tag{3.2.4}$$

A gauge covariant source with a shape similar to a Gaussian is obtained by Jacobi smearing [36, 37] as

$$S(x', x) = \left(1 - \frac{3w}{2n}\right)^n \left[1 + \frac{w^2}{4n - 6w^2} \sum_{i=1}^{3} \left(U_i(x', t)\delta_{x', x-\hat{i}} + U_i^\dagger(x' - \hat{i}, t)\delta_{x', x+\hat{i}}\right)\right]^n \tag{3.2.5}$$

in which w is the input width parameter for a Gaussian distribution and n is the number of smearing steps. The actual smearing size is related to w and n as discribed in [38]. Such smearing is known to have better overlap with the ground state in both pion and nucleon two-point correlation functions. Figure 3.1 shows the result of the nucleon effective mass defined in Eq. (3.1.36) with various smearing sizes. It can be seen that a relatively large smearing size such as $w = 8.0, n = 100$ with $\langle r^2 \rangle^{1/2} = 0.63$ fm will give better plateau at very early time slices compared to all other cases.

3.3 Grid source and momenta

In order to have good signals for baryon correlation functions, we have developed the grid source with Z_3 noises along with the low-mode substitution (LMS) method to construct the correlation functions [39, 29, 40, 1]. Z_3 noise grid is used so that the three quarks of the baryon from the same spatial location of the grid points will automatically contribute to the correlation function, whereas contributions from three quarks at different spatial locations will cancel by Z_3 noise. Low mode means the low lying overlap eigenvectors up to highest eigenvalue λ_c of the overlap Dirac operator D_{ov} which is defined in Sec. 2.4. For two-point functions and three-point functions with finite source momenta, we have developed the use of mixed momenta [40, 1] to accommodate Z_3 noise grid source and momenta. This section proposes a new way to use the mixed momenta to have better signals for the correlation functions with momenta.

Mixed momenta

As discussed in Sec. 2.4, we separate the propagator P into its high-mode and low-mode parts P^L and P^H based on the overlap eigensystem as in Eq. (2.4.17). In order to discuss correlation functions in momentum space, we define the point source propagator from position $(\vec{w}, 0)$ to sink position x as $P_{\vec{w}}(x)$ with $x = (\vec{x}, t)$ (we fix the initial time slice to be 0 in the following discussion) and the nucleon correlation function $G(x, \vec{0})$ constructed with this propagator is

$$G(x,\vec{0}) \equiv \langle \mathrm{Tr}[\Gamma_e \mathcal{O}_N(x)\bar{\mathcal{O}}_N(0)]\rangle = \langle C(P_{\vec{0}}(x), P_{\vec{0}}(x), P_{\vec{0}}(x))\rangle\,, \tag{3.3.1}$$

in which $\Gamma_e \equiv P_+ = \frac{1+\gamma_4}{2}$ is the non-polarized projector of the nucleon, $\langle\cdots\rangle$ denotes the gauge averaging, and $C(P_{\vec{0}}(x), P_{\vec{0}}(x), P_{\vec{0}}(x))$ is the nucleon contraction in Eq. (3.1.19) with polarization projection Γ_e as

$$\begin{aligned} C(P_{\vec{0}}(x), P_{\vec{0}}(x), P_{\vec{0}}(x)) &\equiv \mathrm{Tr}\left[\Gamma_e \langle \mathcal{O}_N(x)_\gamma \bar{\mathcal{O}}_N(0)_{\gamma'}\rangle\right] \\ &= \epsilon_{abc}\epsilon_{a'b'c'}\mathrm{Tr}\left[\widetilde{\mathcal{C}} D_d^{-1}(x|0)^{b'b}(D_u^{-1}(x|0)^{a'a}\widetilde{\mathcal{C}})^T\right]\mathrm{Tr}\left[\Gamma_e D_u^{-1}(x|0)^{c'c}\right] \\ &\quad - \epsilon_{abc}\epsilon_{a'b'c'}\mathrm{Tr}\left[\Gamma_e (D_u^{-1}(x|0)^{a'c})^T \widetilde{\mathcal{C}} D_d^{-1}(x|0)^{b'b}(D_u^{-1}(x|0)^{c'a}\widetilde{\mathcal{C}})^T\right]. \end{aligned} \tag{3.3.2}$$

The correlation function $G(x, \vec{0})$ in momentum space is

$$G(p,\vec{0}) \equiv \sum_{\vec{x}} e^{-i\vec{p}\cdot\vec{x}} C_{\mathrm{2pt}}(x,\vec{0}) \;\; = \langle \sum_x e^{-i\vec{p}\cdot\vec{x}} C(P_{\vec{0}}(x), P_{\vec{0}}(x), P_{\vec{0}}(x))\rangle\,. \tag{3.3.3}$$

The correlation functions $G(p, \vec{w})$ with propagators $P(x, \vec{w})$ starting from position $\vec{w}$ is

$$\begin{aligned} G(p,\vec{w}) &= \langle \sum_{\vec{x}} e^{-i\vec{p}\cdot\vec{x}} C(P_{\vec{w}}(x), P_{\vec{w}}(x), P_{\vec{w}}(x))\rangle \\ &= \langle \sum_{\vec{x}} e^{-i\vec{p}\cdot(\vec{x}+\vec{w})} C(P_{\vec{w}}(\vec{x}+\vec{w}, t), P_{\vec{w}}(\vec{x}+\vec{w}, t), P_{\vec{w}}(\vec{x}+\vec{w}, t))\rangle\,, \end{aligned} \tag{3.3.4}$$

in which we made a shift of summation variable $\vec{x} \to \vec{x} + \vec{w}$ in the second line. With the translation invariance of the correlation function,

$$\begin{aligned} &\langle C(P_{\vec{w}}(\vec{x}+\vec{w},t), P_{\vec{w}}(\vec{x}+\vec{w},t), P_{\vec{w}}(\vec{x}+\vec{w},t))\rangle \\ &\quad = \langle C(P_{\vec{0}}(\vec{x},t), P_{\vec{0}}(\vec{x},t), P_{\vec{0}}(\vec{x},t))\rangle \,, \end{aligned} \tag{3.3.5}$$

we have

$$\begin{aligned} G(p,\vec{w}) &= e^{-i\vec{p}\cdot\vec{w}} \sum_x e^{-i\vec{p}\cdot\vec{x}} \langle C(P_{\vec{0}}(x), P_{\vec{0}}(x), P_{\vec{0}}(x))\rangle \,, \\ &= e^{-i\vec{p}\cdot\vec{w}} \sum_{\vec{x}} e^{-i\vec{p}\cdot\vec{x}} G(x,\vec{0}) \\ &= e^{-i\vec{p}\cdot\vec{w}} G(p,\vec{0}), \end{aligned} \tag{3.3.6}$$

which differs from $G(p,\vec{0})$ by a phase factor $e^{-i\vec{p}\cdot\vec{w}}$.

Before the discussion of LMS, we define the random Z_3 grid source used in LMS as

$$S_{grid} \equiv \sum_i^n \eta_i S(\vec{w}_i),\ \ \vec{w}_i \in (x_0 + m_x\Delta_x, y_0 + m_y\Delta_y, z_0 + m_z\Delta_z) \tag{3.3.7}$$

where η_i is a Z_3 noise on each of the grid points $\vec{w}_0 = (x_0, y_0, z_0)$ is the starting point of the grid, $\Delta_{x,y,z} = L/2$ or $L/3$ or $L/4\cdots$ is the offset in the spatial direction respectively, $m_{x,y,z} \in (0, 1, \cdots, L_s/\Delta_{x,y,z})$ is the number of offset in each direction for each grid points, and $n = \frac{L_s^3}{\Delta_x\Delta_y\Delta_z}$ is the number of grid points of the grid source. As the Dirac operator is a linear operator, the random Z_3 grid source propagator can be written as

$$P_{S_{grid}}(x) = \sum_i^n \eta_i P^L_{\vec{w}_i}(x) + P^H_{S_{grid}}(x), \tag{3.3.8}$$

in which $P^L_{\vec{w}_i}(x)$ is the low-mode part of the point source propagator $P_{\vec{w}_i}(x)$ starting from position $\vec{w}_i$ which can be computed with the eigenvectors at each grid point, and $P^H(x, S_{grid})$ is computed within one inversion with grid source S_{grid} using Eq. (2.4.17) and

$$P^H_{S_{grid}}(x) = \sum_i \eta_i P^H_{\vec{w}_i}(x,\vec{w}_i), \tag{3.3.9}$$

with $P^H_{\vec{w}_i}(x)$ the high-mode part of the point source propagator $P_{\vec{w}_i}(x)$ which we defined for the purpose of this derivation. With these propagators, the nucleon correlation function with LMS is

$$\begin{aligned} G_{LMS}(p, S_{grid}) =& \Big\langle \Big\langle \sum_x e^{-i\vec{x}\cdot\vec{p}} \left(\sum_i^n \Big[C(\eta_i P^L_{\vec{w}_i} + P^H_{S_{grid}}, \eta_i P^L_{\vec{w}_i} + P^H_{S_{grid}}, \eta_i P^L_{\vec{w}_i} + P^H_{S_{grid}}) \Big] \right. \\ & \left. -(n-1) C(P^H_{S_{grid}}, P^H_{S_{grid}}, P^H_{S_{grid}}) \right) \Big\rangle_{Z_3} \Big\rangle. \end{aligned} \tag{3.3.10}$$

in which $\langle\cdots\rangle_{Z_3}$ denotes the noise averaging. We would like to see how this can be written as a sum of $G(p)$ to understand the result. Expanding the terms on the right side using Eq. (3.3.9), the term with all high-mode propagators is

$$\Big\langle\Big\langle C(P^H_{S_{grid}},P^H_{S_{grid}},P^H_{S_{grid}})\Big\rangle_{Z_3}\Big\rangle=\Big\langle\Big\langle\sum_{i,j,k}\eta_i\eta_j\eta_k C(P^H_{\vec{w}_i},P^H_{\vec{w}_j},P^H_{\vec{w}_k})\Big\rangle_{Z_3}\Big\rangle. \tag{3.3.11}$$

As η_i is Z_3 noise, we have $\langle\eta_i\eta_j\eta_k\rangle_{Z_3}=\delta_{i,j}\delta_{j,k}$ and $\eta_i\eta_i\eta_i=1$ which leads to (for each gauge configuration, we use different Z_3 noises)

$$\Big\langle\Big\langle C(P^H_{S_{grid}},P^H_{S_{grid}},P^H_{S_{grid}})\Big\rangle_{Z_3}\Big\rangle=\Big\langle\sum_i C(P^H_{\vec{w}_i},P^H_{\vec{w}_i},P^H_{\vec{w}_i})\Big\rangle. \tag{3.3.12}$$

We have written this term as a direct summation of the high-mode contributions from each of the grid points $\vec{w}_i$. The other term can also be expanded to be

$$\begin{aligned}\Big\langle C(\eta_iP^L_{\vec{w}_i}+P^H_{S_{grid}},\eta_iP^L_{\vec{w}_i}+P^H_{S_{grid}},\eta_iP^L_{\vec{w}_i}+P^H_{S_{grid}})\Big\rangle&=\Big\langle C(P^L_{\vec{w}_i},P^L_{\vec{w}_i},P^L_{\vec{w}_i})\Big\rangle\\&+\Big\langle\eta_i\eta_i(C(P^H_{S_{grid}},P^L_{\vec{w}_i},P^L_{\vec{w}_i})+C(P^L_{\vec{w}_i},P^H_{S_{grid}},P^L_{\vec{w}_i})+C(P^L_{\vec{w}_i},P^L_{\vec{w}_i},P^H_{S_{grid}}))\Big\rangle\\&+\Big\langle\eta_i(C(P^H_{S_{grid}},P^H_{S_{grid}},P^L_{\vec{w}_i})+C(P^H_{S_{grid}},P^L_{\vec{w}_i},P^H_{S_{grid}})+C(P^L_{\vec{w}_i},P^H_{S_{grid}},P^H_{S_{grid}}))\Big\rangle\\&+\Big\langle C(P^H_{S_{grid}},P^H_{S_{grid}},P^H_{S_{grid}})\Big\rangle.\end{aligned} \tag{3.3.13}$$

with $\langle\cdots\rangle$ here for both gauge averaging and noise averaging. A term like

$$\Big\langle\eta_i\eta_iC(P^H_{S_{grid}},P^L_{\vec{w}_i},P^L_{\vec{w}_i})\Big\rangle$$

can be expanded further as

$$\begin{aligned}\Big\langle\eta_i\eta_iC(P^H_{S_{grid}},P^L_{\vec{w}_i},P^L_{\vec{w}_i})\Big\rangle&=\Big\langle\eta_i\eta_iC(\sum_j\eta_jP^H_j,P^L_{\vec{w}_i},P^L_{\vec{w}_i})\Big\rangle\\&=\Big\langle\sum_j\eta_i\eta_i\eta_jC(P^H_{\vec{w}_j},P^L_{\vec{w}_i},P^L_{\vec{w}_i})\Big\rangle=\Big\langle C(P^H_{\vec{w}_i},P^L_{\vec{w}_i},P^L_{\vec{w}_i})\Big\rangle,\end{aligned} \tag{3.3.14}$$

which leads to contributions only from grid point $\vec{w}_i$. Applying a similar procedure to reduce other terms gives

$$\begin{aligned}\Big\langle C(\eta_iP^L_{\vec{w}_i}+P^H_{S_{grid}},\eta_iP^L_{\vec{w}_i}+P^H_{S_{grid}},\eta_iP^L_{\vec{w}_i}+P^H_{S_{grid}})\rangle&=\langle C(P^L_{\vec{w}_i},P^L_{\vec{w}_i},P^L_{\vec{w}_i})\Big\rangle\\&+\Big\langle(C(P^H_{\vec{w}_i},P^L_{\vec{w}_i},P^L_{\vec{w}_i})+C(P^L_{\vec{w}_i},P^H_{\vec{w}_i},P^L_{\vec{w}_i})+C(P^L_{\vec{w}_i},P^L_{\vec{w}_i},P^H_{\vec{w}_i}))\Big\rangle\\&+\Big\langle(C(P^H_{\vec{w}_i},P^H_{\vec{w}_i},P^L_{\vec{w}_i})+C(P^H_{\vec{w}_i},P^L_{\vec{w}_i},P^H_{S_{grid}})+C(P^L_{\vec{w}_i},P^H_{\vec{w}_i},P^H_{\vec{w}_i}))\Big\rangle\\&+\Big\langle C(P^H_{S_{grid}},P^H_{S_{grid}},P^H_{S_{grid}})\Big\rangle.\\=\Big\langle C(P^L_{\vec{w}_i}+P^H_{\vec{w}_i},P^L_{\vec{w}_i}+P^H_{\vec{w}_i},P^L_{\vec{w}_i}+P^H_{\vec{w}_i})-C(P^H_{\vec{w}_i},P^H_{\vec{w}_i},P^H_{\vec{w}_i})+\sum_j^n C(P^H_{\vec{w}_j},P^H_{\vec{w}_j},P^H_{\vec{w}_j})\Big\rangle,\end{aligned} \tag{3.3.15}$$

in which the first term is the same as $G(x, \vec{w}_i)$. Combining Eq. (3.3.10), Eq. (3.3.12) and Eq. (3.3.15), we have

$$\begin{aligned} G_{LMS}(p) =& \Big\langle \sum_x e^{-i\vec{x}\cdot\vec{p}} \Bigg(\sum_i^n [C(P^L_{\vec{w}_i} + P^H_{\vec{w}_i}, P^L_{\vec{w}_i} + P^H_{\vec{w}_i}, P^L_{\vec{w}_i} + P^H_{\vec{w}_i})] \\ &+ \sum_i^n \left[-C(P^H_{\vec{w}_i}, P^H_{\vec{w}_i}, P^H_{\vec{w}_i}) + \sum_j^n C(P^H_{\vec{w}_j}, P^H_{\vec{w}_j}, P^H_{\vec{w}_j}) \right] \\ &- (n-1) \sum_j^n C(P^H_{\vec{w}_j}, P^H_{\vec{w}_j}, P^H_{\vec{w}_j}) \Bigg) \Big\rangle \\ =& \sum_x e^{-i\vec{x}\cdot\vec{p}} \sum_i^n G(x, \vec{w}_i) = \sum_i^n e^{-i\vec{w}_i\cdot\vec{p}} \sum_x e^{-i\vec{x}\cdot\vec{p}} G(x, \vec{0}) \\ =& (\sum_i^n e^{-i\vec{w}_i\cdot\vec{p}}) G(p, \vec{0}). \end{aligned} \tag{3.3.16}$$

At this point, it is easy to see that $G_{LMS}(p)$ is a sum of contributions of $G(p, \vec{0})$ from each grid point $\vec{w}_i$ with a relative phase factor $e^{-i\vec{w}_i\cdot\vec{p}}$. With the definition of $\vec{w}_i$ and defining $\Delta \equiv \Delta_x = \Delta_y = \Delta_z$,

$$\begin{aligned} \sum_i^n e^{-i\vec{w}_i\cdot\vec{p}} &= \sum_{m_x, m_y, m_z} e^{-i(x_0 + m_x\Delta)p_x} e^{-i(y_0 + m_y\Delta)p_y} e^{-i(z_0 + m_z\Delta)p_z} \\ &= e^{-i(x_0 p_x + y_0 p_y + z_0 p_z)} \sum_{m_x} e^{-i(m_x\Delta)p_x} \sum_{m_y} e^{-i(m_y\Delta)p_y} \sum_{m_z} e^{-i(m_z\Delta)p_z}, \end{aligned} \tag{3.3.17}$$

where $\Delta = L/n_s$ in which n_s is the number of sources in each spatial direction and integers $m_{x,y,z} \in (0, 1, \cdots, L/\Delta)$. The sum $\sum_{m_x} e^{-i(m_x\Delta)p_x}$ will not be zero only if $p_x = \frac{2\pi}{L} k\, n_s$ with k some integer. For example, for the special case with $n_s = 2$ and $p_x \in \frac{2\pi}{L}\{0, 1, 2\}$, we have $\sum_{m_x} e^{-i(m_x\Delta)p_x}$ to be

$$\begin{aligned} \sum_{m_x} e^{-i(m_x\Delta)\frac{2\pi}{L}(0)} &= e^{-i0*\pi*0} + e^{-i1*\pi*0} = 2 \\ \sum_{m_x} e^{-i(m_x\Delta)\frac{2\pi}{L}(1)} &= e^{-i0*\pi*1} + e^{-i1*\pi*1} = 0 \\ \sum_{m_x} e^{-i(m_x\Delta)\frac{2\pi}{L}(2)} &= e^{-i0*\pi*2} + e^{-i1*\pi*2} = 2. \end{aligned} \tag{3.3.18}$$

By repeating this pattern, such a phase factor $\sum_i^n e^{-i\vec{w}_i\cdot\vec{p}}$ will not be zero only if $(k_x, k_y, k_z \bmod n_s = 0)$ with $\vec{p} = \frac{2\pi}{L}(k_x, k_y, k_z)$. In other words, k_x, k_y, and k_z need to be multiples of n_s so that the corresponding phase factors are non-zero.

In order to get the other missing momenta, we define another mixed grid source with additional phase factors $\theta_{i,mix}$ as

$$\begin{aligned} S_{grid,mix} &= \sum_i^n \eta_i \theta_{i,mix} S(\vec{w}_i) \\ \theta_{i,mix} &\equiv (e^{i\vec{w}_i\cdot\vec{p}_1} + e^{i\vec{w}_i\cdot\vec{p}_2} + e^{i\vec{w}_i\cdot\vec{p}_3}) \\ p_1 &\equiv \frac{2\pi}{L}(1,0,0),\ p_2 \equiv \frac{2\pi}{L}(0,1,0),\ p_3 \equiv \frac{2\pi}{L}(0,0,1), \end{aligned} \tag{3.3.19}$$

with the corresponding high-mode propagator

$$P^H_{mix} \equiv P^H_{mix}(x, S_{grid,mix}) = \sum_i \eta_i \theta_{i,mix} P^H_{\vec{w}_i}, \tag{3.3.20}$$

and define the mixed low-mode propagator

$$P^L_{\vec{w}_i,mix} \equiv P^L_{mix}(x, \vec{w}_i) = \theta_{i,mix} P^L_{\vec{w}_i}(x). \tag{3.3.21}$$

By replacing one of the propagators of $G_{LMS}(p)$ in Eq. (3.3.10) with these mixed propagators, we obtain

$$\begin{aligned} G_{LMS}(p)^{(1)} = \Big\langle \sum_x e^{-i\vec{x}\cdot\vec{p}} \Bigg(\sum_i^n [C(\eta_i P^L_{\vec{w}_i} + P^H_{S_{grid}}, \eta_i P^L_{\vec{w}_i} + P^H_{S_{grid}}, \eta_i P^L_{\vec{w}_i,mix} + P^H_{mix})] \\ -(n-1) C(P^H_{S_{grid}}, P^H_{S_{grid}}, P^H_{mix}) \Bigg) \Big\rangle, \end{aligned} \tag{3.3.22}$$

in which $G_{LMS}(p)^{(1)}$ means only one of the propagators is replaced with these mixed propagators. Take a close look at the last term,

$$\begin{aligned} \Big\langle C(P^H_{S_{grid}}, P^H_{S_{grid}}, P^H_{mix}) \Big\rangle &= \Big\langle \sum_{i,j,k} \langle \eta_i \eta_j \eta_k \rangle \theta_{k,mix} C(P^H_{\vec{w}_i}, P^H_{\vec{w}_j}, P^H_{\vec{w}_k}) \Big\rangle, \\ &= \Big\langle \sum_i \theta_{i,mix} C(P^H_{\vec{w}_i}, P^H_{\vec{w}_i}, P^H_{\vec{w}_i}) \Big\rangle. \end{aligned} \tag{3.3.23}$$

As usual, we used $\langle \eta_i \eta_j \eta_k \rangle_{Z_3} = \delta_{i,j}\delta_{j,k}$. Eq. (3.3.23) differs from Eq. (3.3.12) by a phase factor $\theta_{i,mix}$. Repeating the same derivation for the other terms in $C_{LMS}(p)^{(1)}$, we have

$$G_{LMS}(p)^{(1)} = (\sum_i^n e^{-i\vec{w}_i\cdot\vec{p}} \theta_{i,mix}) G(p, \vec{0}) \tag{3.3.24}$$

We can also replace two or three propagators in $G_{LMS}(p)$ with the mixed propagator

as

$$
\begin{aligned}
G_{LMS}(p)^{(2)} = & \Big\langle \sum_x e^{-i\vec{x}\cdot\vec{p}} \Bigg(\sum_i^n [C(\eta_i P^L_{\vec{w}_i} + P^H_{S_{grid}}, \eta_i P^L_{\vec{w}_i,mix} + P^H_{mix}, \eta_i P^L_{\vec{w}_i,mix} + P^H_{mix})] \\
& -(n-1)C(P^H_{S_{grid}}, P^H_{mix}, P^H_{mix}) \Bigg) \Big\rangle \\
= & (\sum_i^n e^{-i\vec{w}_i\cdot\vec{p}} \theta^2_{i,mix}) G(p,\vec{0}) \\
G_{LMS}(p)^{(3)} = & \Big\langle \sum_x e^{-i\vec{x}\cdot\vec{p}} \Bigg(\sum_i^n [C(\eta_i P^L_{\vec{w}_i,mix} + P^H_{mix}, \eta_i P^L_{\vec{w}_i,mix} + P^H_{mix}, \eta_i P^L_{\vec{w}_i,mix} + P^H_{mix})] \\
& -(n-1)C(P^H_{mix}, P^H_{mix}, P^H_{mix}) \Bigg) \Big\rangle \\
= & (\sum_i^n e^{-i\vec{w}_i\cdot\vec{p}} \theta^3_{i,mix}) G(p,\vec{0}),
\end{aligned}
\tag{3.3.25}
$$

Define the phase factors before $G(p,\vec{0})$ as

$$
\begin{aligned}
f_i^{(0)} &= e^{-i\vec{w}_i\cdot\vec{p}}, \\
f_i^{(1)} &= e^{-i\vec{w}_i\cdot\vec{p}} \theta_{i,mix}, \\
f_i^{(2)} &= e^{-i\vec{w}_i\cdot\vec{p}} \theta^2_{i,mix}, \\
f_i^{(3)} &= e^{-i\vec{w}_i\cdot\vec{p}} \theta^3_{i,mix},
\end{aligned}
\tag{3.3.26}
$$

which correspond to $G_{LMS}(p)^{(0)} \equiv G_{LMS}(p)$, $G_{LMS}(p)^{(1)}$, $G_{LMS}(p)^{(2)}$, $G_{LMS}(p)^{(3)}$ with

$$
G_{LMS}(p)^{(a)} = (\sum_i^n f_i^{(a)}) G(p,\vec{0}),\ a \in (0,1,2,3). \tag{3.3.27}
$$

In order to calculate the variance of $G_{LMS}(p)^{(a)}$, we start from a simple function

$$
X \equiv \sum_i g_i x_i, \tag{3.3.28}
$$

with x_i an uncorrelated random variable with central value $\overline{x}$ and variance $\sigma(x)$ and $\sum_i g_i = 1$. Then the mean value of X is,

$$
\overline{X} = \sum_i g_i \overline{x_i} = (\sum_i g_i)\overline{x} = \overline{x}. \tag{3.3.29}
$$

The variance of X is

$$\begin{aligned}
\sigma(X) &= \langle (X-\overline{X})^2 \rangle = \langle (\sum_i g_i x_i - \overline{x})^2 \rangle \\
&= \langle (\sum_i g_i (x_i - \overline{x}))^2 \rangle = \langle (\sum_i g_i^2 (x_i - \overline{x})^2) \rangle + 2 \sum_{i \neq j} g_i g_j \langle (x_i - \overline{x})(x_j - \overline{x}) \rangle \\
&= \sum_i g_i^2 \sigma(x) + 2 \sum_{i \neq j} g_i g_j \langle x_i x_j - x_i \overline{x} - x_j \overline{x} + \overline{x}^2 \rangle \\
&= \sum_i g_i^2 \sigma(x) + 2 \sum_{i \neq j} g_i g_j (\overline{x}^2 - 2\overline{x}^2 + \overline{x}^2) \\
&= \sum_i g_i^2 \sigma(x).
\end{aligned} \tag{3.3.30}$$

Assuming $G(p, \vec{0})$ from different grid points $\vec{w}_i$ have the same signals to noise ratios and ignoring errors coming from taking $\langle \eta_i \eta_j \eta_k \rangle = \delta_{i,j} \delta_{j,k}$ in Eq. (3.3.16), the theoretical ratio R of the variances of $G(p, \vec{0})$ and $G_{LMS}(p)^{(a)}$ under simple error propagator with only one inversion will be

$$R(p)^{(a)} = \frac{\sigma(G(p, \vec{0}))}{\sigma(G_{LMS}(p)^{(a)})} = \frac{(\sum_i^n f_i^{(a)})^2}{\sum_i^n (f_i^{(a)})^2}. \tag{3.3.31}$$

Since the average values of $G(p, \vec{0})$ and $G_{LMS}(p)^{(a)}$ are the same, the ratio of signal to noise ratios $G(p, \vec{0})$ and $G_{LMS}(p)^{(a)}$ is $\sqrt{(R(p)^{(a)})}$. For the case of $\vec{p} = \frac{2\pi}{L}(0,0,0)$, $f_i^{(0)} = 1$, and so $R(p)^{(a)} = n$. The variance improvement using a grid source is proportional to the number of grid points n which is the case we desire.

In order to have a feeling of other cases of $f_i^{(a)}$, we take an example of $L_x = L_y = L_z = 32$, $\Delta_x = \Delta_y = \Delta_z = \frac{32}{2} = 16$, $m_{x,y,z} \in \{0, 1\}$ and $\vec{w}_0 = (0,0,0)$. Table. 3.1 lists the $f_i^{(a)}$ and $R(p)^{(a)}$ for momentum $\vec{p} = \frac{2\pi}{L}(0,0,0)$ and $\vec{p} = \frac{2\pi}{L}(0,0,2)$. It can be seen that the f_i's for the two momenta at different cases are the same as expected. For all the cases, $R(p)^{(0)} = 8$, $R(p)^{(1)} = 0$, $R(p)^{(2)} = 3.4$ and $R(p)^{(3)} = 0$. This means that we should use case $G_{LMS}^{(0)}(p)$ to obtain better signals for these two momenta and case $G_{LMS}^{(1)}(p)$ and $G_{LMS(p)}^{(2)}(p)$ will have no signal for these momenta. With the observation of patterns, for the case with $\vec{p} = \frac{2\pi}{L}(k_x, k_y, k_z)$, $k_{x,y,z}$ to be modulo (2), the best case is $G_{LMS}^{(0)}(p)$ with theoretical improvement of a factor of 8 which corresponds to all $f_i^{(0)} = 1$.

Table 3.1: List of $f_i^{(a)}$ and $R(p)^{(a)}$ for momenta $\vec{p} = \frac{2\pi}{L}(0,0,0)$ and $\vec{p} = \frac{2\pi}{L}(0,0,2)$.

$\vec{p}$	Case	f_0	f_1	f_2	f_3	f_4	f_5	f_6	f_7	$R(p)$
$\frac{2\pi}{L}(0,0,0)$	(0)	1	1	1	1	1	1	1	1	8
$\frac{2\pi}{L}(0,0,0)$	(1)	3	1	-1	1	1	-1	-1	-3	0
$\frac{2\pi}{L}(0,0,0)$	(2)	9	1	1	1	1	1	1	9	3.4
$\frac{2\pi}{L}(0,0,0)$	(3)	27	1	1	-1	1	-1	-1	-27	0
$\frac{2\pi}{L}(0,0,2)$	(0)	1	1	1	1	1	1	1	1	8
$\frac{2\pi}{L}(0,0,2)$	(1)	3	1	-1	1	1	-1	-1	-3	0
$\frac{2\pi}{L}(0,0,2)$	(2)	9	1	1	1	1	1	1	9	3.4
$\frac{2\pi}{L}(0,0,2)$	(3)	27	1	1	-1	1	-1	-1	-27	0

Picking only the best cases for the chosen momenta, we can have the ratios listed in Table. 3.2. It can been seen that we have reached the theoretical improvement of 8 only for $\vec{p} = \frac{2\pi}{L}(0,0,0)$ and for some momenta the improvements from using grid source are much smaller, though still worthwhile.

Table 3.2: List of $f_i^{(a)}$ and $R(p)^{(a)}$ for momenta $\vec{p} = \frac{2\pi}{L}(0,0,0)$, $\vec{p} = \frac{2\pi}{L}(0,0,1)$, $\vec{p} = \frac{2\pi}{L}(0,1,1)$ and $\vec{p} = \frac{2\pi}{L}(1,1,1)$.

$\vec{p}$	Case	f_0	f_1	f_2	f_3	f_4	f_5	f_6	f_7	$R(p)$
$\frac{2\pi}{L}(0,0,0)$	(0)	1	1	1	1	1	1	1	1	8
$\frac{2\pi}{L}(0,0,1)$	(1)	3	-1	1	1	1	1	-1	3	2.6
$\frac{2\pi}{L}(0,1,1)$	(2)	9	-1	-1	1	1	-1	-1	9	1.5
$\frac{2\pi}{L}(1,1,1)$	(3)	27	-1	-1	-1	-1	-1	-1	27	1.6

Repeating these tests with a different starting point $\vec{w}_0 = (0,0,4)$ of the noise grid source defined in Eq. (3.3.7), the $R(p)^{(a)}$'s in Table. 3.2 change to $R(\frac{2\pi}{L}(0,0,0))^{(0)} = 8$, $R(\frac{2\pi}{L}(0,0,1))^{(1)} = 4$, $R(\frac{2\pi}{L}(0,1,1))^{(2)} = 2.2$ and $R(\frac{2\pi}{L}(1,1,1))^{(3)} = 2.3$. Since $R(p)^{(a)}$ can vary by a factor of 2 for cases (1), (2) and (3), it would be better if we could have other ways to deal with LMS with momenta so that f_i will all be 1 for all sites so that we can have theoretical improvement approaching the number of grid points n. This will be achieved in next section.

New way of using mixed momenta

Taking a close look at Eq. (3.3.10), we can try to add additional phases $e^{i\vec{w}_i\cdot\vec{p}}$ for the contractions of each grid point as

$$G_{LMS}(p)^{new,try} = \sum_i^n e^{i\vec{w}_i\cdot\vec{p}} \sum_x e^{-i\vec{x}\cdot\vec{p}} \Big\langle [C(\eta_i P^L_{\vec{w}_i} + P^H_{S_{grid}}, \eta_i P^L_{\vec{w}_i} + P^H_{S_{grid}}, \eta_i P^L_{\vec{w}_i} + P^H_{S_{grid}})] - C(P^H_{S_{grid}}, P^H_{S_{grid}}, P^H_{S_{grid}}) \Big\rangle \tag{3.3.32}$$

Expand the contributions from each of the grid point of $G_{LMS}(p)^{new,try}$ to have,

$$\begin{aligned} G_{LMS}(p)^{new,try} &= \sum_i^n e^{i\vec{w}_i\cdot\vec{p}} \sum_x e^{-i\vec{x}\cdot\vec{p}} \\ &\Big\langle \Big[C(P^L_{\vec{w}_i}+P^H_{\vec{w}_i}, P^L_{\vec{w}_i}+P^H_{\vec{w}_i}, P^L_{\vec{w}_i}+P^H_{\vec{w}_i}) - C(P^H_{\vec{w}_i}, P^H_{\vec{w}_i}, P^H_{\vec{w}_i}) + \cancel{\sum_j^n C(P^H_{\vec{w}_j}, P^H_{\vec{w}_j}, P^H_{\vec{w}_j})} \Big] \\ &\quad \cancel{- \sum_j^n C(P^H_{\vec{w}_i}, P^H_{\vec{w}_i}, P^H_{\vec{w}_i})} \Big\rangle \\ &= \sum_i^n e^{i\vec{w}_i\cdot\vec{p}} \sum_x e^{-i\vec{x}\cdot\vec{p}} \Big\langle C(P_{\vec{w}_i}, P_{\vec{w}_i}, P_{\vec{w}_i}) - C(P^H_{\vec{w}_i}, P^H_{\vec{w}_i}, P^H_{\vec{w}_i}) \Big\rangle \end{aligned} \tag{3.3.33}$$

With Eq. (3.3.4) we can have

$$\begin{aligned} G_{LMS}(p)^{new,try} &= \sum_i^n e^{i\vec{w}_i\cdot\vec{p}} G(p,\vec{w}_i) - \sum_i^n e^{i\vec{w}_i\cdot\vec{p}} \sum_x e^{-i\vec{x}\cdot\vec{p}} \Big\langle C(P^H_{\vec{w}_i}, P^H_{\vec{w}_i}, P^H_{\vec{w}_i}) \Big\rangle \\ &= \sum_i^n e^{i\vec{w}_i\cdot\vec{p}} e^{-i\vec{w}_i\cdot\vec{p}} G(p,\vec{0}) - \sum_i^n e^{i\vec{w}_i\cdot\vec{p}} \sum_x e^{-i\vec{x}\cdot\vec{p}} \Big\langle C(P^H_{\vec{w}_i}, P^H_{\vec{w}_i}, P^H_{\vec{w}_i}) \Big\rangle \\ &= \sum_i^n G(p,\vec{0}) - \sum_i^n e^{i\vec{w}_i\cdot\vec{p}} \sum_x e^{-i\vec{x}\cdot\vec{p}} \Big\langle C(P^H_{\vec{w}_i}, P^H_{\vec{w}_i}, P^H_{\vec{w}_i}) \Big\rangle \end{aligned} \tag{3.3.34}$$

Thus we can have $G_{LMS}(p)^{new,try}$ to be $nG(p,\vec{0})$ with even contributions from each of the grid points (with all $f_i = 1$) for all momenta if the last term can be evaluated. Note that the last term is only a function of the high-mode part of the propagator and we will see later that the contribution from this term to the correlation function is very small at large time slices.

Let us first define $G^{(H,H,H)}(p)$ to be the last term as

$$G^{(H,H,H)}(p) = \sum_i^n e^{i\vec{w}_i\cdot\vec{p}} \sum_x e^{-i\vec{x}\cdot\vec{p}} \Big\langle C(P^H_{\vec{w}_i}, P^H_{\vec{w}_i}, P^H_{\vec{w}_i}) \Big\rangle. \tag{3.3.35}$$

Also define the "high mode part" of the point source correlation functions as

$$G^H(p) \equiv \sum_x e^{-i\vec{x}\cdot\vec{p}} G^H(x,\vec{0}) \equiv \sum_x e^{-i\vec{x}\cdot\vec{p}} \langle C(P^H(x,\vec{0}), P^H(x,\vec{0}), P^H(x,\vec{0})) \rangle \tag{3.3.36}$$

Assume translation invariance of $G^H(x,\vec{0})$ as

$$\begin{aligned} G^H(x,\vec{0}) &= G^H((\vec{x}+\vec{w},t),\vec{w}) \\ &= \langle C(P^H_{\vec{w}}(\vec{x}+\vec{w},t), P^H_{\vec{w}}(\vec{x}+\vec{w},t), P^H_{\vec{w}}(\vec{x}+\vec{w},t)) \rangle \end{aligned} \tag{3.3.37}$$

Then we can re-write $G^{(H,H,H)}(p)$ with the change of $\vec{x} \to \vec{x} + \vec{w}_i$ as

$$\begin{aligned} G^{(H,H,H)}(p) = \sum_i^n e^{i\vec{w}_i\cdot\vec{p}} \sum_x e^{-i(\vec{x}+\vec{w}_i)\cdot\vec{p}} \\ \Big\langle C(P^H_{\vec{w}_i}(\vec{x}+\vec{w}_i,t), P^H_{\vec{w}_i}(\vec{x}+\vec{w}_i,t), P^H_{\vec{w}_i}(\vec{x}+\vec{w}_i,t)) \Big\rangle \end{aligned} \tag{3.3.38}$$

Use translation invariance in Eq. (3.3.37), we have

$$\begin{aligned} G^{(H,H,H)}(p) &= \sum_i^n e^{i\vec{w}_i\cdot\vec{p}} \sum_x e^{-i(\vec{x}+\vec{w}_i)\cdot\vec{p}} G^H((\vec{x}+\vec{w},t),\vec{w}) \\ &= \sum_i^n \sum_x e^{-i(\vec{x})\cdot\vec{p}} G^H(x,\vec{0}) \\ &= \sum_i^n G^H(p,\vec{0}) = nG^H(p,\vec{0}). \end{aligned} \tag{3.3.39}$$

Thus we can find a way to estimate $G^H(p,\vec{0})$ to get $G^{(H,H,H)}(p)$. One way of doing so is using the high mode part of the mixed momenta propagator in Eq. (3.3.20) and defining the following contractions for high-mode propagators with mixed propagator inspired from Sec. 3.3 as

$$\begin{aligned} G(p)^{H,(0)} &= \langle \sum_x e^{-i\vec{x}\cdot\vec{p}} \left(C(P^H,P^H,P^H)\right)\rangle = (\sum_i^n e^{-i\vec{w}_i\cdot\vec{p}}) G^H(p,\vec{0}) \\ G(p)^{H,(1)} &= \langle \sum_x e^{-i\vec{x}\cdot\vec{p}} \left(C(P^H,P^H,P^H_{mix})\right)\rangle = (\sum_i^n e^{-i\vec{w}_i\cdot\vec{p}}\theta_{i,mix}) G^H(p,\vec{0}) \\ G(p)^{H,(2)} &= \langle \sum_x e^{-i\vec{x}\cdot\vec{p}} \left(C(P^H,P^H_{mix},P^H_{mix})\right)\rangle = (\sum_i^n e^{-i\vec{w}_i\cdot\vec{p}}\theta^2_{i,mix}) G^H(p,\vec{0}) \\ G(p)^{H,(3)} &= \langle \sum_x e^{-i\vec{x}\cdot\vec{p}} \left(C(P^H_{mix},P^H_{mix},P^H_{mix})\right)\rangle = (\sum_i^n e^{-i\vec{w}_i\cdot\vec{p}}\theta^3_{i,mix}) G^H(p,\vec{0}), \end{aligned} \tag{3.3.40}$$

in which $G(p)^{H,(a)} = (\sum_i^n f_i^{(a)}) G^H(p,\vec{0})$ with $f_i^{(a)}$ having the same definition as in Eq. (3.3.26). We can choose case $G(p)^{H,(a)}$ to be an estimator of $G^H(p,\vec{0})$ so that $G^{(H,H,H)}(p) = nG^H(p,\vec{0})$ depending on the desired momentum p. Even $f_i^{(a)}$ is not equal to 1 which will have influence on the signal of $G^{(H,H,H)}(p)$, this should not affect the final signal of the nucleon correlation functions. This can be seen from Fig 3.2 and Fig 3.3 that $C^H(p)$ is a very small part of the total correlation function. In the figure, we defined $G^{L,H}(p,\vec{0}) = G(p,\vec{0}) - G^L(p,\vec{0}) - G^H(p,\vec{0})$ in which $G^L(p,\vec{0})$ is constructed from low-mode propagators. From this plot, it can be seen that at around 1.0 fm most of the contributions and errors come from the low-mode $G^L(p,\vec{0})$. And the pure high mode $G^H(p,\vec{0})$ contribution is under 1% after 0.75 fm. The test is on a $32^3 \times 64$ domain wall lattice (32ID) with lattice spacing 0.143 fm.

Another issue for the new contractions is that we have two sources in time. The method in Ref.[40, 1] proposed a combination of the two time slices as

$$S_{i,j} \equiv S(\vec{w}_i, 0) + S(\vec{w}_j, 32), \tag{3.3.41}$$

in which $\vec{w}_i$ and $\vec{w}_j$ are the spacial positions on time slices 0 and 32, respectively, — they are chosen so that the distance between $\vec{w}_j$ and $\vec{w}_i$ is as large as possible to reduce the influence between them — and then constructing a low-mode propagator for this

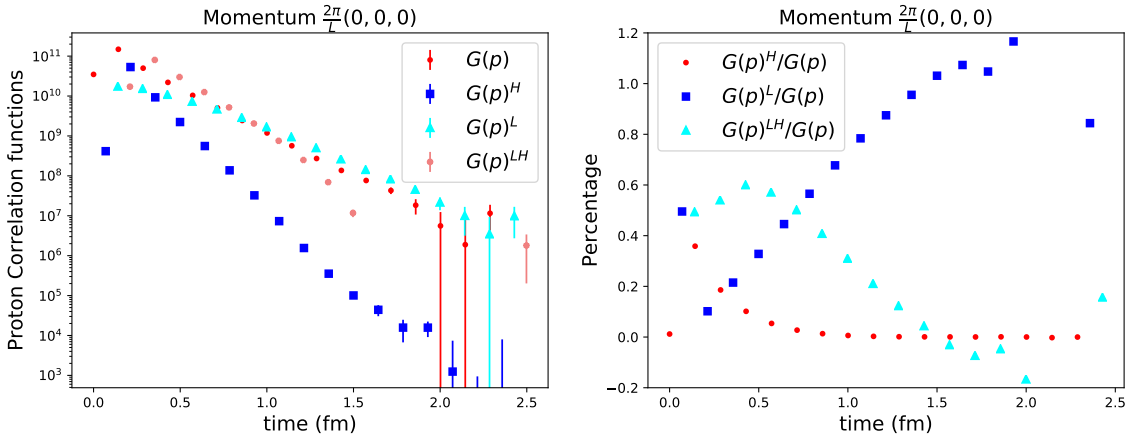

Figure 3.2: Example plots of the high-mode and low-mode contributions to proton smeared to the smeared correlation functions at momentum $\frac{2\pi}{L}(0,0,0)$ with pion mass 174 MeV. The plot on the left is of the correlation functions $G^L(p,\vec{0})$ and the contributions from $G^L(p,\vec{0})$, $G^H(p,\vec{0})$ and the crossing term $G^{L,H}(p,\vec{0}) = G(p,\vec{0}) - G^L(p,\vec{0}) - G^H(p,\vec{0})$. The plot on the right shows the relative proportions of these three terms which add up to 1.

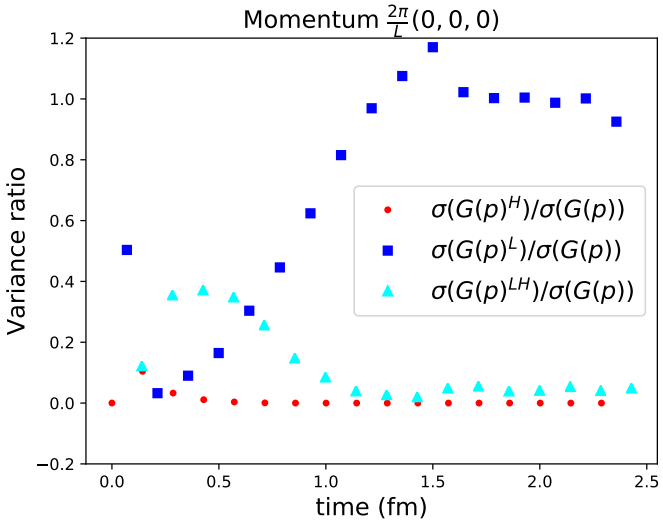

Figure 3.3: Example plot of the ratio of the variance of these three terms shown in Fig. 3.2 to the variance of total correlation function $G(p,\vec{0})$. The ratio $\sigma(G(p)^H)/\sigma(G(p))$ is almost zero as the contribution from pure high mode to the nucleon correlation function is very small.

combined source $S_{i,j}$. For the new method, since there is an additional phase $e^{i\vec{w}_i\cdot\vec{p}}$ factor for each of the grid points, so the current implementation using the grouping of sources is

$$S_{i,i} \equiv S(\vec{w}_i, 0) + S(\vec{w}_i, 32), \tag{3.3.42}$$

in which the spacial positions on time slice 0 and 32 are the same to avoid complexity from the additional phase factor. The results of the new method to get momenta with low-mode substitution are shown in Fig 3.4. It can be seen that it gives consistent results with the previous method and has better signals at momenta $\frac{2\pi}{L}(0,1,1)$ and $\frac{2\pi}{L}(1,1,1)$. And the new method requires only one fourth of the contraction time compared with the original method which requires contraction of $C_{LMS}(p)^{(a)}$ in Eq. (3.3.10), Eq. (3.3.22) and Eq. (3.3.25) with $a \in \{0,1,2,3\}$.

In summary the new methods states

$$\begin{aligned} G_{LMS}(p)^{new} &= \sum_i^n e^{i\vec{w}_i\cdot\vec{p}} \sum_x e^{-i\vec{x}\cdot\vec{p}} \Big\langle [C(\eta_i P^L_{\vec{w}_i} + P^H_{S_{grid}}, \eta_i P^L_{\vec{w}_i} + P^H_{S_{grid}}, \eta_i P^L_{\vec{w}_i} + P^H_{S_{grid}})] \\ &\quad - C(P^H_{S_{grid}}, P^H_{S_{grid}}, P^H_{S_{grid}}) \Big\rangle + G^{(H,H,H)}(p) \end{aligned} \tag{3.3.43}$$

with $G^{(H,H,H)}(p) = nG^H(p,\vec{0})$ calculated with Eq. (3.3.40) under the assumption of translation invariance in Eq. (3.3.37).

There may be several other possibilities to estimate $G^{(H,H,H)}(p)$ all of which need an additional inversion as the above method (inversion for the mixed momenta propagator):

- The first one is to have an additional inversion of the high-mode propagator with Z_4 noises β_i with source and high-mode propagator as

$$\begin{aligned} S^{Z_4}_{grid} &\equiv \sum_i^n \beta_i S(\vec{w}_i) \\ P^H(x, S^{Z_4}_{grid}) &= \sum_i^n \beta_i P^H_{\vec{w}_i}(x). \end{aligned} \tag{3.3.44}$$

  Defining $P^H_{Z_4} = P^H(x, S^{Z_4}_{grid})$, by using $\langle \beta_i\beta_j\beta_k\beta_m\rangle = \delta_{i,j}\delta_{j,k}\delta_{k,m}$ and $\beta_i\beta_i\beta_i\beta_i = 1$, we have

$$\begin{aligned} &\langle \sum_i^n e^{i\vec{w}_i\cdot\vec{p}} \sum_x e^{-i\vec{x}\cdot\vec{p}} \beta_i C(P^H_{Z_4}, P^H_{Z_4}, P^H_{Z_4})\rangle \\ &= \langle \sum_i^n e^{i\vec{w}_i\cdot\vec{p}} \sum_x e^{-i\vec{x}\cdot\vec{p}} \beta_i \sum_{j,k,m}^n \beta_j\beta_k\beta_m C(P^H_{\vec{w}_j}, P^H_{\vec{w}_k}, P^H_{\vec{w}_m})\rangle \\ &= \langle \sum_i^n e^{i\vec{w}_i\cdot\vec{p}} \sum_x e^{-i\vec{x}\cdot\vec{p}} C(P^H_{\vec{w}_j}, P^H_{\vec{w}_k}, P^H_{\vec{w}_m})\rangle \\ &= G^{(H,H,H)}(p), \end{aligned} \tag{3.3.45}$$

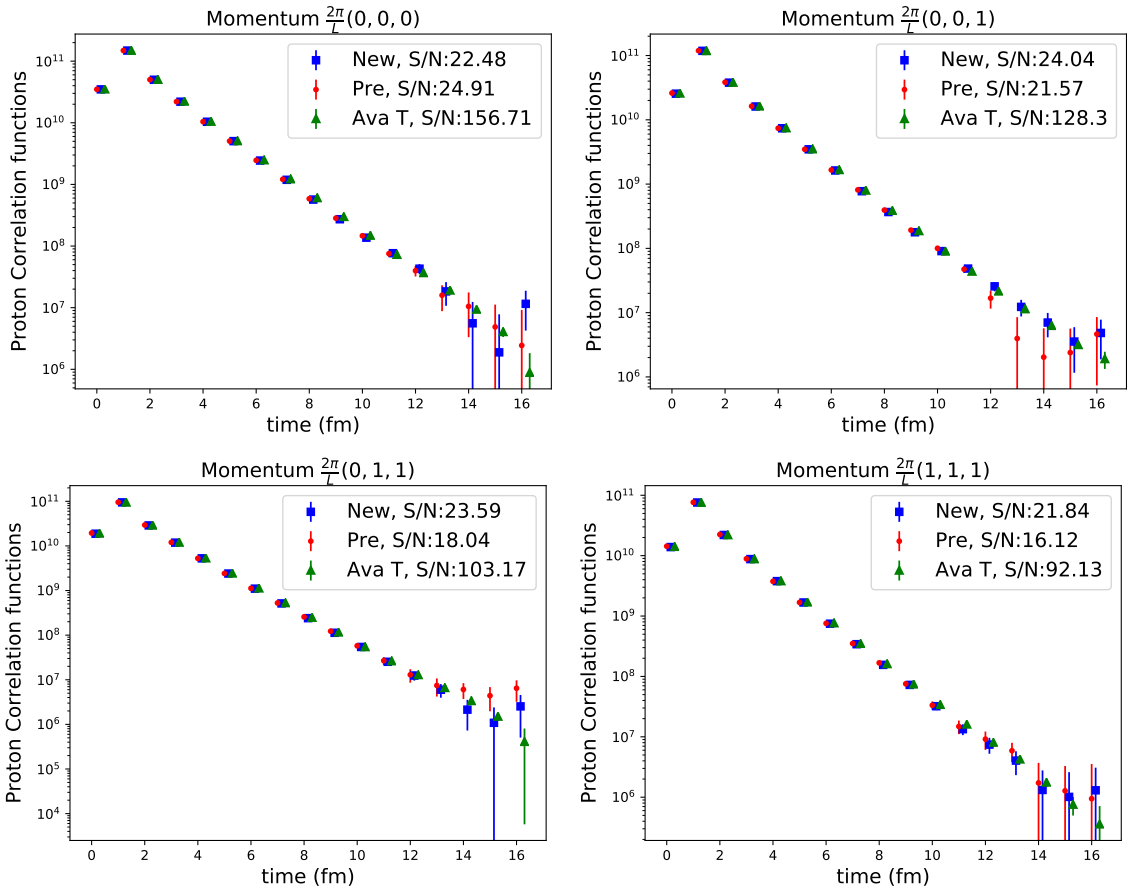

Figure 3.4: The four plots are used to compare the previous method and new method to get momenta with low-mode substitution for proton smeared to smeared correlation functions. The blue points correspond to the new method (New) to deal with momenta measured on 50 configurations. The red points correspond to the previous method (Pre) to deal with momenta measured on 50 configurations and green points (Ava) use the same method with 16 different initial time sources averaged on 200 configurations. The four plots correspond to the cases of momenta $\frac{2\pi}{L}(0,0,0)$, $\frac{2\pi}{L}(0,0,1)$, $\frac{2\pi}{L}(0,1,1)$,$\frac{2\pi}{L}(1,1,1)$ averaged over equivalent directions. S/N in the plot labels the signal to noise ratio at $t = 8$.

which gives $G^{(H,H,H)}(p)$ without the assumption of translation invariance in Eq. (3.3.37).

- Another possibility is that we can use two Z_3 noise grid sources with the same grid points $\vec{w}_i$ but different noises η_i^α and η_i^β as

$$\begin{aligned} S^\alpha_{grid} \equiv \sum_i^n \eta_i^\alpha S(\vec{w}_i), S^\beta_{grid} \equiv \sum_i^n \eta_i^\beta S(\vec{w}_i) \\ P^H(x, S^\alpha_{grid}) = \sum_i^n \eta_i^\alpha P^H_{\vec{w}_i}(x), P^H(x, S^\beta_{grid}) = \sum_i^n \eta_i^\beta P^H_{\vec{w}_i}(x). \end{aligned} \tag{3.3.46}$$

From these two high-mode propagators, we can construct $C^{(H,H,H)}(p)$ in a similar procedure as the Z_4 noise case as (defining $P^{H,\alpha} = P^H(x, S^\alpha_{grid})$ and $P^{H,\beta} = P^H(x, S^\beta_{grid})$)

$$\begin{aligned} &\langle \sum_i^n e^{i\vec{w}_i\cdot\vec{p}} \sum_x e^{-i\vec{x}\cdot\vec{p}} \eta_i^\alpha {\eta_i^\beta}^2 C(P^{H,\alpha}, P^{H,\alpha}, P^{H,\beta})\rangle \\ &= \langle \sum_i^n e^{i\vec{w}_i\cdot\vec{p}} \sum_x e^{-i\vec{x}\cdot\vec{p}} \eta_i^\alpha {\eta_i^\beta}^2 \sum_{j,k,m}^n \eta_j^\alpha \eta_k^\alpha \eta_m^\beta C(P^H_{\vec{w}_j}, P^H_{\vec{w}_k}, P^H_{\vec{w}_m})\rangle \\ &= \langle \sum_i^n e^{i\vec{w}_i\cdot\vec{p}} \sum_x e^{-i\vec{x}\cdot\vec{p}} C(P^H_{\vec{w}_j}, P^H_{\vec{w}_k}, P^H_{\vec{w}_m})\rangle \\ &= G^{(H,H,H)}(p), \end{aligned} \tag{3.3.47}$$

which also gives $G^{(H,H,H)}(p)$ without the assumption of translation invariance in Eq. (3.3.37). As S^α_{grid} and S^β_{grid} have no additional phases other than the Z_3 noise, we can construct $G_{LMS}(p)^{new,\alpha}$ and $G_{LMS}(p)^{new,\beta}$ along with the above estimation of $G^{(H,H,H)}(p)$. Averaging these two correlation functions may give us better signals around $0.5 \sim 1.0$ fm. We may also try to have several different spatial grids on one configuration; we can estimate $G^{(H,H,H)}(p)$ on each configuration once and use it for all other different spatial grids which will save around half the inversion time and storage of propagators. These cases need to be tested further in realistic calculations.

3.4 Three-point functions

Pion three-point functions

On the lattice we approach the charge, matter and spin of hadron by calculating matrix elements $\langle h|\,\mathcal{O}\,|h'\rangle$. A simple case is the electromagnetic form factor of the pion which is defined by

$$\langle \pi^+(p_f)|\,V_\mu\,|\pi^+(p_i)\rangle = (p_f + p_i)_\mu f_{\pi\pi}(Q^2), \tag{3.4.1}$$

in which p_i and p_f are the momenta of the initial and final pion, $Q^2 = (p_f - p_i)^2$ is the space-like momentum transfer, and V_μ is the local vector current

$$V_\mu \ = \tfrac{2}{3}\bar{u}\gamma_\mu u - \tfrac{1}{3}\bar{d}\gamma_\mu d, \tag{3.4.2}$$

in which $\frac{2}{3}$ and $-\frac{1}{3}$ are the charges of the up and down quarks. On the lattice we calculate the three-point function in momentum space as

$$C_{3\text{pt}}(\tau, t_f, \vec{p}_i, \vec{p}_f) = \sum_{\vec{x}_f, \vec{z}} e^{-i\vec{p}_f\cdot\vec{x}_f} e^{i\vec{q}\cdot\vec{z}} \left\langle \text{Tr}[\mathcal{O}_{\pi^+}(x_f) V_\mu(z) \mathcal{O}^\dagger_{\pi^+}(\mathcal{G})] \right\rangle \tag{3.4.3}$$

where $\mathcal{O}_{\pi^+}(\vec{x}, t) = \bar{d}(\vec{x}, t)\gamma_5 u(\vec{x}, t)$ is the interpolating field of the pion, $\mathcal{G}$ is the smeared Z_3-noise grid source [39] at time slice 0, $z \equiv \{\tau, \vec{z}\}$ is the current position, 0 is the position where the pion is created, $x_f \equiv \{t_f, \vec{x}_f\}$ is the position where the pion is annihilated, $\vec{p}_i$ and $\vec{p}_f$ is the initial and final momentum of the pion, respectively, and $\vec{q} = \vec{p}_f - \vec{p}_i$ is the momentum transfer. With the usage of Wick contraction, we can calculate $C_{3\text{pt}}(\tau, t_f, \vec{p}_i, \vec{p}_f)$ for V_μ current as

$$\begin{aligned}
&C_{3\text{pt}}(\tau, t_f, \vec{p}_i, \vec{p}_f) = \sum_{\vec{x}_f, \vec{z}} e^{-i\vec{p}_f\cdot\vec{x}_f} e^{i\vec{q}\cdot\vec{z}} \times \\
&\Big\langle \text{Tr}\Big[-\frac{2}{3}\gamma_5 D_u^{-1}(x_f|z)\gamma_\mu D_u^{-1}(z|\mathcal{G})\gamma_5 D_d^{-1}(\mathcal{G}|x_f) \\
&\quad + \frac{1}{3}\gamma_5 D_d^{-1}(\mathcal{G}|z)\gamma_\mu D_d^{-1}(z|x_f)\gamma_5 D_u^{-1}(x_f|\mathcal{G}|)\Big] \\
&\quad + \text{Tr}\left[\gamma_5 D_u^{-1}(x_f|\mathcal{G})\gamma_5 D_d^{-1}(\mathcal{G}|x_f)\right] \times \left(\frac{2}{3}\text{Tr}\left[\gamma_\mu D_u^{-1}(z|z)\right] - \frac{1}{3}\text{Tr}\left[\gamma_\mu D_d^{-1}(z|z)\right]\right) \Big\rangle,
\end{aligned} \tag{3.4.4}$$

where $D_f^{-1}(y|x)$ is the quark propagator from x to y for quark flavor f, and $\vec{q} = \vec{p}_f - \vec{p}_i$ is the momentum transfer. The first two terms which include propagator $D_u^{-1}(x_f|z)$ or $D_d^{-1}(z|x_f)$ are so-called connected insertions (CI). The last two terms including propagator $D_u^{-1}(z|z)$ or $D_d^{-1}(z|z)$ are called disconnected insersions (DI) which are proven to vanish [41] in the ensemble average because of charge conjugation symmetry. Let us consider the CI terms associated with the current $\bar{u}\gamma_\mu u$ separately as

$$\begin{aligned}
&\gamma_5 D_u^{-1}(x_f|z)\gamma_\mu D_u^{-1}(z|\mathcal{G})\gamma_5 D_d^{-1}(\mathcal{G}|x_f) \\
&\qquad = -(\gamma_5 D_d^{-1}(\mathcal{G}|z)\gamma_\mu D_d^{-1}(z|x_f)\gamma_5 D_u^{-1}(x_f|\mathcal{G}))^\dagger,
\end{aligned} \tag{3.4.5}$$

where we have used the γ_5 hermiticity of the propagator discussed in Eq. (2.4.5), the "$-$" sign comes from $\gamma_5\gamma_\mu^\dagger\gamma_5 = -\gamma_\mu$. As we are working with exact isospin symmetry, we have $D_u^{-1}(y|x) = D_d^{-1}(y|x)$. And $C_{3\text{pt}}(\tau, t_f, \vec{p}_i, \vec{p}_f)$ will have signals only for the real part ($C_{3\text{pt}} = C^*_{3\text{pt}}$ under charge conjugation [41]), we can sum up the two terms from CI parts to have

$$\begin{aligned}
C_{3\text{pt}}(\tau, t_f, \vec{p}_i, \vec{p}_f) = &\sum_{\vec{x}_f, \vec{z}} e^{-i\vec{p}_f\cdot\vec{x}_f} e^{i\vec{q}\cdot\vec{z}} \times \\
&\left\langle \text{Tr}\left[\gamma_5 D^{-1}(\mathcal{G}|z)\gamma_\mu D^{-1}(z|x_f)\gamma_5 D^{-1}(x_f|\mathcal{G})\right] \right\rangle,
\end{aligned} \tag{3.4.6}$$

in which $D_f^{-1}(y|x)$ denotes the light (u or d) quark propagator from x to y. In practice, $D^{-1}(\mathcal{G}|z)$ in Eq. (3.4.6) is calculated with γ_5 hermiticity, i.e., $D^{-1}(\mathcal{G}|z) = \gamma_5 D^{-1}(z|\mathcal{G})^\dagger \gamma_5$, and $D^{-1}(z|x_f)$ is usually obtained in the sequential source method with $\gamma_5 D^{-1}(x_f|\mathcal{G})$ as the source [42, 43]. The calculation of the sequential propagators would need to be repeated for different $\vec{p}_f$ and different quark mass m, thus the cost would be very high when dozens of momenta and multiple quark masses are calculated. Instead, we use the stochastic sandwich method [40, 1], but without low mode substitution (LMS) for $D^{-1}(x_f|\mathcal{G})$ since it is not efficient for pseudoscalar mesons [29]. However, the separation of sink position x_f and current position z in splitting the low and high modes for the propagator $D^{-1}(z|x_f)$ between the current and sink can facilitate FFT along with LMS which is still useful here. As shown in Fig. 3.5, $D^{-1}(z|x_f)$ can be split into the exact low mode part based on the low lying overlap eigenvalues λ_i and eigenvectors v_i of the ith eigenmode of D_c, plus the noise-source estimate $D^{-1}_{H,\mathrm{noi}}$ of the high-mode part,

$$\begin{aligned} D^{-1}(z|x_f) &= D_L^{-1}(z|x_f) + D_H^{-1}(z|x_f), \\ D_L^{-1}(z|x_f) &= \sum_{\lambda_i \le \lambda_c} \frac{1}{\lambda_i + m} v_i(z) v_i^\dagger(x_f), \\ D_H^{-1}(z|x_f) &= \frac{1}{n_f} \sum_{j=1}^{n_f} D^{-1}_{H,\mathrm{noi}}(z, \eta_j) \eta_j^\dagger(x_f), \end{aligned} \tag{3.4.7}$$

where λ_c is the highest eigenvalue in LMS and is much larger than the quark mass m with the typical number of eigenmodes $n_\mathrm{v} \sim 400$ on 24I and 32I, and $n_\mathrm{v} \sim 1800$ on 32ID, 32IDh, 24IDc and 48I; and $D^{-1}_{H,\mathrm{noi}}(z, \eta_j)$ is the noise-estimated propagator for the high modes with the low-mode deflated Z_3 noise $\eta_j(x_f)$ [40, 1]. We generate n_f sets of $D^{-1}_{H,\mathrm{noi}}$ and each inversion includes $2\,n_t$ sink time slices at $i\frac{T}{n_t}t'$ and $T - i\frac{T}{n_t}t'$ with $i = \{1 \cdots n_t\}$ to increase statistics.

Thus $C_{3\mathrm{pt}}$ can be decomposed into factorized forms within the sums of the eigenmodes for the low modes and the n_f number of noises η_j for the high modes,

$$\begin{aligned} C_{3\mathrm{pt}}(\tau, t_f, \vec{p}_i, \vec{p}_f) = \Big\langle & \sum_{\lambda_i \le \lambda_c} \mathrm{Tr}[\frac{1}{\lambda_i + m} G_i^L(\vec{q}, \tau) F_i^L(\vec{p}_f, t_f)] \\ & + \sum_{j=1}^{n_f} \frac{1}{n_f} \mathrm{Tr}[G_j^H(\vec{q}, \tau) F_j^H(\vec{p}_f, t_f)] \Big\rangle, \end{aligned} \tag{3.4.8}$$

where

$$G_i^L(\vec{q}, \tau) = \sum_{\vec{z}} e^{i\vec{q}\cdot\vec{z}} \gamma_5 D^{-1}(\mathcal{G}|z) \gamma_\mu v_i(z), \tag{3.4.9}$$

$$F_i^L(\vec{p}_f, t_f) = \sum_{\vec{x}_f} e^{-i\vec{p}_f\cdot\vec{x}_f} v_i^\dagger(x_f) \gamma_5 D^{-1}(x_f|\mathcal{G}), \tag{3.4.10}$$

$$G_j^H(\vec{q}, \tau) = \sum_{\vec{z}} e^{i\vec{q}\cdot\vec{z}} \gamma_5 D^{-1}(\mathcal{G}|z) \gamma_\mu D^{-1}_{H,\mathrm{noi}}(z, \eta_j), \tag{3.4.11}$$

$$F_j^H(\vec{p}_f, t_f) = \sum_{\vec{x}_f} e^{-i\vec{p}_f\cdot\vec{x}_f} \eta_j^\dagger(x_f) \gamma_5 D^{-1}(x_f|\mathcal{G}), \tag{3.4.12}$$

which are calculated by using FFTs on the spatial points $\vec{z}$ and $\vec{x}_{\rm f}$ for each G_i^L, F_i^L, G_j^H and F_j^H to obtain any $\vec{q}$ and $\vec{p}_f$ with the computational complexity $\mathcal{O}(V\log V)$ with V the lattice spatial volume. Compared with the stochastic sandwich method for a fixed $\vec{p}_f$ which also includes the summation over the spatial points $\vec{z}$ and $\vec{x}_{\rm f}$, eigenvectors v_i and noises η_j, the additional cost factor of using FFTs namely $\mathcal{O}(\log V)$, is only of order ~ 7 for our largest 48I lattice. The cost factor for the traditional stochastic sandwich method is proportional to order ~ 100 if we would like to have more than seven different sink momenta $\vec{p_f}$ and average over different directions. This allows us to calculate any combination of $\vec{q}$ and $\vec{p_f}$ without much additional cost compared to the traditional stochastic sandwich method.

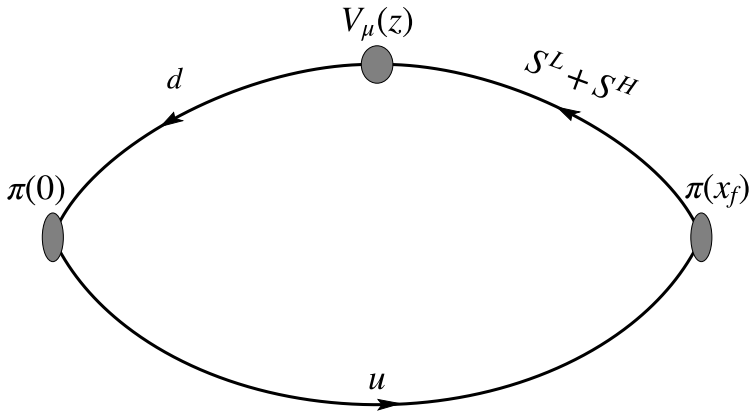

Figure 3.5: Illustration of the pion three-point function with the stochastic sandwich method. LMS is applied for the propagator between the current at z and the sink at x_f with FFT, but not for the propagators from the source at 0.

The source smearing of this FFT contraction is implemented by replacing the source propagator $D^{-1}(z|0)$ with the smeared propagator $D^{-1}(z|\mathcal{G}_S)$

$$D^{-1}(z|\mathcal{G}_S)^{c_1,a}_{\gamma_1\gamma_2} \equiv \sum_{\vec{z}_2} \mathcal{D}^{-1}(\{\vec{z}_1, y_t\}, \{\mathcal{G}(\vec{z}_2), 0\})^{c_1,c_2}_{\gamma_1\gamma_2} S(\vec{x}, \vec{z}_2)^{a,c_2}_{\alpha,\gamma_2} \tag{3.4.13}$$

with S is the smearing function defined in Sec. 3.2. Sink smearing is applied on all the sink spatial points x_f of noise $\eta_j(x_f)$ and eigenvectors $v_i^\dagger(x_f)$ which need to be done carefully for each of the propagators. First, we replace propagator $D^{-1}(x_f|\mathcal{G})$ with $D^{-1}(x_f|\mathcal{G}_S)$ which is the propagator with source smearing. Then the sink smeared propagator $D_S^{-1}(x_f|\mathcal{G}_S)$ is

$$D_S^{-1}(x_f|\mathcal{G}_S)^{ba}_{\beta\alpha} = \sum_{\vec{z}_1} S^\dagger(\vec{x_f}, \vec{z}_1)^{b,c_1}_{\beta,\gamma_1} D^{-1}(\{\vec{z}_1, t_f\}|\mathcal{G}_S)^{c_1,c_2}_{\gamma_1\gamma_2}, \tag{3.4.14}$$

which completes the source smearing of $\mathcal{G}$ at time position 0 and sink smearing at position x_f. The sink smearing of each eigenvector $v_i^\dagger(x_f)$ at the sink time can be

done before the construction of three-point functions as

$$v^{\dagger}_{S,i}(x_f)^{a}_{\alpha} = \sum_{\vec{z}_1} S^{\dagger}(\vec{x_f}, \vec{z}_1)^{a,c_1}_{\alpha,\gamma_1} v_i^{\dagger}(\{\vec{z}_1, t_f\})^{c_1}_{\gamma_1} \tag{3.4.15}$$

and these smeared eigenvectors can be reused for different valence masses and operators. From the sink-smearing noise vector $\eta^{\dagger}(x_f)$, which is used as the source of propagator $D^{-1}_{H,noi}(z, \eta_j)$, we can construct a structure similar to the propagator as

$$S_{\eta}(x_f)^{a,a'}_{\alpha,\alpha'} \equiv \eta^{\dagger}(x_f)\delta_{a,a'}\delta_{\alpha,\alpha'} \tag{3.4.16}$$

with a and a' the color indices, and α and α' the Dirac indices. $S(x_f)$ is diagonal in the color and Dirac indices. Then we can implement the smearing at position x_f for $S_{\eta}(x_f)$ as

$$S_{S,\eta(x_f)}{}^{ba}_{\beta\alpha} = \sum_{\vec{z}_1} S^{\dagger}(\vec{x_f}, \vec{z}_1)^{b,c_1}_{\beta,\gamma_1} S_{\eta}(\{\vec{z}_1, t_f\})^{c_1,c_2}_{\gamma_1\gamma_2}. \tag{3.4.17}$$

Nucleon three-point functions

Such a FFT contraction method can also be applied to the CI part of nucleon three-point functions

$$C_{3\mathrm{pt}}(\Gamma_\nu, \mu, \tau, t_f, \vec{p}_i, \vec{p}_f) = \sum_{\vec{x}_f, \vec{z}} e^{-i\vec{p}_f\cdot\vec{x}_f} e^{i\vec{q}\cdot\vec{z}} \mathrm{Tr}\left[\Gamma_\nu \left\langle \mathcal{O}_N(x_f)\right\rangle V_\mu(z)\bar{\mathcal{O}}_N(0)\right] \tag{3.4.18}$$

which shares the same variables as in Eq. (3.4.3) and Eq. (3.1.20). Γ_ν is the parity projection operator with $\Gamma_0 \equiv \frac{1}{2}(1+\gamma_0)$ and $\Gamma_i = \Gamma_0 i\gamma_5\gamma_i$, and V_μ is the local vector current

$$V_\mu = \sum_f e_f V^f_\mu = \sum_f e_f \bar{q}_f \gamma_\mu q_f, \tag{3.4.19}$$

in which q_f is the quark field of flavor f and e_f is the associated charge. In order to evaluate Eq. (3.4.18) on the lattice, we start from rewriting two-point functions in Eq. (3.1.19) in momentum space with projection of Γ_ν as

$$\begin{aligned}
C_{2\mathrm{pt}}(\mu, \vec{p}) &= \sum_y e^{-i\vec{p}\cdot\vec{y}} \left\langle \mathrm{Tr}\left[\Gamma_\nu \mathcal{O}_N(y)_\gamma \bar{\mathcal{O}}_N(0)_{\gamma'}\right]\right\rangle \\
&= \sum_y e^{-i\vec{p}\cdot\vec{y}} \epsilon_{abc}\epsilon_{a'b'c'} \Big(\mathrm{Tr}\left[\underline{D_d^{-1}(y|0)^{b'b}} D_u^{-1}(y|0)^{a'a}\right] \mathrm{Tr}\left[\Gamma_\nu D_u^{-1}(y|0)^{c'c}\right] \\
&\qquad + \mathrm{Tr}\left[\Gamma_\nu D_u^{-1}(y|0)^{c'c} \underline{D_d^{-1}(y|0)^{b'b}} D_u^{-1}(y|0)^{a'a}\right] \Big) \\
&= \sum_y e^{-i\vec{p}\cdot\vec{y}} \epsilon_{abc}\epsilon_{a'b'c'} \Big(\mathrm{Tr}\left[D_d^{-1}(y|0)^{b'b} \underline{D_u^{-1}(y|0)^{a'a}}\right] \mathrm{Tr}\left[\Gamma_\nu D_u^{-1}(y|0)^{c'c}\right] \\
&\qquad + \mathrm{Tr}\left[\underline{D_u^{-1}(y|0)^{a'a}} \Gamma_\nu D_u^{-1}(y|0)^{c'c} D_d^{-1}(y|0)^{b'b}\right] \Big).
\end{aligned} \tag{3.4.20}$$

We can try to single our down quark propagator $D_d^{-1}(y|0)$ as

$$\begin{aligned} C_{\rm 2pt}(\mu,\vec{p}) &= \sum_y e^{-i\vec{p}\cdot\vec{y}}(M_\nu^d)^{bb'}_{\beta\beta'}(y|0)D_d^{-1}(y|0)^{b'b}_{\beta'\beta} \\ &= \sum_y e^{-i\vec{p}\cdot\vec{y}}{\rm Tr}\left[M_\nu^d(y|0)D_d^{-1}(y|0)\right], \end{aligned} \tag{3.4.21}$$

with M^d being

$$\begin{aligned} (M_\nu^d)^{bb'}_{\beta\beta'}(y|x) = \epsilon_{abc}\epsilon_{a'b'c'}\Big(&\left[\underline{D_u^{-1}(y|x)^{a'a}}\right]_{\beta\beta'}{\rm Tr}\left[\Gamma_\nu D_u^{-1}(y|x)^{c'c}\right] \\ &+ {\rm Tr}\left[\underline{D_u^{-1}(y|0)^{a'a}\Gamma_\nu D_u^{-1}(y|x)^{c'c}}\right]_{\beta\beta'}\Big), \end{aligned} \tag{3.4.22}$$

in which we have exchanged color index b and b' to have a consistent trace Tr over color and spin in Eq. (3.4.21). Similarly, we can single out up quark propagator $D_u^{-1}(y|0)$ as

$$\begin{aligned} C_{\rm 2pt}(\mu,\vec{p}) &= \sum_y e^{-i\vec{p}\cdot\vec{y}}{\rm Tr}\left[M^u_{1,\nu}(y|0)D_u^{-1}(y|0) + M^u_{2,\nu}(y|0)D_u^{-1}(y|0)\right] \\ &= \sum_y e^{-i\vec{p}\cdot\vec{y}}{\rm Tr}\left[M^u_{3,\nu}(y|0)D_u^{-1}(y|0) + M^u_{4,\nu}(y|0)D_u^{-1}(y|0)\right], \end{aligned} \tag{3.4.23}$$

with $M^u_{1,\nu}$, $M^u_{2,\nu}$, $M^u_{3,\nu}$ and $M^u_{4,\nu}$ defined as

$$\begin{aligned} (M^u_{1,\nu})^{aa'}_{\alpha\alpha'}(y|x) &= \epsilon_{abc}\epsilon_{a'b'c'}\left[\underline{D_d^{-1}(y|0)^{b'b}}\right]_{\alpha\alpha'}{\rm Tr}\left[\Gamma_\nu D_u^{-1}(y|0)^{c'c}\right], \\ (M^u_{2,\nu})^{aa'}_{\alpha\alpha'}(y|x) &= \epsilon_{abc}\epsilon_{a'b'c'}\left[\Gamma_\nu D_u^{-1}(y|0)^{c'c}\underline{D_d^{-1}(y|0)^{b'b}}\right]_{\alpha\alpha'}, \\ (M^u_{3,\nu})^{cc'}_{\alpha\alpha'}(y|x) &= \epsilon_{abc}\epsilon_{a'b'c'}{\rm Tr}\left[\underline{D_d^{-1}(y|0)^{b'b}}D_u^{-1}(y|0)^{a'a}\right][\Gamma_\nu]_{\alpha\alpha'}, \\ (M^u_{4,\nu})^{cc'}_{\alpha\alpha'}(y|x) &= \epsilon_{abc}\epsilon_{a'b'c'}\left[\underline{D_d^{-1}(y|0)^{b'b}}D_u^{-1}(y|0)^{a'a}\Gamma_\nu\right]_{\alpha\alpha'}, \end{aligned}$$

Then the evaluation of the CI part of Eq. (3.4.18) for the down quark part is

$$\begin{aligned} C^d_{\rm CI,3pt}(\Gamma_\nu,\mu,\tau,t_f,\vec{p}_i,\vec{p}_f) &= \sum_{\vec{x}_f,\vec{z}} e^{-i\vec{p}_f\cdot\vec{x}_f}e^{i\vec{q}\cdot\vec{z}}{\rm Tr}\left[\Gamma_\nu\left\langle\mathcal{O}_N(x_f)\right\rangle V_\mu^d(z)\bar{\mathcal{O}}_N(0)\right] \\ &= e_d\sum_{\vec{x}_f,\vec{z}} e^{-i\vec{p}_f\cdot\vec{x}_f}e^{i\vec{q}\cdot\vec{z}}{\rm Tr}\left[M_\nu^d(x_f|0)D_d^{-1}(x_f|z)\gamma_\mu D_d^{-1}(z|0)\right]. \end{aligned} \tag{3.4.24}$$

We can also write the CI part of the up quark contribution $C^u_{\rm CI,3pt}$ as

$$\begin{aligned} C^u_{\rm CI,3pt}(\Gamma_\nu,\mu,\tau,t_f,\vec{p}_i,\vec{p}_f) = e_u\sum_{\vec{x}_f,\vec{z}} &e^{-i\vec{p}_f\cdot\vec{x}_f}e^{i\vec{q}\cdot\vec{z}}\times \\ &{\rm Tr}\left[M_\nu^u(x_f|0)D_u^{-1}(x_f|z)\gamma_\mu D_u^{-1}(z|0)\right], \end{aligned} \tag{3.4.25}$$

in which we have defined M^u_ν to be

$$M^u_\nu = M^u_{1,\nu} + M^u_{2,\nu} + M^u_{3,\nu} + M^u_{4,\nu}. \tag{3.4.26}$$

With Eq. (3.4.7) we are able to evaluate $D^{-1}(x_f|z)$, and also we can implement FFT contractions similar to Eq. (3.4.8) and Eq. (3.4.9) to get $C^{u/d}_{\mathrm{CI,3pt}}(\Gamma_\nu, \mu, \tau, t_f, \vec{p}_i, \vec{p}_f)$ as

$$\begin{aligned} C^{u/d}_{\mathrm{CI,3pt}} =& \langle \sum_{\lambda_i \leq \lambda_c} \mathrm{Tr}[\frac{1}{\lambda_i + m} G^L_i(\mu, \vec{q}, \tau) F^{L,u/d}_i(\nu, \vec{p}_f, t_f)] \\ &+ \sum_{j=1}^{n_f} \frac{1}{n_f} \mathrm{Tr}[G^H_j(\mu, \vec{q}, \tau)(F^{H,u/d}_j(\nu, \vec{p}_f, t_f)]\rangle, \end{aligned} \tag{3.4.27}$$

where

$$\begin{aligned} G^L_i(\mu, \vec{q}, \tau) &= \sum_{\vec{z}} e^{i\vec{q}\cdot\vec{z}} v^\dagger_i(z) \gamma_\mu D^{-1}(z|0), \\ F^{L,u/d}_i(\nu, \vec{p}_f, t_f) &= \sum_{\vec{x}_f} e^{-i\vec{p}_f\cdot\vec{x}_f} M^{u/d}_\nu(x_f|0) v_i(x_f), \\ G^H_j(\mu, \vec{q}, \tau) &= \sum_{\vec{z}} e^{i\vec{q}\cdot\vec{z}} \gamma_5 (D^{-1}_{H,noi}(z, \eta_j))^\dagger \gamma_5 \gamma_\mu D^{-1}(z|0), \\ F^{H,u/d}_j(\nu, \vec{p}_f, t_f) &= \sum_{\vec{x}_f} e^{-i\vec{p}_f\cdot\vec{x}_f} M^{u/d}_\nu(x_f|0) \eta(x_f), \end{aligned} \tag{3.4.28}$$

in which we have defined $D^{-1}(z|0) = D^{-1}_u(z|0) = D^{-1}_d(z|0)$ to be the light quark propagator, and used $D^{-1}(x_f|z) = \gamma_5 (D^{-1}(z|x_f))^\dagger \gamma_5$ for the high-mode propagator $D^{-1}_{H,noi}(z, \eta_j)$. In the same way as was done for the pion, we can also implement source and sink smearing for the nucleon with the method described in Sec. 3.4. It is also straightforward to implement LMS as described in Sec. (3.3). Comparing the contractions in Eq. (3.4.20) and contractions with LMS in Eq. (3.3.43), LMS of the source simply says to replace propagator in Eq. (3.4.20)

$$D^{-1} \to \eta_i P^L_{\vec{w}_i} + P^H_{S_{grid}} \tag{3.4.29}$$

with the propagator from grid position $\vec{w}_i$ and repeat the calculation of the three-point function for all grid points. Also we need make the replacement

$$D^{-1} \to P^H_{S_{grid}} \tag{3.4.30}$$

for the pure high mode part $G^{(H,H,H)}(p)$ in Eq. (3.3.43) and repeat the calculation of the three-point function. This summarizes the contractions of the CI part of the nucleon three-point functions which leads to gains similar to those in the pion case.

Chapter 4 Pion form factor

4.1 Introduction

The electric form factor $f_{\pi\pi}(Q^2)$, $Q^2 \equiv -(p'-p)^2 \geq 0$, is defined from the pionic matrix element and its slope at $Q^2 = 0$ gives the mean square charge radius

$$\langle \pi^i(p')|V_\mu^j(0)|\pi^k(p)\rangle = i\epsilon^{ijk}(p_\mu + p'_\mu)f_{\pi\pi}(Q^2), \tag{4.1.1}$$

$$\langle r_\pi^2\rangle \equiv -6\frac{df_{\pi\pi}(Q^2)}{dQ^2}|_{Q^2=0}, \tag{4.1.2}$$

where $V_\mu^j = \bar{\psi}\frac{1}{2}\tau^j\gamma_\mu\psi$ is the isovector vector current, τ^i are the Pauli matrices in flavor space, and $|\pi^i\rangle$ are the pion triplet states. $\langle r_\pi^2\rangle$ has been determined precisely based on the existing πe scattering data [44, 3, 45] and $e^+e^- \to \pi^+\pi^-$ data [46, 47] averaged by the Particle Data Group (PDG) [18] as $\langle r_\pi^2\rangle = 0.434(5)$ fm^2. Phenomenologically, $f_{\pi\pi}(Q^2)$ is fitted quite well over the range $0 < Q^2/m_\rho^2 < 0.4$ with the single monopole form $(1 + Q^2/\Lambda^2)^{-1}$, with $\Lambda \sim m_\rho$. This gives credence to the idea of vector dominance [48, 49]. In chiral perturbation theory, $\langle r_\pi^2\rangle$ has been calculated with $SU(2)$ Chiral Perturbation Theory [50] at NNLO and also at NLO with $SU(3)$ formula [51], which entails the uncertainties of the low energy constants.

Since lattice QCD is an *ab initio* calculation and the experimental determination of $\langle r_\pi^2\rangle$ from the πe scattering is very precise, it provides a stringent test for lattice QCD calculations to demonstrate complete control over the statistical and systematic errors in estimates of the relevant pionic matrix element. Over the years, the pion form factor has been calculated with quenched approximation [52, 41], and for the $N_\mathrm{f} = 2$ [9, 10, 11, 12, 13], $N_\mathrm{f} = 2+1$ [53, 54, 55, 14, 15, 16] and $N_\mathrm{f} = 2+1+1$ [17] cases.

In this section, we use valence overlap fermions to calculate the pion form factor on six ensembles of domain-wall fermion configurations with different sea pion masses, including two at the physical pion mass, four lattice spacings and different volumes to control the systematic errors. Due to the multi-mass algorithm available for overlap fermions, we can effectively calculate several valence quark masses on each ensemble [29, 56, 57, 58] and also $\mathcal{O}(100)$ combinations of the initial and final pion momenta with little overhead with the usage of the fast Fourier transform (FFT) algorithm [59] in the three-point function contraction. This allows us to study both the sea and the valence quark mass dependence of $\langle r_\pi^2\rangle$ in terms of partially quenched chiral perturbation theory, besides giving an accurate result at the physical pion mass.

4.2 Numerical details

We use overlap fermions on six ensembles of HYP smeared 2+1-flavor domain-wall fermion configurations with Iwasaki gauge action (labeled with I) [60, 61] and Iwasaki plus the Dislocation Suppressing Determinant Ratio (DSDR) gauge action (labeled

Table 4.1: The ensembles and their respective lattice size $L^3 \times T$, lattice spacing a, pion mass m_π and number of configurations n_{cfg}.

Lattice	$L^3 \times T$	a (fm)	La (fm)	m_π(MeV)	$m_\pi L$	n_{cfg}
24IDc	$24^3 \times 64$	0.195	4.66	141	3.33	231
32ID	$32^3 \times 64$	0.143	4.58	172	3.99	199
32IDh	$32^3 \times 64$	0.143	4.58	250	5.80	100
48I	$48^3 \times 96$	0.114	5.48	139	3.86	81
24I	$24^3 \times 64$	0.111	2.65	340	4.56	202
32I	$32^3 \times 64$	0.083	2.65	302	4.05	309

with ID) [62] as listed in Table 4.1. The effective quark propagator of the massive overlap fermions is the inverse of the operator $(D_c + m)$ [25, 28], where D_c is chiral, i.e., $\{D_c, \gamma_5\} = 0$ [26]. And it can be expressed in terms of the overlap Dirac operator D_{ov} as $D_c = \rho D_{ov}/(1 - D_{ov}/2)$, with $\rho = -(1/(2\kappa) - 4)$ and $\kappa = 0.2$. A multi-mass inverter is used to calculate the propagators with 2 to 6 valence pion masses varying from the unitary point to ~ 390 MeV. On 24I, 32I and 24IDc (c stands for the coarse lattice spacing), Gaussian smearing [63] is applied with root mean square (RMS) radius 0.49 fm, 0.49 fm and 0.53 fm, respectively, for both source and sink. On 48I, 32ID and 32IDh (h for heavier pion mass), box-smearing [64, 65] with box half size 0.57 fm, 1.0 fm and 1.0 fm, respectively, is applied as an economical substitute for Gaussian smearing.

To extract pionic matrix elements, the three-point function (3pt) $C_{3\text{pt}}(\tau, t_{\text{f}}, \vec{p}_{\text{i}}, \vec{p}_{\text{f}})$ is computed

$$C_{3\text{pt}} = \sum_{\vec{x}_{\text{f}}, \vec{z}} e^{-i\vec{p}_{\text{f}} \cdot \vec{x}_{\text{f}}} e^{i\vec{q} \cdot \vec{z}} \langle \text{T}[\chi_{\pi^+}(x_{\text{f}}) V_4^3(z) \chi_{\pi^+}^\dagger(\mathcal{G})] \rangle \tag{4.2.1}$$

where $\chi_{\pi^+}(\vec{x}, t) = \bar{d}(\vec{x}, t)\gamma_5 u(\vec{x}, t)$ is the interpolating field of the pion with u and d the up and down quark spinors, $S(y|x)$ is the quark propagator from x to y, $z \equiv \{\tau, \vec{z}\}$, $x_{\text{f}} \equiv \{t_{\text{f}}, \vec{x}_{\text{f}}\}$, $\vec{p}_{\text{i}}$ and $\vec{p}_{\text{f}}$ is the initial and final momentum of the pion, respectively, $\vec{q} = \vec{p}_{\text{f}} - \vec{p}_{\text{i}}$ is the momentum transfer, and $\mathcal{G}$ is the smeared Z_3-noise grid source [39]. The disconnected insertions in Eq.(4.2.1) vanish in the ensemble average [41]. The connected insertions of $C_{3\text{pt}}(\tau, t_{\text{f}}, \vec{p}_{\text{i}}, \vec{p}_{\text{f}})$ are computed with the method described in Sec. 3.4 using FFT.

4.3 Analysis and results

The source-sink separations t_{f} used in this work with different ensembles are collected in Table 4.2. The largest t_{f} is ~ 2.0 fm on the coarsest lattice 24IDc and the smallest one is ~ 0.7 fm on the finest lattice 32I. There are two momentum setups used in this work: the special $|\vec{p}_{\text{i}}| = |\vec{p}_{\text{f}}|$ case and the general $|\vec{p}_{\text{i}}| \neq |\vec{p}_{\text{f}}|$ one. We will talk about the fit procedures in this section.

Table 4.2: The lattice setup of this calculation. The $n_{\rm i}$ sets of smeared noise-grid sources with $\{n_s, n_s, n_s, n_t\}$ points in $\{x, y, z, t\}$ directions, respectively, are placed on the lattice to improve the statistics, and $n_{\rm f}$ sets of $S^H_{\rm noi}$ at $2n_t$ sink time slices at $i\frac{T}{n_t}t_{\rm f}$ and $T - i\frac{T}{n_t}t_{\rm f}$ with $i = \{1 \cdots n_t\}$. On a given configuration, the total number of the propagators we generated is $n_{\rm i} + n_{\rm f}$ and $n_{\rm meas} = n_{\rm i} n_s^3 n_t$ which is the number of measurements of 3pt.

Lattice	$n_{\rm i}$	n_t	n_s	$t_{\rm f}/a$	$n_{\rm f}$	$n_{meas} n_{cfg}$
24IDc	4	2	3	$6, 7, 8, 9, 10$	$4, 4, 6, 4, 4$	49896
32ID	6	2	2	$9, 10, 11$	$4, 5, 12$	19104
32IDh	6	2	2	$9, 10, 11$	$4, 5, 12$	9600
48I	5	3	4	$8, 10, 12$	$4, 8, 12$	77760
24I	8	1	2	$10, 11, 12$	$3, 5, 5$	12928
32I	8	1	2	$8, 12, 15$	$4, 8, 12$	19776

Three-point functions fitting

With the usage of Wick contractions and gauge invariance, the three-point function (3pt) with two sources, one at each of the time slices 0 and $T/2$, has contributions from the three diagrams shown in Fig. 4.1. (We assume $T/2 > t_{\rm f} > \tau > 0$.) The diagram 4.1.(1) contributes

$$\begin{aligned} C_{\rm 3pt,(1)}(\tau, t_{\rm f}, \vec{p}_{\rm i}, \vec{p}_{\rm f}) = & \frac{Z_{\vec{p}_{\rm i}} Z_{\vec{p}_{\rm f}} (E_{\rm i} + E_{\rm f})}{E_{\rm i} E_{\rm f} Z_V} f_{\pi\pi}(Q^2)(e^{-E_{\rm i}\tau - E_{\rm f}(t_{\rm f}-\tau)}) \\ & + C_1 e^{-E_{\rm i}\tau - E^1_{\rm f}(t_{\rm f}-\tau)} + C_2 e^{-E^1_{\rm i}\tau - E_{\rm f}(t_{\rm f}-\tau)} + C_3 e^{-E^1_{\rm i}\tau - E^1_{\rm f}(t_{\rm f}-\tau)}, \end{aligned} \tag{4.3.1}$$

where $Z_{\vec{p}}$ is the spectral weight and E and E^1 is the ground state and first-excited state energy, respectively. $Z_{\vec{p}_{\rm i}}, Z_{\vec{p}_{\rm f}}$, $E_{\rm i}$, $E_{\rm f}$, $E^1_{\rm i}$ and $E^1_{\rm f}$ are constrained by the joint fit with the corresponding two-point function (2pt). Z_V is the finite normalization constant for the local vector current which is determined from the forward matrix element as $Z_V \equiv \frac{2E}{\langle \pi(p)|V_4|\pi(p)\rangle}$. C_1, C_2 and C_3 are free parameters for the excited-state contaminations. The diagram 4.1.(2) contributes

$$C_{\rm 3pt,(2)}(\tau, t_{\rm f}, \vec{p}_{\rm i}, \vec{p}_{\rm f}) = \frac{Z_{\vec{p}_{\rm i}} Z_{\vec{p}_{\rm f}} (E_{\rm i} + E_{\rm f})}{E_{\rm i} E_{\rm f} Z_V} f_{\pi\pi}(Q^2)(e^{-E_{\rm i}(T/2+\tau) - E_{\rm f}(t_{\rm f}-\tau)}), \tag{4.3.2}$$

in which we have ignored the excited-state contaminations from the source at $T/2$ since such terms are suppressed by $e^{-E^1_i T/2}$ which is of order $\sim 10^{-8}$ with $E^1_i \approx$ 1.3 GeV estimated with the experimental value of the first excited-state of the pion. Since we have put two sources at $t = 0$ and $t = T/2$ for most ensembles to increase statistics, we need a term with C_4 and $E_{\rm h}$ to account for the case that the current insertion is outside of the time window between the source and the sink. This is shown in the diagram 4.1.(3) and contributes as

$$C_{\rm 3pt,(3)}(\tau, t_{\rm f}, \vec{p}_{\rm i}, \vec{p}_{\rm f}) = C_4 e^{-E_{\rm i}(T/2 - t_{\rm f}) - E_{\rm h}(t_{\rm f}-\tau)}, \tag{4.3.3}$$

in which this term corresponds to the creation of a hadron state with operator $V_4 = \bar{q}\gamma_4 q$ at time slice τ with momentum q as $\langle h(q)|\, V_4\, |0\rangle$, an annihilation of a pion

state at time slice $T/2$ with momentum $p_{\rm i}$ as $\langle 0|\,\chi^{\dagger}_{\pi^+}\,|\pi^-(p_{\rm i})\rangle$ and an unknown matrix element $\langle \pi^-(p_{\rm i})|\,\chi_{\pi^+}\,|h(q)\rangle$. The excited-state contaminations from E^1_i are ignored for the same reason as in the previous discussion and the excited-state contaminations from E^1_h are ignored under current statistics.

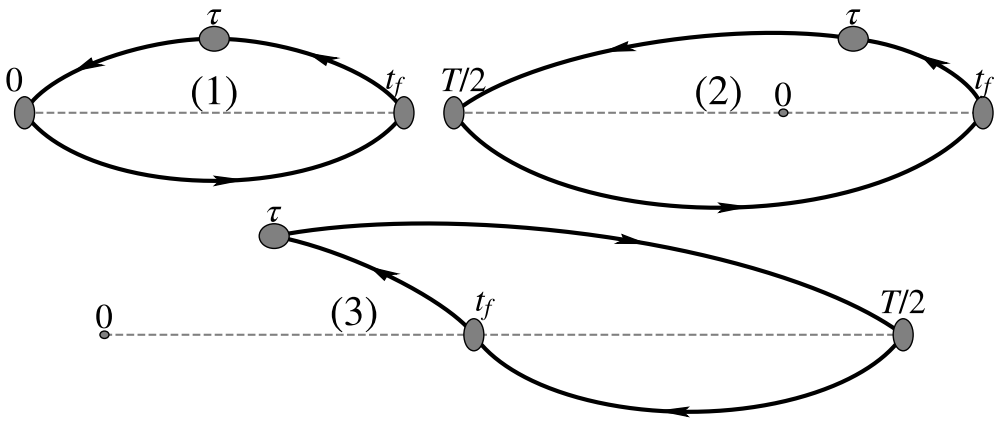

Figure 4.1: Diagrams of pion three-point functions with sources at time slices 0 and $T/2$.

In order to test the functional form of $C_{\rm 3pt,(3)}(\tau, t_{\rm f}, \vec{p}_{\rm i}, \vec{p}_{\rm f})$, we construct 3pt with one source at time slice $T/2 = 32$ and sink time $t_{\rm f}$ at $20, 21, 22$ with $\vec{p}_{\rm i} = \{0,0,0\}$ and $\vec{p}_{\rm f} = \{0,0,\frac{2\pi}{L}\}$. Then we can evaluate the effective mass $E^{\rm eff}_{\rm h}$ and $E^{\rm eff}_{\rm i}$ from $C_{\rm 3pt,(3)}(\tau, t_{\rm f}, \vec{p}_{\rm i}, \vec{p}_{\rm f})$ with

$$\begin{aligned} E^{\rm eff}_{\rm h}(\tau, t_{\rm f}) &= \ln\left(\frac{C_{\rm 3pt,(3)}(\tau+1, t_{\rm f}, \vec{p}_{\rm i}, \vec{p}_{\rm f})}{C_{\rm 3pt,(3)}(\tau, t_{\rm f}, \vec{p}_{\rm i}, \vec{p}_{\rm f})}\right), \\ E^{\rm eff}_{\rm i}(\tau, t_{\rm f}) &= \ln\left(\frac{C_{\rm 3pt,(3)}(\tau+1, t_{\rm f}, \vec{p}_{\rm i}, \vec{p}_{\rm f})}{C_{\rm 3pt,(3)}(\tau, t_{\rm f}-1, \vec{p}_{\rm i}, \vec{p}_{\rm f})}\right), \end{aligned} \tag{4.3.4}$$

in which $E^{eff}_{\rm i}$ is evaluated by a simultaneous change of τ and $t_{\rm f}$ to single out $E_{\rm i}$ from the exponential $e^{-E_{\rm i}(T/2-t_{\rm f})-E_{\rm h}(t_{\rm f}-\tau)}$. And they should equal to $E_h = \sqrt{m_h^2 + (\vec{p}_{\rm f}-\vec{p}_{\rm i})^2}$ and $E_\pi = \sqrt{m_\pi^2 + \vec{p}_{\rm i}^{\,2}} = m_\pi$ in the $t_{\rm f} \gg \tau$ limit, as confirmed in Fig. 4.2 and the fit results in Fig. 4.4.

Thus the final functional form is $C_{\rm 3pt} = C_{\rm 3pt,(1)} + C_{\rm 3pt,(2)} + C_{\rm 3pt,(3)}$ as

$$\begin{aligned} C_{\rm 3pt}(\tau, t_{\rm f}, \vec{p}_{\rm i}, \vec{p}_{\rm f}) &= \frac{Z_{\vec{p}_{\rm i}} Z_{\vec{p}_{\rm f}} (E_{\rm i}+E_{\rm f})}{E_{\rm i} E_{\rm f} Z_V} f_{\pi\pi}(Q^2) \times (e^{-E_{\rm i}\tau - E_{\rm f}(t_{\rm f}-\tau)} + e^{-E_{\rm i}(T/2+\tau) - E_{\rm f}(t_{\rm f}-\tau)}) \\ &+ C_1 e^{-E_{\rm i}\tau - E^1_{\rm f}(t_{\rm f}-\tau)} + C_2 e^{-E^1_{\rm i}\tau - E_{\rm f}(t_{\rm f}-\tau)} + C_3 e^{-E^1_{\rm i}\tau - E^1_{\rm f}(t_{\rm f}-\tau)} + C_4 e^{-E_{\rm i}(T/2-t_{\rm f}) - E_{\rm h}(t_{\rm f}-\tau)}. \end{aligned} \tag{4.3.5}$$

The associated 2pt is fitted with

$$\begin{aligned} C_{\rm 2pt}(t, \vec{p}) = \frac{Z^2_{\vec{p}}}{E}(e^{-Et} + e^{-E(T-t)} + e^{-E(T/2-t)} + e^{-E(T/2+t)}) \\ + A_1(e^{-E^1 t} + e^{-E^1(T/2-t)}), \end{aligned} \tag{4.3.6}$$

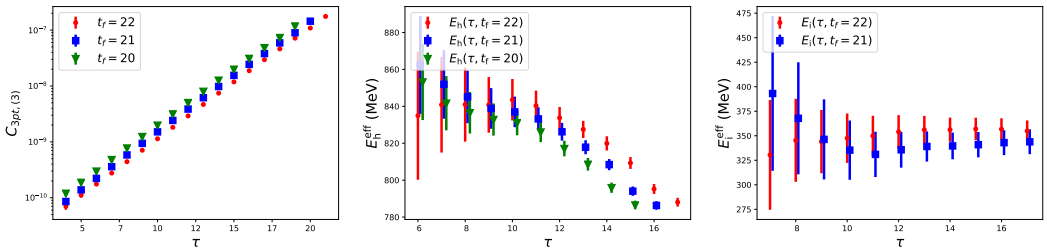

Figure 4.2: The plot on the left is of $C_{3\mathrm{pt},(3)}$ on 24I with $m_\pi = 347$ MeV, one source at time slice $T/2$, $\vec{p}_\mathrm{i} = \{0,0,0\}$ and $\vec{p}_\mathrm{f} = \{0,0,\frac{2\pi}{L}\}$. The correlation function is a rising exponential which confirms that $E_h > 0$ in Eq. (4.3.3). The plots in the middle and right panels show the corresponding effective masses $E_\mathrm{h}^\mathrm{eff}$ and $E_\mathrm{i}^\mathrm{eff}$ obtained with Eq. (4.3.4), respectively.

with A_1 being a free parameter for the excited-state contributions and the exponential terms with $T/2$ account for contributions from the source at $T/2$. An example of fitted energies is shown in Fig. 4.3. It can be seen that the first excited-state energy E^1 is close to the experimental value 1.3 GeV and it has been used to constrain the one in 3pt by the joint fit of 2pt and 3pt to extract $f_{\pi\pi}(Q^2)$.

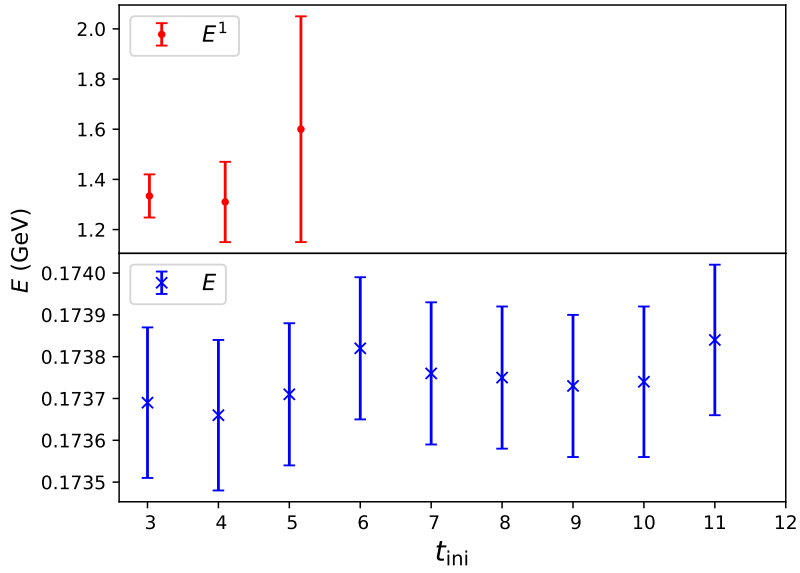

Figure 4.3: Pion energies as a function of t_ini with $[t_\mathrm{ini}, 15]$ the fit-range of the 2pt on 32ID with pion mass 173.7 MeV at zero momentum. The contributions from the first excited state are ignored for $t_\mathrm{ini} \geq 6$ under current statistics.

In order to test the fitting function of 3pt in Eq. (4.3.5), a comparison of the fitting of the one-source result with the source at $t = 0$ and that of the two-source result with sources at $t = 0$ and 32 in the same inversion is shown in Fig. 4.4. For

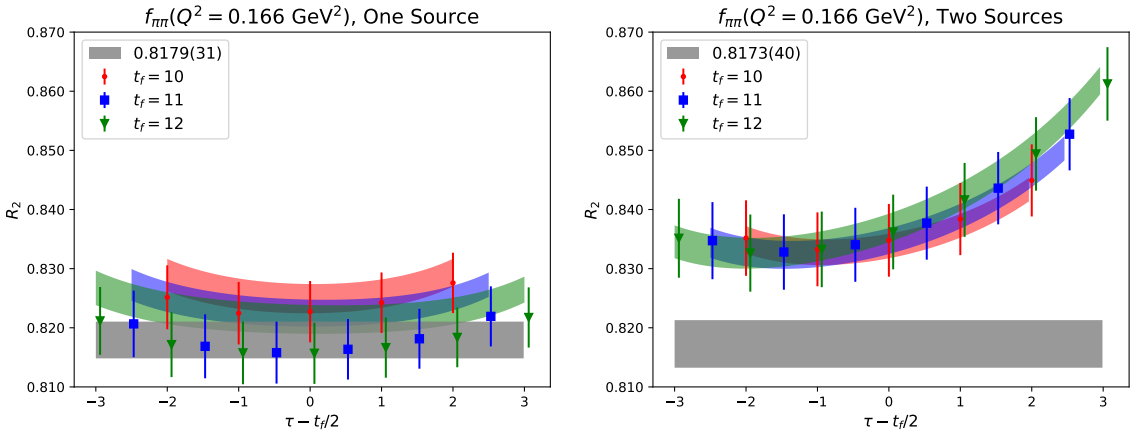

Figure 4.4: Joint fitting results on 24I with $m_\pi = 347$ MeV, $\vec{p}_\mathrm{i} = \{0,0,0\}$ and $\vec{p}_\mathrm{f} = \{0,0,\frac{2\pi}{L}\}$. The plot on the left corresponds to the case of one source at time slice 0. The gray band is for the fitted value of the ground state form factor $f_{\pi\pi}(Q^2)$ which is close to the data points due to small excited-state contaminations. The plot on the right corresponds to the case of a source at each of the time slices 0 and $T/2$. The gray band is far away from the rising data points due to the additional C_4 term with fitted $E_\mathrm{h} = 807(82)$ MeV which is consistent with the result of Fig. 4.2.

illustrative purpose, the data points are shown with ratio R_2,

$$\begin{aligned} R_2(\tau, t_\mathrm{f}, \vec{p}_\mathrm{i}, \vec{p}_\mathrm{f}) &= \frac{C_{3\mathrm{pt}}(\tau, t_\mathrm{f}, \vec{p}_\mathrm{i}, \vec{p}_\mathrm{f})}{\frac{Z_{\vec{p}_\mathrm{i}} Z_{\vec{p}_\mathrm{f}} (E_\mathrm{i}+E_\mathrm{f})}{4E_\mathrm{i}E_\mathrm{f}Z_V}(e^{-E_\mathrm{i}\tau - E_\mathrm{f}(t_\mathrm{f}-\tau)} + e^{-E_\mathrm{i}(T/2+\tau) - E_\mathrm{f}(t_\mathrm{f}-\tau)})} \\ &= f_{\pi\pi}(Q^2) + \text{excited-state terms} + C_4 \text{ term}, \end{aligned} \tag{4.3.7}$$

in which $Z_{\vec{p}}$ and E are determined from the fitting of 2pt and Z_V from 3pt at zero momentum transfer. It can be seen that the two results agree with each other within uncertainty which again confirms our fitting formula.

Thus for the general momentum setup $|\vec{p}_\mathrm{i}| \neq |\vec{p}_\mathrm{f}|$ we can proceed further to fit $C_{3\mathrm{pt}}(\tau, t_\mathrm{f}, \vec{p}_\mathrm{i}, \vec{p}_\mathrm{f})$ together with $C_{3\mathrm{pt}}(\tau, t_\mathrm{f}, \vec{p}_\mathrm{f}, \vec{p}_\mathrm{i})$ which corresponds to the exchange of initial and final momentum. Fig. 4.5 shows example plots on 24IDc and 32ID. The data points are fitted well with Eq. (4.3.5) and the fit results are shown in bands with $\chi^2/d.o.f. \sim 1$. The data points for $C_{3\mathrm{pt}}(\tau, t_\mathrm{f}, \vec{p}, \vec{0})$ are lower and closer to the gray band since the C_4 term has a negative contribution with a suppression factor $e^{-E(\vec{p})T/2}$ compared to the case of $C_{3\mathrm{pt}}(\tau, t_\mathrm{f}, \vec{0}, \vec{p})$ in which the C_4 term has a positive and large contribution with only a suppression factor $e^{-E(\vec{0})T/2}$.

For the special $|\vec{p}_\mathrm{i}| = |\vec{p}_\mathrm{f}|$ case, one can simply calculate the ratio of 3pts, and obtain the pion form factor by the following parametrization of the ratio R_1,

$$\begin{aligned} R_1(\tau, t_\mathrm{f}, \vec{p}_\mathrm{i}, \vec{p}_\mathrm{f}) &= C_{3\mathrm{pt}}(\tau, t_\mathrm{f}, \vec{p}_\mathrm{i}, \vec{p}_\mathrm{f}) / C_{3\mathrm{pt}}(\tau, t_\mathrm{f}, \vec{p}_\mathrm{i}, \vec{p}_\mathrm{i}) \\ &= f_{\pi\pi}(Q^2) + B_1(e^{-\Delta E \tau} + e^{-\Delta E(t_\mathrm{f}-\tau)}) + B_2 e^{-\Delta E t_\mathrm{f}}, \end{aligned} \tag{4.3.8}$$

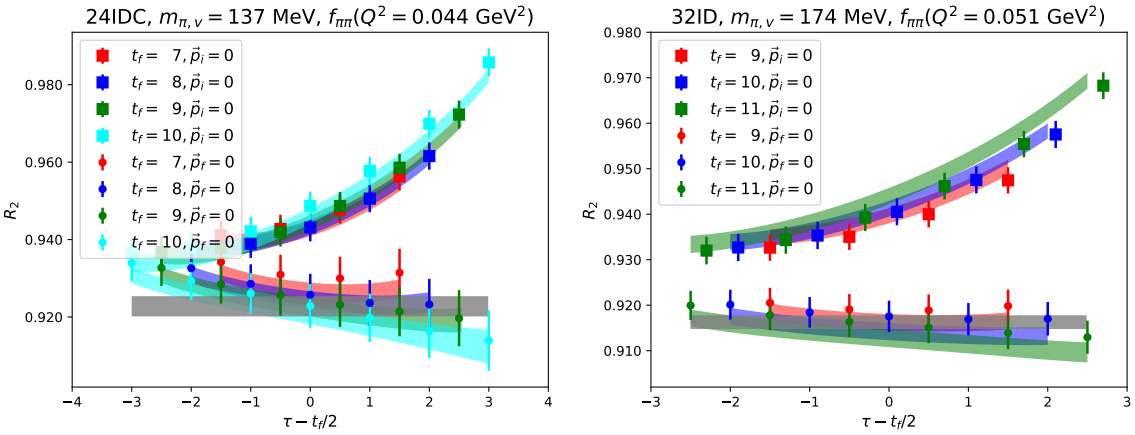

Figure 4.5: Examples of the ratios on 24IDc and 32ID with various values of source-sink separation t_f and current position τ. The plots show the general $|\vec{p}_\mathrm{i}| \neq |\vec{p}_\mathrm{f}|$ case with square points $\vec{p}_\mathrm{i} = -\vec{q}, \vec{p}_\mathrm{f} = 0$ and dot points $p_\mathrm{i} = 0, \vec{p}_\mathrm{f} = \vec{q}$. The data points agree well with the bands predicted from the fit, and the gray band is for the ground state form factor $f_{\pi\pi}(Q^2)$.

where the terms with B_1 and B_2 are the contributions from the excited-state contamination, and $\Delta E = E^1(\vec{p}_\mathrm{i}) - E(\vec{p}_\mathrm{i})$ is the energy difference between the pion energy $E(\vec{p}_\mathrm{i})$ and that of the first excited state $E^1(\vec{p}_\mathrm{i})$. These energies are also constrained by the joint fit with the corresponding 2pt. Since the excited-state contaminations of the forward matrix element in the denominator are known to be small and the contribution from C_4 term in Eq. (4.3.5) is suppressed by $e^{-E(\vec{p}_i)T/2}$ with $\vec{p}_i \neq \vec{0}$ for both the denominator and numerator, we have dropped them in the parametrization of the ratio and our fits can describe the data with $\chi^2/d.o.f. \sim 1$. Fig. 4.6 shows a sample plot for 32ID with the unitary pion mass of 174 MeV at $Q^2 = 0.146$ GeV^2. In view of the fact that the data points are symmetric about $\tau = t_\mathrm{f}/2$, within uncertainty, it reassures that the sink smearing implemented under the FFT contraction has the same overlap with the pion state as that of the source smearing.

z-Expansion fit and chiral extrapolation of pion radius

To obtain $f_{\pi\pi}(Q^2)$, we have done a model-independent z-expansion [66] fit using the following equation with $k_\mathrm{max} \geq 3$.

$$\begin{aligned} f_{\pi\pi}(Q^2) &= \sum_{k=0}^{k_\mathrm{max}} a_k z^k \\ z(t, t_\mathrm{cut}, t_0) &= \frac{\sqrt{t_\mathrm{cut} - t} - \sqrt{t_\mathrm{cut} - t_0}}{\sqrt{t_\mathrm{cut} - t} + \sqrt{t_\mathrm{cut} - t_0}}, \end{aligned} \tag{4.3.9}$$

where $t = -Q^2$, and $f_{\pi\pi}(0) = 1$ after normalization which leads to the constraint $a_0 = 1 - \sum_{k=1}^{k_\mathrm{max}} a_k z^k(t = 0, t_\mathrm{cut}, t_0)$; $t_\mathrm{cut} = 4m^2_{\pi,\mathrm{mix}}$ corresponds to the two-pion production

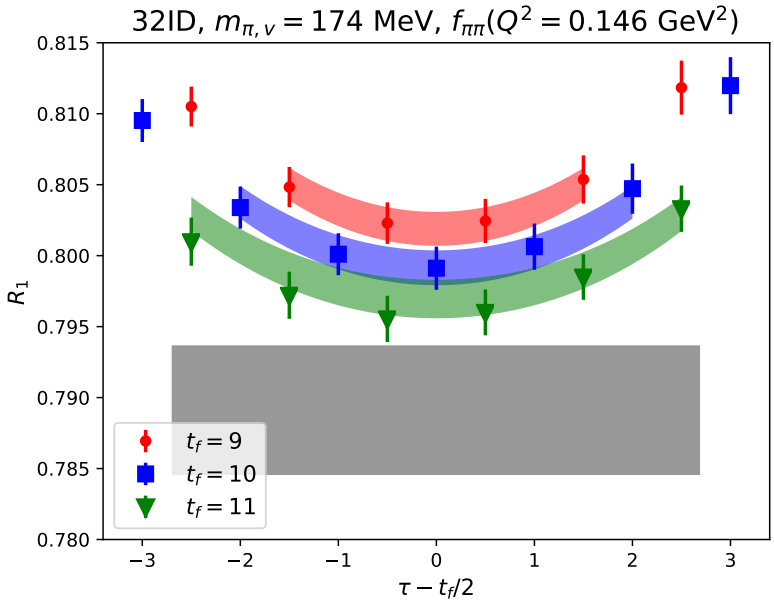

Figure 4.6: Example of the ratios for the special $|\vec{p}_\text{i}| = |\vec{p}_\text{f}|$ case on 32ID with various values of source-sink separation t_f and current position τ. The data points agree well with the bands predicted from the fit, and the gray band is for the fitted value of ground state form factor $f_{\pi\pi}(Q^2)$.

threshold with $m^2_{\pi,\text{mix}} = (m^2_{\pi,\text{v}} + m^2_{\pi,sea})/2 + \Delta^{I/D}_\text{mix} a^2$, the partially-quenched pion mass with mixed-action effect included [67], $m_{\pi,\text{v}}$ the valence pion mass and $m_{\pi,\text{sea}}$ the sea pion mass; $\Delta^I_\text{mix} = 0.041(6)$ GeV^4 and $\Delta^{ID}_\text{mix} = 0.0105(5)$ GeV^4; and t_0 is chosen to be its "optimal" value $t_0^\text{opt}(Q^2_\text{max}) = t_\text{cut}(1 - \sqrt{1 + Q^2_\text{max}/t_\text{cut}})$ to minimize the maximum value of $|z|$, with Q^2_max the maximum Q^2 under consideration.

In order to minimize the model dependence of the z-expansion fitting, we need to take k_max to be large enough such that the fit results are independent of the precise value of k_max. One way of achieving this is putting a Gaussian bound on the z-expansion a_k with central value 0. The choice of the Gaussian bound can be investigated using the Vector Meson Dominance (VMD) model with rho meson mass $m_\rho = 775$ MeV,

$$f_{\pi\pi}(Q^2) = \frac{1}{1 + Q^2/m^2_\rho}. \tag{4.3.10}$$

A non-linear least squares fit of this analytical function with z-expansion fitting at $k_\text{max} = 10$ gives $|a_k/a_0|_\text{max} < 1.03$, in which we used $t_\text{cut} = 4m^2_{\pi,\text{phys}}$, $t_0^\text{opt}(Q^2_\text{max}) = t_\text{cut}(1 - \sqrt{1 + Q^2_\text{max}/t_\text{cut}})$ and $Q^2_\text{max} = 1.0$ GeV^2. Also by investigating the z-expansion fits with $k_\text{max} = 3$ without priors of our data, we find $|a_k/a_0|_\text{max} < 3.0$. Thus we propose the use of conservative choice of Gaussian bound [66] with $|a_k/a_0|_\text{max} = 5$ for the pion form factor. The z-expansion fitted pion form factors up to $Q^2 \sim 1.0$ GeV^2 for the six lattices with the same valence and sea pion mass are shown in Fig. 4.7 with $\chi^2/d.o.f. \sim [0.4, 0.9]$.

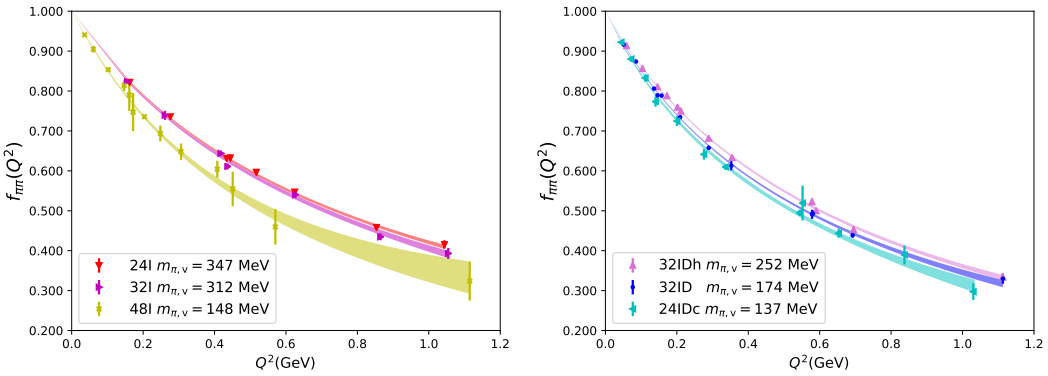

Figure 4.7: z-expansion fitting of the pion form factors on six gauge ensembles at their unitary pion mass with $k_{\max} = 3$ and $|a_k/a_0|_{\max} = 5$. The left panel is for the ensembles using Iwasaki gauge action and the Iwasaki+DSDR cases are shown in the right panel.

Another way to reach higher $k_{\max}$ and control the model dependence of fittings is using the fact that at the $Q^2 \to \infty$ limit $f_{\pi\pi}(Q^2)$ falls as $1/Q^2$ up to logarithms [68, 69]. Thus we have $Q^k f_{\pi\pi}(Q^2) \to 0$ for $k = 0, 1$ and follow the same argument in [66], which implies

$$\left.\frac{d^n}{dz^n} f_{\pi\pi}\right|_{z=1} = 0, \quad n \in \{0, 1\}, \tag{4.3.11}$$

with $z = 1$ corresponding to the $Q^2 \to \infty$ limit. These equations will lead to the two sum rules for pion form factors as

$$\sum_{k=0}^{\infty} a_k = 0, \quad \sum_{k=1}^{\infty} k a_k = 0. \tag{4.3.12}$$

With z-expansion fitting using Eq. (5.3.27), the charge radius of pion can be obtained through the definition in Eq. (4.1.2). The $\langle r_\pi^2 \rangle$ on different lattices with different valence pion masses are plotted in Fig. 4.9. We see that there is a strong dependence on the valence pion masses from the data points on each of the ensembles. Also, from the comparison of 32ID and 32IDh, we see that the data points line up as a function of $m^2_{\pi,\text{mix}}$ which evinces a strong dependence on the sea pion mass. The following fitting form as a function of $m^2_{\pi,\text{mix}}$ is used which includes an essential divergent log term from the $SU(3)$ NLO ChPT [51, 70],

$$\langle r_\pi^2 \rangle = \langle r_\pi^2 \rangle_{\text{phys}} + b_1 \ln \frac{m^2_{\pi,\text{mix}}}{m^2_{\pi,\text{phys}}} + b_2^{I/ID} a^2 + \frac{b_3 e^{-m_{\pi,\text{mix}} L}}{(m_{\pi,\text{mix}} L)^{3/2}}, \tag{4.3.13}$$

where the b_1 term reflects the pion mass dependence, $m_{\pi,\text{phys}} = 139.57$ MeV is the physical pion mass, L is the spatial size of the lattice, the $b_2^{I/ID}$ terms reflect the

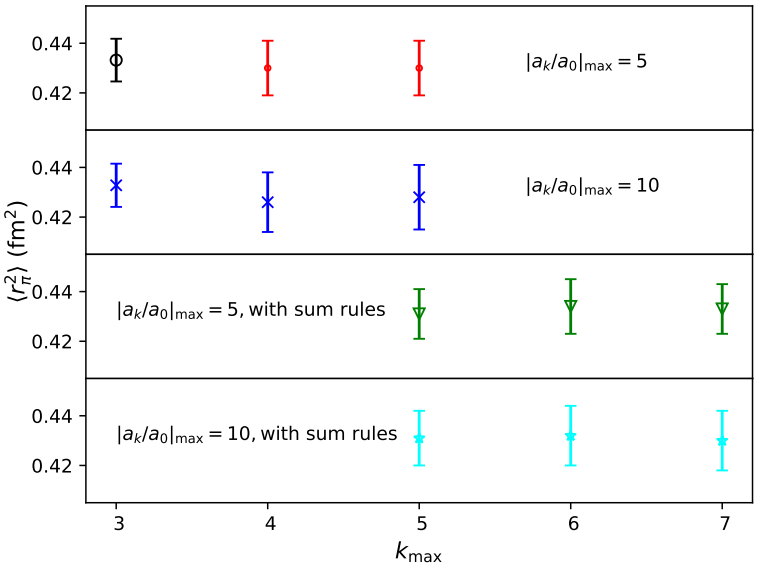

Figure 4.8: Comparison of extrapolated $\langle r_\pi^2 \rangle$ with z-expansion fits with different $k_{\max}$. The first and second sets are the fits with priors $|a_k/a_0|_{\max} = 5$ and $|a_k/a_0|_{\max} = 10$, respectively. The third and fourth sets are the similar fits constrained with the sum rules in Eq. (4.3.12).

lattice spacing dependence for the two sets of ensembles with different gauge actions (Iwasaki and Iwasaki plus DSDR), and the b_3 term accounts for the finite volume effect [71, 72, 13]. Since the kaon mass only varies a little in the current pion mass range, we do not include the kaon log term in the fitting.

The estimates of the extrapolated charge radius of the pion using Eq. (4.3.13) with different z-expansion fits are shown in Fig. 4.8. Since b_2^I and b_3 have no statistical significance, we use only three free parameters $\langle r_\pi^2 \rangle_{\text{phys}}$, b_1 and b_2^{ID} in these fits. All the fits have $\chi^2/d.o.f. \sim 0.6$ which is a good enough with $d.o.f. = 23$ and the central values and error values varying a little for different fits. Thus we take the result shown in black $\langle r_\pi^2 \rangle = 0.4332(86)$ fm^2 which corresponds to $k_{\max} = 3$ and $|a_k/a_0|_{\max} = 5$ as our fit result. The systematic uncertainties considered are listed as follows:

- The maximum difference between the result shown in black in Fig. 4.8 with the other fitted cases is treated as the systematic uncertainty from z-expansion fitting.

- The systematic uncertainty from the excited-state contaminations is estimated by changing the fit-ranges of 2pt and 3pt on 32ID with pion mass 174 MeV at the smallest momentum transfer which results in $f_{\pi\pi}(Q^2 = 0.051 \text{ GeV}^2) = 0.9158(14)(13)$; the second error corresponds to the systematic uncertainty from excited-state contaminations. This case is chosen because of its good signal/noise ratio which has the most control of the final result at close to the physical pion mass and the smallest momentum transfer is chosen due to its

largest influence on the radius. In order to estimate the systematic uncertainty of the radius from the form factor at only one small momentum transfer, we solve the VMD model in Eq. (4.3.10),

$$\frac{1}{1+(0.051\ \text{GeV}^2)/m_\rho} = 0.9158(14)(13) \tag{4.3.14}$$

with m_ρ as a free parameter. The predicted radius is

$$\langle r_\pi^2 \rangle = 6.0/m_\rho = 0.4190(74)(68)\ \text{fm}^2.$$

The second error 0.0068 fm^2, which propagates from the systematic uncertainty of the form factor, is treated as the systematic uncertainty from the change of fit ranges for the extrapolated charge radius.

- We added a linear dependence term between the charge radius of the pion and the pion mass squared as $b_4 M_\pi^2$ to Eq. (4.3.13) proposed by SU(2) NNLO ChPT [50] and repeated the fit with four free parameters $\langle r_\pi^2 \rangle_{\text{phys}}$, b_1, b_2^{ID} and b_4. The coefficient b_4 is consistent with zero and the prediction changed by 0.0032 fm^2 which is treated as the chiral extrapolation systematic uncertainty.

  Another source of the chiral extrapolation systematic uncertainty is the lack of a kaon log term in Eq. (4.3.13). On 24I, the valence pion masses ranging from 256 MeV to 391 MeV give a range of kaon mass from 514 MeV to 554 MeV. Thus we estimate the maximum kaon mass for the pion mass range in consideration to be $M_{K,\text{max}} = 554$ MeV. With the usage of SU(3) NLO ChPT [51], the systematic uncertainty from the kaon log term can be given by $\frac{1}{32\pi^2 F_0^2} \ln \frac{M_{K,\text{max}}^2}{M_{K,p}^2} = 0.0026$ fm^2, in which $F_0 = 93.3$ MeV and $M_{K,p} = 493$ MeV is the physical kaon mass.

- We repeated the fitting with four free parameters $\langle r_\pi^2 \rangle_{\text{phys}}$, b_1, b_2^{ID} and b_2^I which includes the discretization error from the Iwasaki gauge action and the prediction changed by 0.0025 fm^2. With this fitting, we get a difference between the fitting predictions in the continuum limit with those from the smallest lattice spacing (32I) to be 0.0018 fm^2. We combined these two as the systematic uncertainty of finite lattice spacing.

- With similar systematic analysis for finite volume effects with four free parameters $\langle r_\pi^2 \rangle_{\text{phys}}$, b_1, b_2^{ID} and b_3, the prediction changed by 0.0058 fm^2 and the difference between the fitting predictions in the infinite volume limit with those from the largest $m_\pi L = 5.8$ (32IDh) in our simulation is negligible.

Thus, the final result of the mean square charge radius of the pion at the physical pion mass in the physical limit reads

$$\begin{aligned} \langle r_\pi^2 \rangle &= 0.4332(86)_{\text{stat}}(72)_{z\text{-exp}}(68)_{\text{fit-range}}(41)_\chi(31)_{\text{a}}(58)_{\text{V}}\ \text{fm}^2 \\ &= 0.4332(86)(125)\ \text{fm}^2, \end{aligned} \tag{4.3.15}$$

with statistical error (stat) and systematic uncertainty from z-expansion fitting (z-exp), fit-range dependence (fit-range), chiral extrapolation (χ), finite lattice spacing (a), and finite volume (V). The total uncertainties at heavier pion masses are estimated from the scale of the total/statistical ratio at the physical pion mass.

The results of the fitting are shown in Fig. 4.9. One can see that our prediction of $\langle r_\pi^2 \rangle = 0.433(9)(13)$ fm^2 at the physical point is in very good agreement with the experimental result (the black dot). The discretization errors across the Iwasaki gauge ensembles are small while those across the Iwasaki plus DSDR gauge ensembles are obvious; this is consistent with what was found in the previous work with the DWF valence quark on similar RBC ensembles [16].

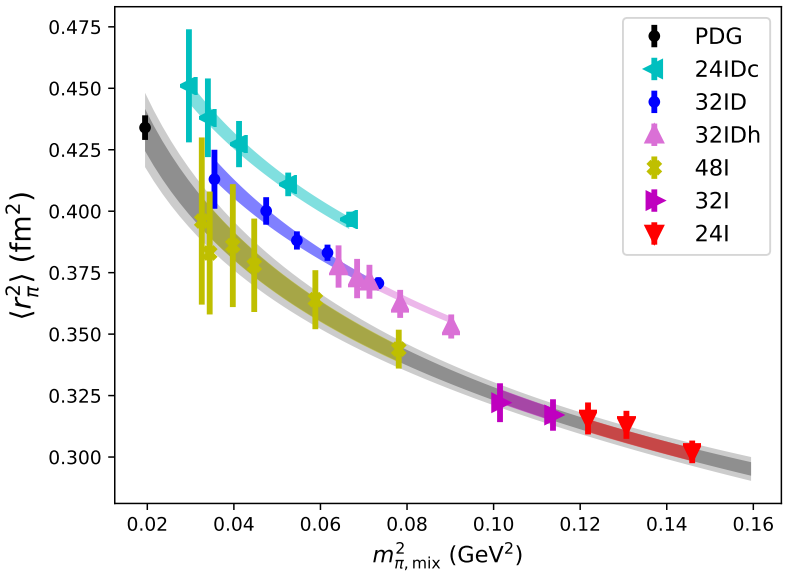

Figure 4.9: Pion radius squared $\langle r_\pi^2 \rangle$ as a function of $m^2_{\pi,\mathrm{mix}}$. Data points with different colors correspond to the results on the six ensembles with different sea pion masses. The colored bands show our prediction based on the global fit of $\langle r_\pi^2 \rangle$ with $\chi^2/d.o.f. = 0.65$; the inner gray band shows our prediction for the unitary case of equal pion mass in the valence and the sea in the continuum and infinite volume limits and the outer lighter gray band includes the systematic uncertainties from excited-state contaminations, z-expansion fitting, chiral extrapolation, lattice spacing and finite volume dependence.

Chiral extrapolation of the pion form factor

In order to make a prediction of the form factor at the continuum and infinite volume limits, we fit the inverse of the $f_{\pi\pi}(Q^2)$ data on different lattices with different valence

pion masses, as inspired from the NLO $SU(2)$ ChPT expansion [50, 51],

$$\frac{1}{f_{\pi\pi}(Q^2)} = 1 + \frac{Q^2}{6(4\pi F_\pi)^2}\left[\bar{l}_6 - \ln\frac{m^2_{\pi,\mathrm{mix}}}{m^2_{\pi,phys}} - 1 + R(s)\right] + Q^2 m^2_{\pi,\mathrm{mix}}(c_1 + c_2 Q^2) + c_3^{I/ID} a^2 Q^2 + c_4^{I/ID} a^2 Q^4 + \frac{Q^2}{(m_{\pi,\mathrm{mix}}L)^{3/2}}(c_5 + c_6\frac{Q^2}{m^2_{\pi,\mathrm{mix}}})e^{-M_\pi L}, \tag{4.3.16}$$

in which F_π and $\bar{l}_6$ are free parameters for fitting, c_1 and c_2 correspond to possible NNLO effects, $c_3^{I/ID}$ and $c_4^{I/ID}$ reflect the lattice spacing dependence terms, c_5 and c_6 correspond to the finite volume effect, and

$$R(s) = \frac{2}{3} + \left(1 + \frac{4}{s}\right)\left[\sqrt{1+\frac{4}{s}}\ln\frac{\sqrt{1+\frac{4}{s}}-1}{\sqrt{1+\frac{4}{s}}+1} + 2\right].$$

Since the inverse of $f_{\pi\pi}(Q^2)$ is mainly dominated by the NLO contributions considering the vector dominace of the pion form factor, fitting the inverse helps avoid the need of too many low-energy constants from NNLO corrections [13].

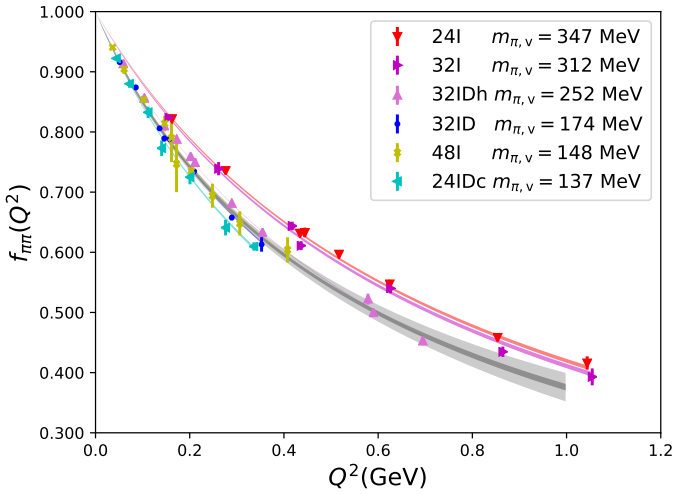

Figure 4.10: Pion form factor $f_{\pi\pi}(Q^2)$ on six gauge ensembles at their unitary pion mass with the bands from the chiral extrapolation fitting. The inner gray error band shows the fitting result and statistical error extrapolated to the physical limit and the outer ligher gray band corresponds to the inclusion of the systematic uncertainties from excited-state contaminations, NNLO corrections, chiral extrapolation, lattice spacing and finite volume dependence.

The fitting result of the chiral extrapolation of the pion form factor is shown in Fig. 4.10. We have made a cut of the Q^2 ranges used on each ensembles with $Q^2/m^2_{\pi,\mathrm{mix}} < 13$, so that the current formula can fully describe our data without the need of higher order terms of the ChPT expansion. The following systematic uncertainties are included in the analysis:

- With a variation of the fit-ranges of 2pt and 3pt on 32I with pion mass 312 MeV we got the form factor at large momentum transfer $f_{\pi\pi}(Q^2 = 0.865\ \text{GeV}^2) = 0.4347(87)(98)$. Along with previous analysis on 32ID at small momentum transfer $f_{\pi\pi}(Q^2 = 0.051\ \text{GeV}^2) = 0.9158(14)(13)$, we estimate the systematic uncertainty from the excited-state contaminations to be equal to the statistical uncertainty of the fitted pion form factors for all $Q^2 < 1.0\ \text{GeV}^2$.

- Since the c_1 and c_2 terms are just an estimation of the possible NNLO effects, we estimate the NNLO systematic uncertainty by setting c_1 and c_2 in Eq. (4.3.16) to be zero and treat the changes as systematic uncertainty from NNLO corrections.

- The systematic uncertainty from the lack of a kaon log term proposed by $SU(3)$ NLO ChPT is calculated with

$$\frac{Q^2}{12(4\pi F_0)^2}\left[\ln\frac{M_{K,\max}^2}{m_{K,p}^2}\right], \tag{4.3.17}$$

  which is the difference between using $M_{K,\max}$ and $m_{K,p}$ in the ChPT formula. This is treated as the systematic uncertainty from chiral extrapolation.

- We use the difference between the fitting predictions in the continuum limit with those from the smallest lattice spacing (32I) as systematic uncertainty of finite lattice spacing.

- The systematic uncertainty from finite volume effects is estimated by the difference between the fitting predictions in the infinite volume limit with those from the largest $m_\pi L = 5.8$ (32IDh).

The mean square charge radius of the pion from this fitting is $\langle r_\pi^2\rangle = 0.433(9)\ \text{fm}^2$, which is consistent with the above analysis, with $\chi^2/d.o.f. = 1.0$. Our extrapolated result at the physical pion mass and continuum and infinite volume limits for the curve $f_{\pi\pi}(Q^2)$ including the systematic uncertainties from excited-state contaminations, NNLO corrections, chiral extrapolation, lattice spacing and finite volume dependence, is shown and compared with experiments in Fig. 4.11; it goes through basically all the experimental data points up to $Q^2 = 1.0\,\text{GeV}^2$.

4.4 Summary

We have presented a calculation of the pion form factor using overlap fermions with a range of valence pion masses on six RBC/UKQCD domain-wall ensembles including two which have the physical pion mass. The lattice results for $\langle r_\pi^2\rangle$ in the continuum and infinite volume limits are compiled in Fig. 4.12 together with that of experiment. Our globally fitted pion mean square charge radius from the lattice data on six ensembles is $\langle r_\pi^2\rangle = 0.433(9)(13)\ \text{fm}^2$, which includes systematic errors from chiral extrapolation, finite lattice spacing and others; it agrees with experimental value of $\langle r_\pi^2\rangle = 0.434(5)\ \text{fm}^2$ within one sigma.

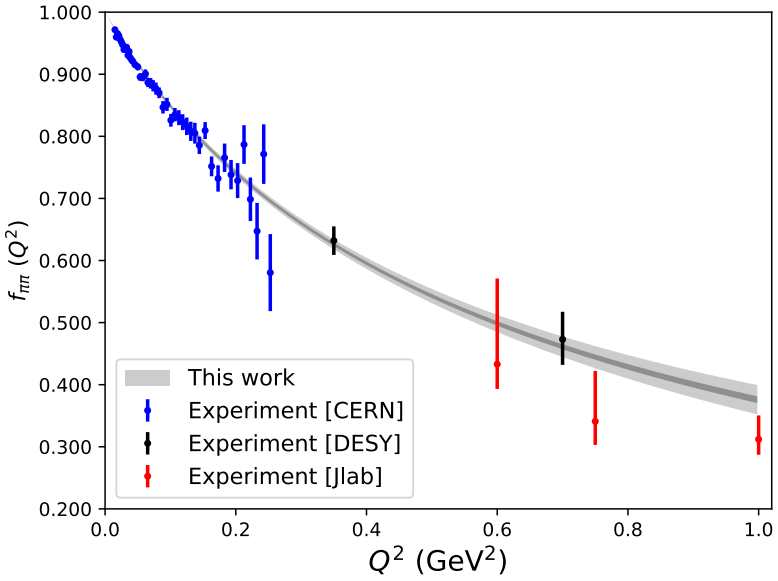

Figure 4.11: Comparison of the pion form factor $f_{\pi\pi}(Q^2)$ at physical pion mass with the CERN experiment at $Q^2 < 0.25$ GeV^2 [3] and the Jlab and DESY experimental data at larger Q^2 [4, 5, 6, 7, 8]. The inner gray band is the statistical error and the outer band includes the systematic uncertainties.

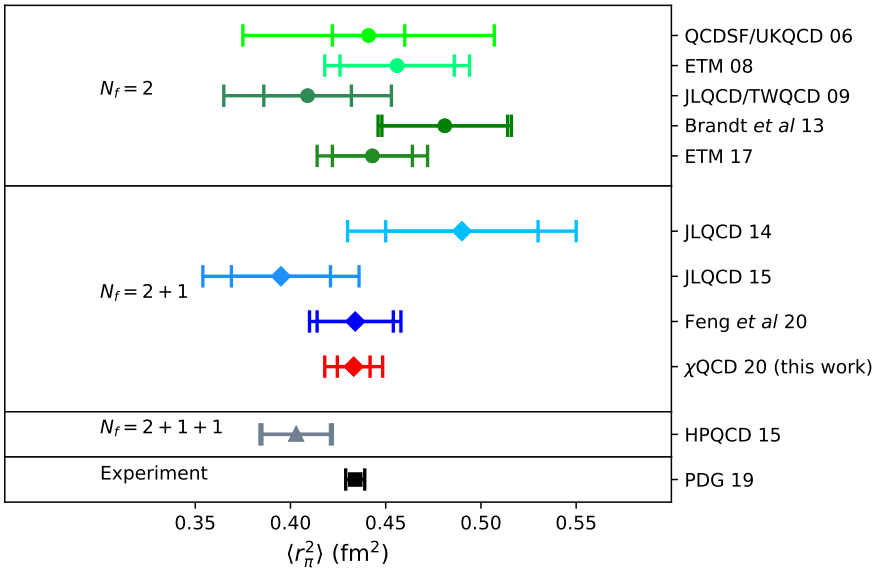

Figure 4.12: Summary of the pion radius results at the physical point. The lattice QCD results with different sea flavors are collected in different blocks, while all the results are consistent with each other within uncertainties. Numbers are from (QCDSF/UKQCD) [9], (ETM) [10], (JLQCD/TWQCD) [11], (Brandt et al.) [12], (ETM) [13], (JLQCD) [14, 15], (Feng et al.) [16], (HPQCD) [17], and (PDG) [18].

We find that $\langle r_\pi^2 \rangle$ has a strong dependence on both the valence and sea pion masses. More precisely, it depends majorly on the mass of the pion with one valence quark and one sea quark. We also give the extrapolated form factor $f_{\pi\pi}(Q^2)$, and the result agrees well with the experimental data points (up to $Q^2 = 1.0$ GeV^2).

Thus this work shows that the hadron form factor and the corresponding radius can be studied accurately and efficiently by combining LMS with the multi-mass algorithm of overlap fermions and FFT on the stochastic sandwich method, which provides the possibility to investigate the form factor of nucleon and its pion mass dependence with relatively small overhead on multiple quark masses and momentum transfers.

Chapter 5 Proton momentum and angular momentum fractions

5.1 Introduction

A quantitative understanding of the proton spin in terms of its fundamental quark and gluon constituents is an important and challenging question of hadron physics. It is expected that its spin arises from the intrinsic spin and orbital angular momentum of its constituents. Recent experiments using polarized deep inelastic lepton-nucleon scattering (DIS) processes show that the total helicity contribution from the quarks is just about 25-30% [73, 74, 75, 76, 77, 78] of the proton spin. The gluon helicity measured from polarized proton-proton collisions from the Relativistic Heavy Ion Collider (RHIC) [79, 80, 81] at BNL provide constraints on $\int_{0.05}^{0.2} \Delta g(x)dx = 0.06^{+0.11}_{-0.15}$ with a sizeable uncertainty.

On the other hand, Lattice QCD provides the *ab initio* non-perturbative framework to calculate the spin and momentum distributions of quarks and gluons constituents inside proton from the QCD action directly. The intrinsic spin carried by each quark flavor was first studied by χQCD [82] with followup calculations by χQCD [1], Extended Twisted Mass Collaboration (ETMC) [83, 84] and PNDME [85] which have provided results consistent with experiment at comparable uncertainties with $\Delta u = 0.777(25)(30)$, $\Delta d = -0.438(18)(30)$ and $\Delta s = -0.053(8)$ averaged by Flavour Lattice Averaging Group (FLAG) [86]. It is worth noting that the current predication of Δs from Lattice QCD is more precise than the phenomenological determinations. Gluon spin is determined in Ref. [58] to be 0.251(47)(16) at the physical pion mass in the $\overline{\text{MS}}$ scheme at $\mu^2 = 10$ GeV^2. Overlap fermions have been used in this calculation on $2+1$-flavor domain-wall fermion configurations with four lattice spacings and four volumes including an ensemble with physical quark mass. In order to address the angular mometnum fractions, a first attempt to fully decompose the proton spin was carried out by the χQCD collaboration in 2013 [87] in the quenched approximation and a lot of progress has been reached with dynamical fermions [88, 84, 89, 90, 91] including one with complete non-perturbative renormalization and normalization [92].

In this dissertation, we use the nucleon matrix element of the traceless, symmetric energy-momentum tensor (EMT) to determine the momentum and angular momentum fractions of up, down, strange and glue constituents inside the nucleon. Overlap fermions are used on $2+1$-flavor domain-wall fermion configurations with $m_\pi = 174$ MeV which is close to the physical pion mass. With a multi-mass inverter, we are able to simulate on several valence pion masses and extrapolate our results to the physical pion mass. Since the EMT of each parton species are not separately conserved, we summarize the final momentum and angular momentum fractions by considering mixing and non-perturbative renormalization at $\overline{\text{MS}}(\mu = 2\text{ GeV})$ and use the momentum and angular momentum conservations to normalize them.

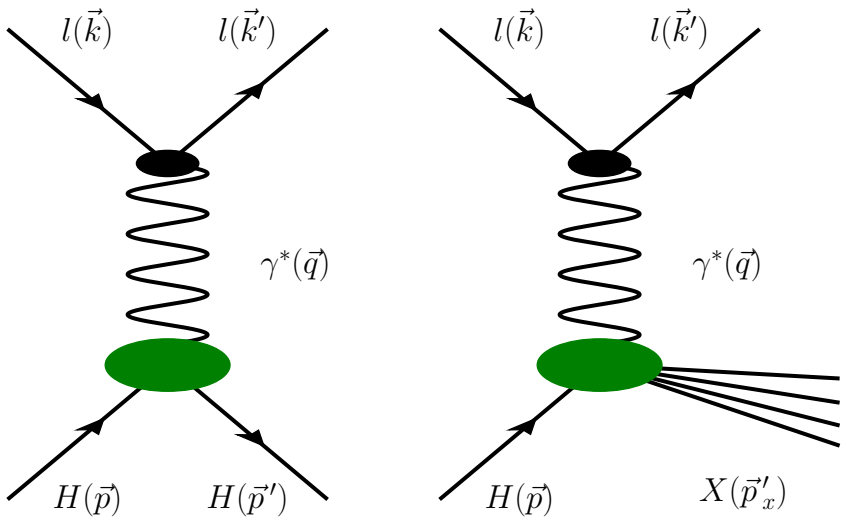

Figure 5.1: Left: Diagram for elastic lepton-hadron scattering with the hadron state remaining the same. Right: Diagram for deep inelastic scattering with the hadron blown apart into other particles.

5.2 Deep inelastic scattering

On the experimental side, deep inelastic scattering processes are the main tool to resolve individual quarks and gluons inside hadrons. Deep means the wavelength of initial lepton is much shorter than the size of the target hadron in this process. The process is called *elastic* when the incident and resultant particles remain the same as shown in the left diagram of Fig. 5.1. On the other hand, if the target hadron is blown apart to many resultant particles, the process is called *inelastic* as shown in the right diagram of Fig. 5.1. In the *inclusive* DIS, the energy and direction of the initial and final lepton are measured in the detector and the final hadronic states are not measured. If one or two hadronic states are measured, it is called *semi-inclusive* DIS. If all final hadronic states are measured, it is called *exclusive* scattering.

Kinematics

The basic DIS process can be denoted as

$$l(k) + H(p) \to l(k') + X(p'_x) \tag{5.2.1}$$

and the kinematic variables for DIS are

- $p = (M_H, \vec{0})$: The 4-momentum of the fixed hadron target with M_H the rest mass of the incoming hadron.

- $Q^2 = -q^2 = (k' - k)^2 = 4EE'\sin^2(\frac{\theta}{2})$: The momentum transfer of the virtual photon γ^* with θ the angle between the incoming and outgoing leptons, $k = (E, \vec{k})$ and $k' = (E', \vec{k}')$.
- $\nu = E - E' = p \cdot q / M_H$: The energy loss of the lepton which is the energy of the virtual photon γ^*.
- $y = \nu / E$: The fractional energy loss of the lepton.
- $x_B = \frac{Q^2}{2p \cdot q} = \frac{Q^2}{2M_H \nu}$: The Bjorken scaling variable.

The information of DIS is collected in the structure functions and at leading order with $Q^2 \to \infty$, the hadron structure functions depend only on the fixed scaling variable x proposed by Bjorken [93, 94] and depend on the dimensional parameter Q^2 logarithmically. Since the total mass of the final hadron state M_X must be the same or larger than the hadron mass M_H, we have,

$$M_X^2 = (p+q)^2 = M^2 + 2p \cdot q + q^2 \geq M^2 \quad \Rightarrow x_B = \frac{Q^2}{2p \cdot q} \leq 1. \tag{5.2.2}$$

We also have that both $Q^2 = -q^2$ and $p \cdot q$ are positive so that

$$0 \leq x_B \leq 1. \tag{5.2.3}$$

DIS Cross Section

The cross section for the unpolarized DIS in the laboratory frame is given by

$$\frac{d^2\sigma}{d\Omega dE'} = \frac{e^4}{16\pi^2 Q^4}(\frac{E'}{M_N E}) L_{\mu\nu}(p,q) W^{\mu\nu}(p,q) \tag{5.2.4}$$

in which e is the electron charge, $L_{\mu\nu}$ is the leptonic tensor which can be determined from perturbative QED, and $W^{\mu\nu}$ is the hadronic tensor. $L_{\mu\nu}$ can be written as

$$L_{\mu\nu} = \sum_{\text{final states}} \langle k' | J_l^\mu | k, s_l \rangle \langle k, s_l | J_l^\nu | k' \rangle , \tag{5.2.5}$$

with J_l the leptonic current, s_l the final lepton polarization vector and the sum is over all possible leptonic final states. At leading order and neglecting the lepton mass, $L_{\mu\nu}$ is

$$L_{\mu\nu} = p'_\mu p_\nu + p'_\nu p_\mu - g_{\mu\nu} p' \cdot p. \tag{5.2.6}$$

With the optical theorem, the hadronic tensor can be expressed as the imaginary part of the forward scattering amplitude in deeply virtual Compton scattering as

$$W_{\mu\nu} = \frac{1}{2\pi} \text{Im} T_{\mu\nu}, \tag{5.2.7}$$

with

$$T_{\mu\nu} = i \sum_{s',s} \int d^4x e^{iq\cdot z} \langle p, s' | \mathcal{T}[J_\mu(z), J_\nu(0)] | p, s \rangle , \tag{5.2.8}$$

in which $\mathcal{T}[\cdots]$ is the time-ordered product and s the polarization of the hadron. Thus we have

$$W_{\mu\nu}(p,q) = \sum_{s',s} \frac{1}{4\pi} \int d^4z e^{iq\cdot z} \langle p, s' | J_\mu(z), J_\nu(0) | p, s \rangle , \tag{5.2.9}$$

which is the spin independent part of the hadronic tensor for unpolarized scattering. With the usage of current conservation, parity conservation and time reversal invariance, we can write the hadronic tensor for a spin-1/2 target as

$$W^{\mu\nu}(p,q) = -F_1(x,Q^2)(g^{\mu\nu} - \frac{q^\mu q^\nu}{q^2}) + \frac{F_2(x,Q^2)}{p\cdot q}(p^\mu - \frac{p\cdot q}{q^2}q^\mu)(p^\nu - \frac{p\cdot q}{q^2}q^\nu). \tag{5.2.10}$$

In the Bjorken limit, $Q^2 \to \infty$ and $\nu \to \infty$, the structure functions F_1 and F_2 depend only on x and the Bjorken scaling functions are related by the Callan-Gross relation [95],

$$F_2(x) = \sum_q e_q^2 \, x \, q(x) = 2 \, x \, F_1(x), \tag{5.2.11}$$

where e_q is the electric charge of the quark with different flavor, and $q(x)$ is the probability of finding a parton with a longitudinal momentum x, which is called parton distribution function (PDF). It is a sum of the corresponding quark and anti-quark distributions as

$$q(x) = (q_\uparrow + q_\downarrow)(x) + (\bar{q}_\uparrow + \bar{q}_\downarrow)(x). \tag{5.2.12}$$

Operator Product Expansion

The structure functions can be related to the matrix elements of local operators between hadronic states with the operator product expansion (OPE) [96]. At the short-distance limit $z^2 \to 0$, the current product in Eq. (5.2.9) can be expanded with a series of local operators,

$$\lim_{z^2\to 0} J_i(z) J_j(0) = \sum_k c_{ijk}(z,\mu)\mathcal{O}_k(0,\mu) \tag{5.2.13}$$

where $c_{ijk}(z)$ are the Wilson coefficients which depend on the separation z and energy scale μ but are independent of the matrix elements, and $\mathcal{O}_k(0)$ are a tower of local operators $\mathcal{O}_n^{\mu_1,\cdots,\mu_n}$ which are traceless and symmetric in the indices μ_i. We group these operators with $t = d - n$ which is called *twist* of the operators with d the dimension and n the spin of the operator. The leading contributions of the expansion have $t = 2$ which are written in terms of quark fields $\psi(d = 3/2, n = 1/2, t = 1)$, gluon fields $F_{\mu\nu}(d = 2, n = 1, t = 1)$ and covariant derivatives $\mathcal{D}(d = 1, n = 1, t = 0)$. Adding derivatives $\mathcal{D}(t = 0)$ to the operator will not change the twist. For example,

the general forms of traceless twist-two operators for quarks in Minkowski space are written as

$$\begin{aligned}\mathcal{O}_q^{\{\mu_1\cdots\mu_n\}} &= i^{n-1}\bar{\psi}^{(f)}\gamma^{\{\mu_1}\overleftrightarrow{\mathcal{D}}_2^{\mu}\cdots\overleftrightarrow{\mathcal{D}}^{\mu_n\}}\psi^{f'},\\ \mathcal{O}_{\sigma q}^{[\mu_1\{\nu]\cdots\mu_n\}} &= i^{n}\bar{\psi}^{(f)}\sigma^{[\mu_1\{\nu]}\overleftrightarrow{\mathcal{D}}_2^{\mu}\cdots\overleftrightarrow{\mathcal{D}}^{\mu_n\}}\psi^{f'},\end{aligned} \tag{5.2.14}$$

with $\psi^{(f)}$ the quark field with flavor f, $\overleftrightarrow{\mathcal{D}}_\mu = 1/2(\overrightarrow{\mathcal{D}}_\mu - \overleftarrow{\mathcal{D}}_\mu)$ the symmetrized covariant derivative and $\sigma^{\mu\nu} = i/2[\gamma_\mu, \gamma_\nu]$. Notation $\{\mu_1\cdots\mu_2\}$ means symmetrization of μ_i's and $[\mu_1\mu_2]$ means anti-symmetrization of μ_1 and μ_2.

5.3 Lattice operators and nucleon form factors

In order to evaluate angular momentum fractions of nucleon on the lattice, we follow Ref. [97, 87] to use the traceless, symmetric QCD energy-momentum tensor (EMT) as the current operator. The ith component of angular momentum operator for quarks and glue can be written with EMT as

$$J_i^{q,g} = \frac{1}{2}\epsilon^{ijk}\int d^3x\left(\mathcal{T}^{\{0k\}q,g}x^j - \mathcal{T}^{\{0j\}q,g}x^k\right), \tag{5.3.1}$$

where $\mathcal{T}^{\{0j\}q,g}$ are the gauge-invariant and conserved EMT operators for quark and gluon parts, respectively. Also, the linear momentum operators are

$$P_i^{q,g} = \int d^3x\mathcal{T}^{\{0i\}q,g}. \tag{5.3.2}$$

The nucleon matrix element of EMT can be decomposed into three generalized form factors (GFFs) based on their associated spinor structures as

$$\begin{aligned}\langle p',s'|\,\mathcal{T}^{\{\mu\nu\}q,g}\,|p,s\rangle \;=&\frac{1}{2}\bar{u}(p',s')\Big[T_1(q^2)(\gamma^\mu\bar{p}^\nu+\gamma^\nu\bar{p}^\mu)\\ &+\frac{1}{2m}T_2(q^2)\left(iq_\alpha(\bar{p}^\mu\sigma^{\nu\alpha}+\bar{p}^\nu\sigma^{\mu\alpha})\right)+\frac{1}{m}T_3(q^2)q^\mu q^\nu\Big]^{q,g}u(p,s)\end{aligned} \tag{5.3.3}$$

where $|p,s\rangle$ is the nucleon initial state with momentum p and spin s, $\langle p',s'|$ is the nucleon final state with momentum p' and spin s, $\bar{u}$ and u are the initial and final nucleon spinors, $q = p' - p$ is the momentum transfer, $\bar{p} = (p'+p)/2$ is the the total momentum, and T_1, T_2 and T_3 are the three generalized form factors.

With the insertions of Eq.(5.3.3) into Eq.(5.3.1) and Eq.(5.3.2) in the $q^2 \to 0$ limit, we obtain

$$J^{q,g} = \frac{1}{2}\left[T_1(0)+T_2(0)\right]^{q,g},\ \langle x\rangle^{q,g} = T_1(0)^{q,g} \tag{5.3.4}$$

in which $J^{q,g}$ is the the total angular momentum fraction for quarks and glue, respectively and $\langle x\rangle^{q,g}$ is the second moment of the momentum distribution.

In this dissertation, we will focus on the calculation of $\mathcal{T}_{4i}$ which is adequate to give the $T_1(0)$ and $T_2(0)$ form factors. Following from the conservation of EMT, the momentum and angular momentum are conserved with sum rules

$$\begin{aligned} \langle x\rangle^q + \langle x\rangle^g &= T_1(0)^q + T_1(0)^g = 1, \\ J^q + J^g &= \frac{1}{2}\{[T_1(0)^q + T_2(0)^q] + [T_1(0) + T_2(0)]^g\} = \frac{1}{2}. \end{aligned} \tag{5.3.5}$$

One implication of these two sum rules is that the sum of $T_2(0)$'s for the quarks and gluons is zero, that is,

$$T_2(0)^q + T_2(0)^g = 0, \tag{5.3.6}$$

which has been derived in [98, 99].

Quark and gluon operators

The EMT matrix elements of Eq.(5.3.3) in Euclidean space-time with current Pauli-Sakurai γ matrices convention is

$$\begin{aligned} \langle p', s'|\, \mathcal{T}_{4i}^{q,g(E)}\, |p, s\rangle = \frac{1}{2}\bar{u}^{(E)}(p', s')\Big[T_1(-q^2)(\gamma_4\bar{p}_i + \gamma_i\bar{p}_4) \\ - \frac{1}{2m}T_2(-q^2)\left(q_\alpha(\bar{p}_4\sigma_{i\alpha} + \bar{p}_i\sigma_{4\alpha})\right) - \frac{i}{m}T_3(-q^2)q_4q_i\Big]^{q,g} u^{(E)}(p, s), \end{aligned} \tag{5.3.7}$$

in which $\mu, \nu \in \{1, 2, 3, 4\}$ is the Euclidean space-time index and the normalization conditions of $\bar{u}^{(E)}$ and $u^{(E)}$ are

$$\bar{u}^{(E)}(p, s)u^E(p, s) = 1,\ \sum_s u^E(p, s)\bar{u}^{(E)}(p, s) = \frac{\not{p} + m}{2m}. \tag{5.3.8}$$

The associated Euclidean gluon EMT is

$$\mathcal{T}_{4i}^{g(E)} = (+i)\left[-\frac{1}{2}\sum_{k=1}^{3} 2\mathrm{Tr}^{\mathrm{color}}[G_{4k}G_{ki} + G_{ik}G_{k4}]\right], \tag{5.3.9}$$

in which $G_{\mu\nu}$ is the Euclidean field-strength tensor

$$G_{\mu\nu}^{(E)}(x) = \frac{1}{8}\left(P_{\mu\nu}(x) - P_{\mu\nu}^\dagger(x)\right), \tag{5.3.10}$$

with $P_{\mu\nu}$ being the "cloverleaf"

$$\begin{aligned} P_{\mu\nu} = U_\mu(x)U_\nu(x+\mu)U_\mu^\dagger(x+\nu)U_\nu^\dagger(x) \\ + U_\nu(x)U_\mu^\dagger(x-\mu+\nu)U_\nu^\dagger(x-\mu)U_\mu(x-\mu) \\ + U_\mu^\dagger(x-\mu)U_\nu^\dagger(x-\mu-\nu)U_\mu(x-\mu-\nu)U_\nu(x-\nu) \\ + U_\nu^\dagger(x-\nu)U_\mu(x-\nu)U_\nu(x-\nu+\mu)U_\mu^\dagger(x) \end{aligned} \tag{5.3.11}$$

which is built from the HYP-smeared gauge links. The difference between the bare matrix elements and the HYP-smeared matrix elements will be compensated by the non-perturbative renormalization procedure [90].

The Euclidean quark EMT is

$$\mathcal{T}_{4i}^{q(E)} = (-1)\frac{i}{4}\sum_f \bar{\psi}_f \left[\gamma_4 \overrightarrow{D}_i + \gamma_i \overrightarrow{D}_4 - \gamma_4 \overleftarrow{D}_i - \gamma_i \overleftarrow{D}_4\right] \psi_f, \tag{5.3.12}$$

In order to discretize $\mathcal{T}_{4i}^{q(E)}$, we use the following left and right gauge covariant derivatives on the lattice,

$$\begin{aligned} \overrightarrow{D}_\mu \psi(x) &= \frac{1}{2a}\left[U_\mu(x)\psi(x+a_\mu) - U_\mu^\dagger(x-a_\mu)\psi(x-a_\mu)\right], \\ \bar{\psi}(x)\overleftarrow{D}_\mu &= \frac{1}{2a}\left[\bar{\psi}(x+a_\mu)U_\mu^\dagger(x) - \bar{\psi}(x-a_\mu)U_\mu^\dagger(x-a_\mu)\right], \end{aligned} \tag{5.3.13}$$

each ψ being a quark field operator on the lattice and each U a gauge link. Thus the quark EMT operator for flavor f is

$$\begin{aligned} \mathcal{T}_{4i}^{q}(x) = \frac{-i}{8a}\big[&\bar{\psi}_f(x)\gamma_4 U_i(x)\psi_f(x+a_i) - \bar{\psi}_f(x)\gamma_4 U_i^\dagger(x-a_i)\psi_f(x-a_i) \\ &+ \bar{\psi}_f(x-a_i)\gamma_4 U_i(x-a_i)\psi_f(x) - \bar{\psi}_f(x+a_i)\gamma_4 U_i^\dagger(x)\psi_f(x) \\ &+ \bar{\psi}_f(x)\gamma_i U_4(x)\psi_f(x+a_4) - \bar{\psi}_f(x)\gamma_i U_4^\dagger(x-a_4)\psi_f(x-a_4) \\ &+ \bar{\psi}_f(x-a_4)\gamma_i U_4(x-a_4)\psi_f(x) - \bar{\psi}_f(x+a_4)\gamma_i U_4^\dagger(x)\psi_f(x)\big]. \end{aligned} \tag{5.3.14}$$

Three-point correlation functions

The EMT matrix element can be extracted from the three-point function (3pt) along with the associated two-point function (2pt) as

$$G_{\alpha\beta}^{NN}(\vec{p},t) = \sum_{\vec{x}} e^{-i\vec{p}\cdot\vec{x}} \langle 0|\, T[\chi_\alpha(\vec{x},t)\bar{\chi}_\beta(\vec{0},0)]\,|0\rangle\,, \tag{5.3.15}$$

with $\chi(x) = \mathcal{O}_N(x)$ and $\bar{\chi}(x) = \bar{\mathcal{O}}_N(x)$ the nucleon interpolation fields defined in Eq. (3.1.17) and Eq. (3.1.18), respectively. In the $t \gg 1$ limit, the unpolarized nucleon two-point function $C_{2\mathrm{pt}}(\vec{p},t)$ is

$$C_{2\mathrm{pt}}(\vec{p},t) \equiv \mathrm{Tr}[\Gamma_0 G^{NN}(\vec{p},t)] \xrightarrow{t\gg 1} \frac{Z_p^2}{(La)^3}\frac{E_p+m}{E_p}e^{-E_p(t-t_0)} + Ae^{-E_p^1(t-t_0)}, \tag{5.3.16}$$

in which $\Gamma_0 = P_+ = \frac{1+\gamma_4}{2}$ is the unpolarized projection for the nucleon, Z_p is the spectral weight, m is the nucleon rest mass, E_p and E_p^1 are the ground state energy and first excited-state energy, respectively, and A is an unknown parameter associated with the excited-state contaminations. The 3pt of EMT is

$$\begin{aligned} G_{\alpha\beta}^{N\mathcal{T}_{4i}^{q,g}N}(t',t,\vec{p}',\vec{p}) = \sum_{\vec{x}',\vec{z}} &e^{-i\vec{p}'\cdot(\vec{x}'-\vec{z})}e^{i\vec{p}\cdot\vec{z}}\times \\ &\langle 0|\, T[\chi_\alpha(\vec{x}',t')\mathcal{T}_{4i}^{q,g}(\vec{z},t)\bar{\chi}_\beta(\vec{0},0)]\,|0\rangle\,, \end{aligned} \tag{5.3.17}$$

in which $z = \{\vec{z}, t\}$ is the current position, $x' = \{\vec{x}', t'\}$ is the sink position, $\vec{p}'$ is the momentum of the final nucleon, and $\vec{p}$ is the momentum of the initial nucleon. With the unpolarized/polarized projection for the nucleon, we define $C_{3\text{pt}}$ as

$$C_{3\text{pt}}(\mu, 4, i; t', t, \vec{p}', \vec{p}) \equiv \text{Tr}[\Gamma_\mu G^N \mathcal{T}_{4i}^{q,g} {}^N(t', t, \vec{p}', \vec{p})], \tag{5.3.18}$$

with $\mu \in \{0, 1, 2, 3\}$, Γ_0 the unpolarized projection for nucleon, and Γ_1, Γ_2 and Γ_3 the polarized projection in the x, y, z direction, respectively, as

$$\Gamma_m = \begin{cases} \frac{1+\gamma_4}{2}\sigma_{23}, \text{ for } m = 1 \\ \frac{1+\gamma_4}{2}\sigma_{31}, \text{ for } m = 2 \\ \frac{1+\gamma_4}{2}\sigma_{12}, \text{ for } m = 3 \end{cases}, \tag{5.3.19}$$

where $\sigma_{ij} = \frac{1}{2i}[\gamma_i, \gamma_j]$. With an insertion of a complete set of energy eigenstates in Eq. (5.3.16), we get

$$\begin{aligned} C_{3\text{pt}}(\mu, 4, i; t', t, \vec{p}', \vec{p}) \xrightarrow[t'-t \gg 1]{t' \gg 1} \frac{Z_{p'} Z_p}{4 E_{p'} E_p} e^{-E_p(t'-t)} e^{-E_{p'} t} \times \\ \left[a_1 T_1(Q^2) + a_2 T_2(Q^2) + a_3 T_3(Q^2)\right], \end{aligned} \tag{5.3.20}$$

where the a_is are known coefficients which depend on the momentum and energy of the nucleon which we calculate using 'python' script, and $Q^2 = (p' - p)^2$ is the momentum transfer squared. In order to extract $T_1(Q^2)$, $T_2(Q^2)$ and $T_3(Q^2)$, we take the ratios of 3pt and 2pt functions,

$$\begin{aligned} R(\mu, 4, i; t', t, \vec{p}', \vec{p}) &\equiv \frac{C_{3\text{pt}}(\mu, 4, i; t, t', \vec{p}', \vec{p})}{C_{2\text{pt}}(\vec{p}', t')} \times \sqrt{\frac{C_{2\text{pt}}(\vec{p}, t'-t) C_{2\text{pt}}(\vec{p}', t) C_{2\text{pt}}(\vec{p}', t')}{C_{2\text{pt}}(\vec{p}', t'-t) C_{2\text{pt}}(\vec{p}, t) C_{2\text{pt}}(\vec{p}, t')}} \\ &\xrightarrow[t'-t \gg 1]{t' \gg 1} \frac{a_1 T_1(Q^2) + a_2 T_2(Q^2) + a_3 T_3(Q^2)}{4\sqrt{E_{p'}(E_{p'} + m) E_p (E_p + m)}}. \end{aligned} \tag{5.3.21}$$

In this dissertation, we focus on the evaluation of the T_1 and $[T_1 + T_2]$ form factors by choosing specific momentum and polarization projection settings. We set the initial and final momentum of the nucleon to be the same to approach T_1 form factor,

$$R(\Gamma_i, 4, j; t', t, \vec{p}, \vec{p}) \to \epsilon_{i,j,k} p_k T_1(0), \tag{5.3.22}$$

with $i, j \in \{1, 2, 3\}$, The following settings are used to calculate $[T_1 + T_2]$ form factor,

$$\begin{aligned} R(\Gamma_i, 4, j; t', t, \vec{p}, \vec{0}) &\to \epsilon_{i,j,k} p_k [T_1 + T_2](Q^2), \\ R(\Gamma_i, 4, j; t', t, \vec{0}, \vec{p}) &\to \epsilon_{i,j,k} p_k [T_1 + T_2](Q^2), \\ R(\Gamma_i, 4, j; t', t, \vec{p}, -\vec{p}) &\to \epsilon_{i,j,k} p_k [T_1 + T_2](Q^2), \end{aligned} \tag{5.3.23}$$

in which the first two momentum settings have either initial/final momentum to be $\vec{0}$, while the third corresponds to the case where the initial and final momentum of the nucleon are in opposite directions which will result in larger momentum transfers.

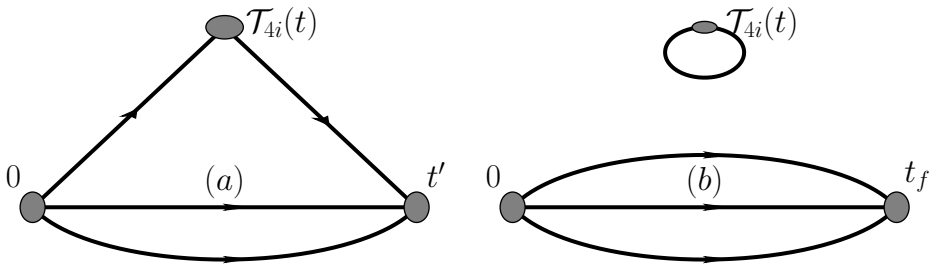

Figure 5.2: Illustration of the nucleon three-point functions with (a) connected insertions (CI) and (b) disconnected insertions (DI).

With the usage of Wick contractions, the evaluation of 3pt in Eq. (5.3.17) on the lattice gives two topologically distinct contributions: connected insertions (CI) and disconnected insertions (DI), which are shown in Fig. 5.2. In the case of CI, the quark/anti-quark from current $\mathcal{T}_{4i}$ is contracted with the quark/anti-quark from the source/sink nucleon interpolating fields. Whereas, in the case of DI, the quark/anti-quark from current $\mathcal{T}_{4i}$ is contracted with itself at current position z to form a loop.

The evaluation of CI cases can be done with the method described in Sec. 3.4. This method allows the usage of FFT to get any combinations of $\vec{p}'$ and $\vec{p}$ so that we can average over different directions to increase statistics. For the DI case, the gauge-averaged three-point function can be written as

$$\begin{aligned} C_{3\mathrm{pt}}(\mu,4,i;t',t,\vec{p}',\vec{p})_{\mathrm{DI}} &= \sum_{\vec{z},\vec{x}'} e^{-i\vec{p}'\cdot\vec{x}'} e^{i\vec{q}\cdot\vec{z}} \times \langle 0| \left[\chi_\alpha(\vec{x}',t')\bar{\chi}_\beta(\vec{0},0)\right] \times [\mathcal{T}_{4i}(\vec{z},t)]\,|0\rangle \\ &= \langle \mathrm{Tr}[\Gamma_\mu G^{NN}(\vec{p},t;U)] \times L[t,\vec{q};U]\rangle - \langle \mathrm{Tr}[\Gamma_\mu G^{NN}(\vec{p},t;U)]\rangle \times \langle L[4,i,t,\vec{q};U]\rangle\,, \end{aligned} \tag{5.3.24}$$

in which $\langle\cdots\rangle$ denotes the gauge average and $G^{NN}(\vec{p},t;U)$ is the computation of nucleon propagator under gauge field U and $L[4,i,t,\vec{q};U]$ is the current loop of quark/gluon. We have subtracted the uncorrelated part of the loop and the nucleon propagator. The quark loop $L = L^f[4,i,t,\vec{q};U]$ is constructed from the propagator of quark flavor f as

$$\begin{aligned} L^f[4,i,t,\vec{q};U] = \frac{i}{8a}\sum_{\vec{z}} e^{i\vec{q}\cdot\vec{z}} \\ \mathrm{Tr}\Big\{ & D_f^{-1}(z+a_i,z;U)\gamma_4 U_i(z) - D_f^{-1}(z-a_i,z;U)\gamma_4 U_i^\dagger(z-a_i) \\ & + D_f^{-1}(z,z-a_i;U)\gamma_4 U_i(z-a_i) - D_f^{-1}(z,z+a_i;U)\gamma_4 U_i^\dagger(z) \\ & + D_f^{-1}(z+a_4,z;U)\gamma_i U_4(z) - D_f^{-1}(z-a_4,z;U)\gamma_i U_4^\dagger(z-a_4) \\ & + D_f^{-1}(z,z-a_4;U)\gamma_i U_4(z-a_4) - D_f^{-1}(z,z+a_4;U)\gamma_i U_4^\dagger(z)\Big\}\,, \end{aligned} \tag{5.3.25}$$

in which the trace Tr is the trace over color and spin, and $D_f^{-1}(z+a_i,z;U)$ is the quark propagator from point z to point $z+a_i$ under gauge field U with flavor f. In

the case of the gluon three-point function, only DI contributes as in Eq. (5.3.24) with the current loop $L = L^g[4, i, t, \vec{q}; U]$ as

$$L^g[4,i,t,\vec{q};U] = (+i)\sum_{\vec{z}} e^{i\vec{q}\cdot\vec{z}}\times \left[-\frac{1}{2}\sum_{k=1}^{3} 2\mathrm{Tr}^{\mathrm{color}}[G_{4k}(z)G_{ki}(z) + G_{ik}(z)G_{k4}(z)]\right], \tag{5.3.26}$$

with the field-strength tensor $G_{\mu\nu}$ defined in Eq. (5.3.10).

z-Expansion fit

In order to fit the $[T_1+T_2](Q^2)$ form factor and extrapolate it to $Q^2 = 0$, we have done a model-independent z-expansion [66] fit using the following equation with $k_{\max} \geq 2$,

$$\begin{aligned} T(Q^2) &= \sum_{k=0}^{k_{\max}} a_k z^k \\ z(t, t_{\mathrm{cut}}, t_0) &= \frac{\sqrt{t_{\mathrm{cut}} - t} - \sqrt{t_{\mathrm{cut}} - t_0}}{\sqrt{t_{\mathrm{cut}} - t} + \sqrt{t_{\mathrm{cut}} - t_0}}, \end{aligned} \tag{5.3.27}$$

where $T(Q^2)$ represent a nucleon form factor such as T_1, T_2, T_3 and their linear combinations such as $[T_1 + T_2]$; $t = -Q^2$; $t_{\mathrm{cut}} = 4m_\pi^2$ corresponds to the two-pion production threshold with $m_\pi = 172$ MeV chosen to be the sea pion mass; and t_0 is chosen to be its "optimal" value $t_0^{\mathrm{opt}}(Q^2_{\max}) = t_{\mathrm{cut}}(1 - \sqrt{1 + Q^2_{\max}/t_{\mathrm{cut}}})$ to minimize the maximum value of $|z|$, with $Q^2_{\max}$ the maximum Q^2 under consideration.

In order to remove the model dependence of the z-expansion fitting, we need to take $k_{\max}$ to be large enough such that the fit results are independent of the precise value of $k_{\max}$. One way of achieving this is putting a Gaussian bound on the z-expansion parameter a_k with central value 0. We adopt the Gaussian bound proposed in [66] with $|a_k/a_0|_{\max} < 5.0$.

Another way to reach higher $k_{\max}$ and control the model dependence of fittings is using the fact that at the $Q^2 \to \infty$ limit nucleon form factors fall as $1/Q^4$ up to logarithms [100]. Thus we have $Q^k T(Q^2) \to 0$ for $k = 0, 1, 2, 3$ and following the same argument in [66], this implies

$$\left.\frac{d^n}{dz^n} T\right|_{z=1} = 0, \quad n \in \{0, 1, 2, 3\}, \tag{5.3.28}$$

with $z = 1$ corresponding to the $Q^2 \to \infty$ limit. These equations lead to the sum rules for nucleon form factors as

$$\begin{aligned} &\sum_{k=0}^{\infty} a_k = 0, \sum_{k=1}^{\infty} k a_k = 0, \\ &\sum_{k=2}^{\infty} k(k-1)a_k = 0 \text{ and } \sum_{k=3}^{\infty} k(k-1)(k-2)a_k = 0. \end{aligned} \tag{5.3.29}$$

In practice, instead of ∞, the summation of k will have an upper limit $k_{\max}$ chosen to be large enough to minimize model dependence.

5.4 Operator mixing and renormalization

Although the total form factors T_1, T_2 and T_3, with $T(Q^2) \equiv \sum_{a=u,d,\cdots,g} T^a(Q^2)$, are renormalization and scale invariant, the quark and gluon pieces are not separately conserved. We renormalize our results at $\overline{\rm MS}(\mu = 2\ {\rm GeV})$ with a nonperturbative renormalization procedure. As lattice breaks down rotational symmetry to the hypercubic group $H(4)$, the EMT operators subduce into two traceless, symmetric irreducible representations of $H(4)$ which are labelled with $\tau_1^{(3)}$ and $\tau_1^{(6)}$ [101, 102]. They do not mix with same or lower-dimension operators. In Euclidean space, a basis of operators in the three-dimensional $\tau_1^{(3)}$ representation is [89]

$$\begin{aligned} \mathcal{T}_1^{\tau_1^{(3)}} &= \frac{1}{2}(\mathcal{T}_{11} + \mathcal{T}_{22} - \mathcal{T}_{33} + \mathcal{T}_{44}), \\ \mathcal{T}_2^{\tau_1^{(3)}} &= \frac{1}{\sqrt{2}}(\mathcal{T}_{33} + \mathcal{T}_{44}),\ \mathcal{T}_3^{\tau_1^{(3)}} = \frac{1}{\sqrt{2}}(\mathcal{T}_{11} - \mathcal{T}_{22}). \end{aligned} \tag{5.4.1}$$

A basis of the six-dimensional $\tau_1^{(6)}$ representation is

$$\mathcal{T}_{i=1,\cdots,6}^{\tau_1^{(6)}} = \frac{(-i)^{\delta_{\nu 4}}}{\sqrt{2}}(\mathcal{T}_{\mu\nu} + \mathcal{T}_{\mu\nu}),\ 1 \le \mu \le \nu \le 4. \tag{5.4.2}$$

Since we only consider the operator $\mathcal{T}_{4i}$ in this dissertation, a purely multiplicative renormalization procedure is involved for the T_1, T_2 and T_3 form factors and also their linear combinations such as $T_1(Q^2) + T_2(Q^2)$ as

$$\begin{aligned} T^{u,d}({\rm CI})^R &= Z_{QQ}^{\overline{\rm MS}}(\mu) T^{u,d}({\rm CI}), \\ T^{u,d,s}({\rm DI})^R &= Z_{QQ}^{\overline{\rm MS}}(\mu) T^{u,d,s}({\rm DI}) + \delta Z_{QQ}^{\overline{\rm MS}}(\mu) \sum_{q=u,d,s} [T^q({\rm CI}) + T^q({\rm DI})] \\ &\quad + Z_{QG}^{\overline{\rm MS}}(\mu) T^g({\rm DI}), \\ T^g({\rm DI})^R &= Z_{GQ}^{\overline{\rm MS}}(\mu) \sum_{q=u,d,s} [T^q({\rm CI}) + T^q({\rm DI})] + Z_{GG}^{\overline{\rm MS}} T^g({\rm DI}), \end{aligned} \tag{5.4.3}$$

in which $T^{q/g}({\rm CI})$ and $T^{q/g}({\rm DI})$ are the CI and DI bare form factors under the lattice regularization, respectively. In order to calculate the renormalization constants $Z^{\overline{\rm MS}}$ at $\overline{\rm MS}$ scale μ, we follow the nonperturbative renormalization procedure described in [56]. First, we carry out the RI/MOM nonperturbative renormalization at scale $\mu_R^2 = p^2$ for several p^2 with several quark masses at different momentum and then extrapolate the results to the massless limit. Then, we match from RI/MOM to $\overline{\rm MS}$ using the matching coefficients from perturbative calculations. The matching coefficients from $\overline{\rm MS}$ scheme at scale μ to RI/MOM scheme at scale μ_R are

$$\begin{aligned} &\begin{pmatrix} Z_{QQ}^{\overline{\rm MS}}(\mu) + N_f \delta Z_{QQ}^{\overline{\rm MS}}(\mu) & N_f Z_{QG}^{\overline{\rm MS}}(\mu) \\ Z_{GQ}^{\overline{\rm MS}}(\mu) & Z_{GG}^{\overline{\rm MS}}(\mu) \end{pmatrix} = \left\{ \left[\begin{pmatrix} Z_{QQ}(\mu_R) + N_f \delta Z_{QQ} & N_f Z_{QG}(\mu_R) \\ Z_{GQ}(\mu_R) & Z_{GG}(\mu_R) \end{pmatrix} \right. \right. \\ &\left. \left. \begin{pmatrix} R_{QQ}(\frac{\mu}{\mu_R}) + \mathcal{O}(N_f \alpha_s^2) & N_f R_{QG}(\frac{\mu}{\mu_R}) \\ R_{GQ}(\frac{\mu}{\mu_R}) & R_{GG}(\frac{\mu}{\mu_R}) \end{pmatrix} \right] \right|_{a^2 \mu_R^2 \to 0} \Bigg\}^{-1} \equiv \begin{pmatrix} C_{QQ} & C_{QG} \\ C_{GQ} & C_{GG} \end{pmatrix}^{-1}, \end{aligned} \tag{5.4.4}$$

with

$$
\begin{aligned}
C_{QQ} &= \left[(Z_{QQ}R_{QQ}) + N_f\left(\delta Z_{QQ}R_{QQ} + Z_{QG}R_{GQ}\right)\right](\mu_R, \frac{\mu}{\mu_R})\Big|_{a^2\mu_R^2\to 0}, \\
C_{QG} &= \left[N_f\left((Z_{QQ} + N_f\delta R_{QQ})R_{QG} + Z_{QG}R_{GG}\right)\right](\mu_R, \frac{\mu}{\mu_R})\Big|_{a^2\mu_R^2\to 0}, \\
C_{GQ} &= \left[Z_{GQ}R_{QQ} + Z_{GG}R_{GQ}\right](\mu_R, \frac{\mu}{\mu_R})\Big|_{a^2\mu_R^2\to 0}, \\
C_{GG} &= \left[N_f Z_{GQ}R_{QG} + Z_{GG}R_{GG}\right](\mu_R, \frac{\mu}{\mu_R})\Big|_{a^2\mu_R^2\to 0},
\end{aligned}
\tag{5.4.5}
$$

and $Z_{QQ}^{\overline{\rm MS}}(\mu) = \Big[(Z_{QQ}R_{QQ})\,(\mu_R, \frac{\mu}{\mu_R})|_{a^2\mu_R^2\to 0}\Big]^{-1}$. The matching coefficient Rs are the perturbative matching coefficients from the RI scheme at scale μ_R to the $\overline{\rm MS}$ scheme at scale μ as

$$
R_{QQ}(\frac{\mu}{\mu_R}) = 1 + \frac{g^2}{16\pi^2}C_F[\frac{8}{3}\log(\mu^2/\mu_R^2) + \frac{31}{9}] + \mathcal{O}(\alpha_s^2), \tag{5.4.6}
$$

with $\sum_a (T^a)^2_{bb} = (N_c^2-1)/(2N_c) = C_F$ the quadratic Casimir invariant of $SU(N_c)$, with $N_c = 3$. This matching coefficients have been obtained at 3-loop level [103] and others at 1-loop level [104] as

$$
\begin{aligned}
R_{QG} &= -\frac{g^2}{16\pi^2}[\frac{2}{3}\log(\mu^2/\mu_R^2) + \frac{4}{9}] + \mathcal{O}(\alpha_s^2), \\
R_{GQ} &= -\frac{g^2 C_F}{16\pi^2}[\frac{8}{3}\log(\mu^2/\mu_R^2) + \frac{22}{9}] + \mathcal{O}(\alpha_s^2), \\
R_{GG} &= 1 + \frac{g^2 N_f}{16\pi^2}[\frac{2}{3}\log(\mu^2/\mu_R^2) + \frac{10}{9}] - \frac{g^2 N_c}{16\pi^2}\frac{5}{12} + \mathcal{O}(\alpha_s^2).
\end{aligned}
\tag{5.4.7}
$$

The RI/MOM renormalization constants Zs for the quark external legs are defined [103] as

$$
Z_{QQ}(\mu_R) = \frac{V{\rm Tr}\left[\Gamma^q_{\mu\nu}\bar{S}_q^{-1}(p)\left\langle\sum_w \gamma_5 S_q^\dagger(p,w)\gamma_5\frac{1}{2}(\gamma_\mu\overleftrightarrow{D}_\nu + \gamma_\nu\overleftrightarrow{D}_\mu)S_q(p,w)\right\rangle\bar{S}_q^{-1}(p)\right]}{\left[-i\Gamma^q_{\mu\nu}(\frac{1}{2}(\gamma_\mu\tilde{p}_\nu + \gamma_\nu\tilde{p}_\mu) - \frac{1}{4}\not{\tilde{p}})\right]Z_q}\Bigg|_{p^2=\mu_R^2}, \tag{5.4.8}
$$

$$
\delta Z_{QQ}(\mu_R) = \frac{V{\rm Tr}\left[\Gamma^q_{\mu\mu}\bar{S}_q^{-1}(p)\left\langle\mathcal{T}^q_{\mu\nu}S_q(p)\right\rangle\bar{S}_q^{-1}(p)\right]}{\left[-i\Gamma^q_{\mu\nu}(\frac{1}{2}(\gamma_\mu\tilde{p}_\mu + \gamma_\mu\tilde{p}_\nu) - \frac{1}{4}\not{\tilde{p}})\right]Z_q}\Bigg|_{p^2=\mu_R^2}, \tag{5.4.9}
$$

$$
Z_{GQ}(\mu_R) = \frac{V{\rm Tr}\left[\Gamma^q_{\mu\nu}\bar{S}_q^{-1}(p)\left\langle\mathcal{T}^g_{\mu\nu}S_q(p)\right\rangle\bar{S}_q^{-1}(p)\right]}{\left[-i\Gamma^q_{\mu\nu}(\frac{1}{2}(\gamma_\mu\tilde{p}_\nu + \gamma_\nu\tilde{p}_\mu) - \frac{1}{4}\not{\tilde{p}})\right]Z_q}\Bigg|_{p^2=\mu_R^2}, \tag{5.4.10}
$$

in which index μ is not summed while results from different μ are averaged, V is the lattice volume, p is the momentum of the external quark or gluon state, $\tilde{p}_\mu = \sin(p_\mu)$ is the lattice momentum, $\bar{S}_q(p) = \langle S_q(p)\rangle = \langle\sum_x e^{ipx}S_q(p,x)\rangle$ is the quark propagator in momentum space with $S_q(p,x) = \sum_y e^{-ipy}\psi(x)\bar{\psi}(y)$, Z_q is the quark normalization

constant defined from the axial-vector vertex correction and Ward identity [105] and the quark vertex operator is

$$\Gamma^q_{\mu\nu} = i\gamma_\mu \tilde{p}_\nu + i\gamma_\nu \tilde{p}_\mu - i\frac{\tilde{p}_\mu \tilde{p}_\nu}{\tilde{p}^2}\tilde{\not{p}}, \tag{5.4.11}$$

as suggested by Ref. [106]. Inspired by Ref. [104, 90], the gluon external legs are defined as

$$\begin{aligned} Z_{QG}(\mu_R) &= \xi^{-1} Z_b(\mu_R, \overline{T}^q) - (\xi^{-1} - 1) Z_a(\mu_R, \overline{T}^q), \\ Z_{GG}(\mu_R) &= \xi^{-1} Z_b(\mu_R, \overline{T}^g) - (\xi^{-1} - 1) Z_a(\mu_R, \overline{T}^g), \end{aligned} \tag{5.4.12}$$

with $\xi \equiv \frac{\sum_\mu p_\mu^4}{(\sum_\mu p_\mu^2)^2}$. Z_a is

$$Z_a(\mu_R, \overline{T}) = \frac{p^2 \langle (k_\mu \mathcal{T}_{\mu\nu} q_\nu) \mathrm{Tr}[A_\rho(p) A_\tau(-p) \Gamma_{\rho\tau}] \rangle}{2k^2 q^2 \langle \mathrm{Tr}[A_\rho(p) A_\tau(-p) \Gamma_{\rho\tau}] \rangle}, \tag{5.4.13}$$

which is calculated under the conditions $p^2 = \mu_R^2$, $k + q = p$, $k \cdot q = 0$ and $\Gamma_{\rho\tau} = \delta_{\rho\tau} - \frac{k_\rho k_\tau}{k^2} - \frac{q_\rho q_\tau}{q^2}$ with the repeated indices summed here. And Z_b is

$$Z_b(\mu_R, \overline{T}) = \frac{\langle (p_\mu \overline{T}_{\mu\nu} p_\nu - l_\mu \overline{T}_{\mu\nu} l_\nu) \mathrm{Tr}[A_\rho(p) A_\tau(-p) \tilde{\Gamma}_{\rho\tau}] \rangle}{2p^2 \langle \mathrm{Tr}[A_\rho(p) A_\tau(-p) \tilde{\Gamma}_{\rho\tau}] \rangle}, \tag{5.4.14}$$

which is calculated under the conditions $p^2 = \mu_R^2$, $l^2 = p^2$, $l \cdot p = 0$ and $\tilde{\Gamma}_{\rho\tau} = \delta_{\rho\tau} - \frac{p_\rho p_\tau}{p^2} - \frac{l_\rho l_\tau}{l^2}$ with the repeated indices also summed here.

Table 5.1: The non-perturbative renormalization constants of τ_1^3 representation on 32ID lattice.

Lattice	Z_{QQ}	δZ_{QQ}	Z_{QG}	Z_{GQ}	Z_{GG}
32ID	1.25(0)(2)	0.018(2)(2)	0.017(17)	0.57(3)(6)	1.29(5)(9)

Ref. [56] has done a complete calculation of the non-perturbative renormalization constants on the 32ID lattice of the τ_1^3 representation which are shown in Table. 5.1. The non-perturbative renormalization constants of the τ_1^6 representation are also calculated which are consistent with those values of the τ_1^3 representation under current statistics. Thus we use the values in Table. 5.1 to renormalise the results in this dissertation.

As we are using local current operators, we need to normalize the momentum and angular momentum fractions with the two sum rules in Eq. (5.3.5). A way of normalizing the momentum and angular momentum fractions is proposed in Ref. [87], in which the normalization constants for quarks and glue Z_q^L and Z_g^L separately are defined as

$$\begin{aligned} Z_q^L \langle x \rangle^{q,L} + Z_g^L \langle x \rangle^{g,L} &= 1, \\ Z_q^L J^{q,L} + Z_g^L J^{g,L} &= \frac{1}{2}, \end{aligned} \tag{5.4.15}$$

and the normalized quantities are

$$\begin{aligned} \langle x\rangle^q = Z_q^L \langle x\rangle^{q,L},\ \langle x\rangle^g = Z_g^L \langle x\rangle^{g,L}, \\ J^q = Z_q^L J^{q,L},\ J^g = Z_g^L J^{g,L}. \end{aligned} \tag{5.4.16}$$

By solving Eq. (5.4.15) we get Z_q^L and Z_g^L as

$$\begin{aligned} Z_q^L &= \frac{-2J^{g,L} + \langle x\rangle^{g,L}}{2J^{q,L}\langle x\rangle^{g,L} - 2J^{g,L}\langle x\rangle^{q,L}} = \frac{-T_2^g}{T_2^q T_1^g - T_2^g T_1^q}, \\ Z_g^L &= \frac{2J^{q,L} - \langle x\rangle^{q,L}}{2J^{q,L}\langle x\rangle^{g,L} - 2J^{g,L}\langle x\rangle^{q,L}} = \frac{T_2^q}{T_2^q T_1^g - T_2^g T_1^q}, \end{aligned} \tag{5.4.17}$$

in which $T_1^{q,g}$ and $T_2^{q,g}$ are the nucleon form factor from the local current after renormalization. Whereas, the T_2 form factors, which are required in the numerator of the normalization, have almost no signal under our current statistics. Given the current situation, we assume $A \equiv Z_q^L = Z_g^L$ and calculate A from the momentum sum rule as

$$A\langle x\rangle^{q,L} + A\langle x\rangle^{g,L} = 1. \tag{5.4.18}$$

Then we will test this normalization constant A on the angular momentum fractions sum rule as

$$A\, J^{q,L} + A\, J^{g,L} \ = C\,\tfrac{1}{2}, \tag{5.4.19}$$

to check whether C is close to 1 within uncertainty.

Numerical details

We use overlap fermions on a $32^3 \times 64$ ensemble (32ID) of HYP smeared 2+1-flavor domain-wall fermion configuration with Iwasaki plus the Dislocation Suppressing Determinant Ratio (DSDR) gauge action (labeled with ID) [62] at $a = 0.143$ fm and $m_\pi = 172$ MeV. The effective quark propagator of the massive overlap fermions is the inverse of the operator $(D_c + m)$ [25, 28], where D_c is chiral, i.e., $\{D_c, \gamma_5\} = 0$ [26]. And it can be expressed in terms of the overlap Dirac operator D_{ov} as $D_c = \rho D_{ov}/(1 - D_{ov}/2)$, with $\rho = -(1/(2\kappa) - 4)$ and $\kappa = 0.2$. A multi-mass inverter is used to calculate the propagators on 200 gauge configurations with 6 valence pion masses, 173.76(17), 232.61(17), 261.34(17), 287.11(17), 325.47(17) and 391.11(17) MeV. Box-smearing [64, 65] with box half size 1.0 fm is applied to have better overlap with the nucleon ground state.

On each of configuration, three source propagators $D^{-1}(y|\mathcal{G})$ are computed with $\mathcal{G}$ the smeared Z_3-noise grid source [39] with $\{2, 2, 2, 2\}$ points in $\{x, y, z, t\}$ directions, respectively.

For the CI, we use the stochastic sandwich method [40, 1] to calculate the three-point function with low mode substitution (LMS) on source grid-source to improve signals of the nucleon. The separation of sink position x' and current position z in splitting the low and high modes for the propagator $D^{-1}(z|x')$ between the current

and sink can facilitate FFT along with LMS as described in Sec. 3.4. We generate n_f sets of high-mode propagator $D^{-1}_{H,noi}(z,\eta_j)$ defined in Eq. (3.4.7). Four source-sink separations $t' = 7, 8, 9, 10$ $(a) = 1.0, 1.14, 1.29, 1.43$ (fm) are used to control the excited-state contaminations with $n_f = 2, 3, 4, 5$, respectively.

We also use smeared Z_3-noise grids to calculate the nucleon two-point functions with the spatial center of each grid chosen randomly and repeat the calculation with 16 different source time positions on each configuration to have good statistics.

The Quark loop $L^q[4, i, t, \vec{q}; U]$ is calculated based on the point source propagators $D^{-1}(y|z)$ with $y = z \pm a_x, a_y$ or a_z. The low-mode part of this propagator is calculated exactly using the low-lying eigenvectors of the overlap Dirac operator. The high-mode part of is estimated with 8 sets of a 4-4-4-2 space-time Z_4-noise of grid with even-odd dilution [107]. Each set has different spatial center and additional time shift. The valence quark masses used in construction of quark loops vary from light quark masses to the strange quark region. The bare valence strange quark mass $m_s a = 0.08500$ is determined from the global-fit value $m_s = 101(3)(6)$ MeV at 2 GeV in $\overline{\text{MS}}$ scheme calculated in [108] and the nonperturbative mass renormalization constant [105] is $Z_m = 0.87642(77)$. The Gluon operator $L^q[4, i, t, \vec{q}; U]$ is constructed on all the current positions z to have full statistics.

The total number of propagators we generated is $3 + 14 + 16 + 8 = 41$ on each of the 200 configurations.

5.5 Results and analysis

Three-point function fit

The formula we use to fit the quark/gluon ratio R is

$$\begin{aligned} R(\mu, 4, i; t, t', \vec{p}', \vec{p}) =& A + B_1 e^{-\Delta E_{p'}(t'-\tau)} \\ &+ B_2 e^{-\Delta E_p(\tau)} + B_3 e^{-\Delta E_p(\tau) - \Delta E_{p'}(t'-\tau)}, \end{aligned} \tag{5.5.1}$$

where A is the ground state matrix element, the terms with B_1, B_3 and B_2 are the contributions from the excited-state contamination, and $\Delta E_p = E^1_p - E_p$ is the energy difference between the nucleon ground-state energy E_p and that of the first excited-state E^1_p. In order to stabilize the fit, we use the ΔE_p from the fitting of the two-point function as a prior for the three-point function fit with $\Delta E_p \sim [300, 800]$ MeV.

Connected insertions

We first present the fitting of CI of up and down quarks. Fig. 5.3 shows a sample fitting plot of the T_1 form factor on 32ID with the unitary pion mass of 174 MeV at $\vec{q} = \frac{2\pi}{L}[0, 0, 1]$. We have used the energy difference ΔE from 2pt to constrain our fits of Eq. (5.5.1) for all CI. A similar fitting is shown in Fig. 5.4 for $[T_1 + T_2]$ form factor at $Q^2 = 0.0718$ GeV^2. We have used source sink separation $t' = 7, 8, 9, 10$ for both fits and 6 points are dropped (3 points close to the source $t = 0$ and 3 points close to the sink t') for each separation. All the fits for the CI 3pt to 2pt ratios have $\chi^2/d.o.f. \sim 1.0$.

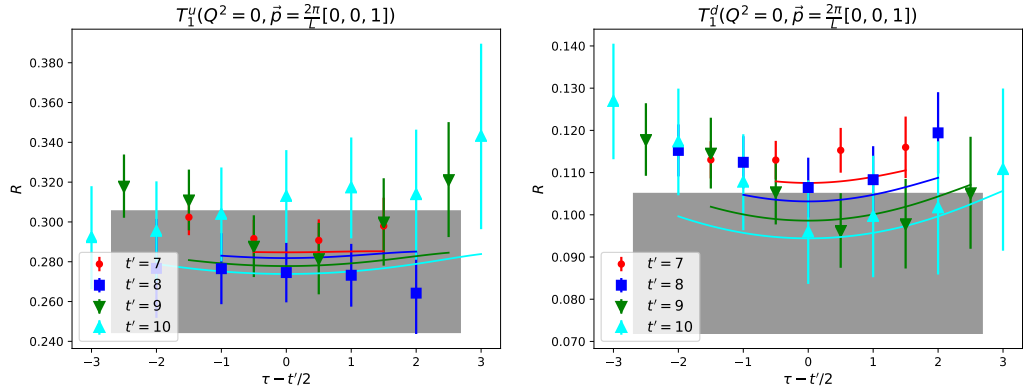

Figure 5.3: The ratio R of the CI three-point to two-point function for up (left panel) and down quark (right panel) with valence pion mass 174 MeV at $\vec{q} = \frac{2\pi}{L}[0,0,1]$. The data points correspond to different source-sink separation t' and current position τ. The bands are the fitting predictions with the gray band the ground state T_1 form factor.

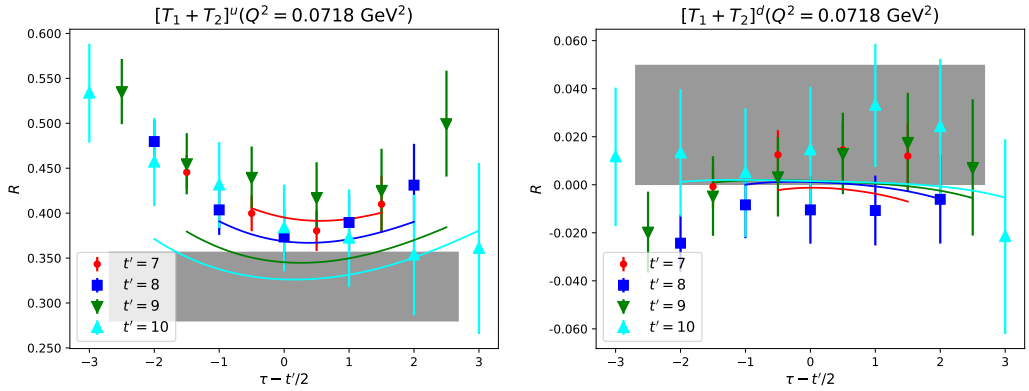

Figure 5.4: The ratio R of the CI three-point to two-point function for up (left panel) and down quark (right panel) with valence pion mass 174 MeV at $Q^2 = 0.0718$ GeV^2. The data points correspond to different source-sink separation t' and current position τ. In each plot, the bands are the fitting predictions with the gray band the ground state $[T_1 + T_2]$ form factor.

We repeat this procedure for all of the other p, the CI T_1 form factor for the up and down quarks at different p_{num}. The results are shown in Fig. 5.5 with p_{num} being the label of the lattice discrete momentum ordered according to $|\vec{p}|^2$. As shown in Eq. (5.3.22), the calculation of the T_1 form factor using operator $\mathcal{T}_{4i}$ can only be done at $\vec{p} \neq \vec{0}$. This is why we don't have $p_{\text{num}} = 0$ in Fig. 5.5 for the CI up and down quark, and also for the following similar plots for DI up/down quark, strange quark and glue. It can be seen that the results for $T_1(Q^2 = 0)$ from different p are consistent with each other within uncertainty. Thus we use a simple constant fit of the data points to give the final predictions.

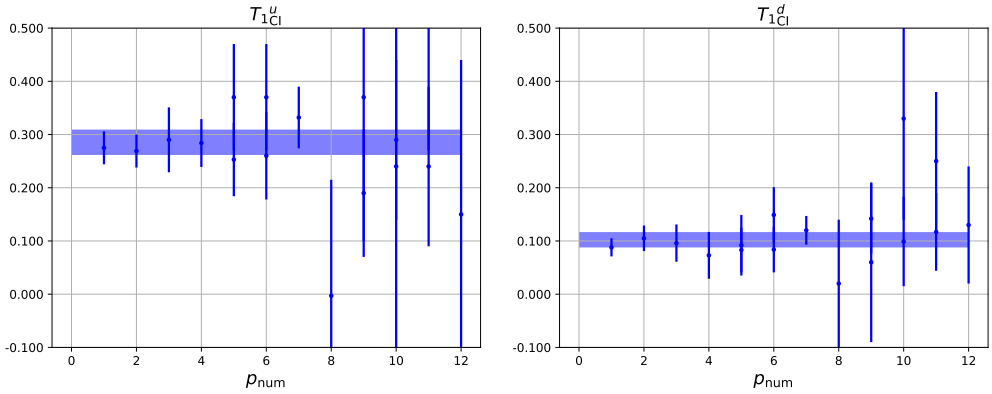

Figure 5.5: CI plots of the T_1 form factor for up (left panel) and down (right panel) quarks with p_{num} the label of the lattice discrete momentum ordered according to $\vec{p}^2$. In each plot, the band corresponds to a constant fit of the data points.

The fitting of the CI $[T_1 + T_2]$ form factor for up and down quarks is shown in Fig. 5.6. As shown in Eq. (5.3.23), calculation of the $[T_1 + T_2]$ form factor using operator $\mathcal{T}_{4i}$ can only be done at $\vec{p} \neq \vec{0}$. Thus, we use the z-expansion defined in Eq. (5.3.27) to fit the data points and extrapolate to $Q^2 = 0$ to get $[T_1 + T_2](Q^2 = 0)$ for the CI up and down quarks, and also for the following similar plots for DI up/down quark, strange quark and glue.

Quark disconnected insertions

The fittings of DI 3pt to 2pt ratios R for the T_1 form factor of up/down and strange quarks are shown in Fig. 5.7. We treat up and down quark DI contributions to be the same since we have exact isospin symmetry in the current simulation. We have also used the energy difference ΔE from 2pt to constrain our fits of Eq. (5.5.1) for all DI. The source sink separations $t' = 4, 5, 6, 7, 8, 9, 10$ are used for both fits and 4 points are dropped (2 points close to the source $t = 0$ and 2 points close to the sink t') for each separation. We have chosen the fit which starts from source sink separation $t' = 4$ instead of $t' = 7$ in the CI cases under current statistics. A similar fit is shown in Fig. 5.8 for the $[T_1 + T_2]$ form factor at $Q^2 = 0.0718$ GeV^2. All the fits have $\chi^2/d.o.f. \sim 1.0$.

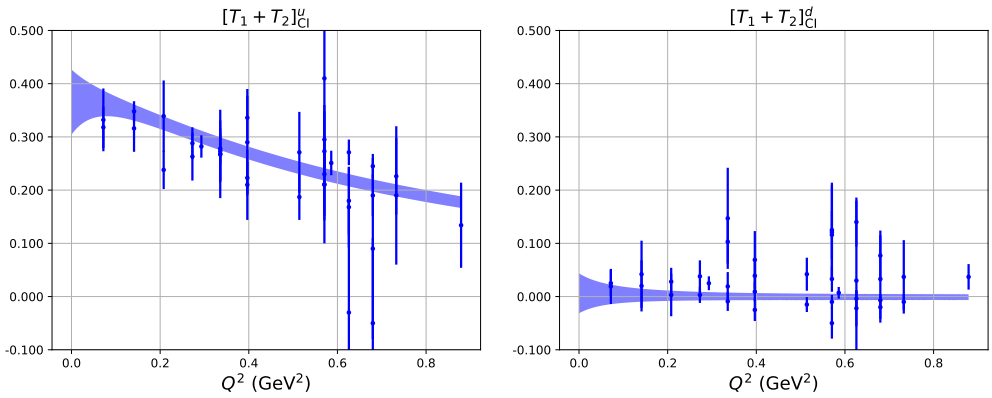

Figure 5.6: CI plots of the $[T_1 + T_2]$ form factor for up (left panel) and down (right panel) quarks as a function of Q^2. In each plot, the band corresponds to the z-expansion fit with $k_{\max} = 7$ and sum rules in Eq. (5.3.29).

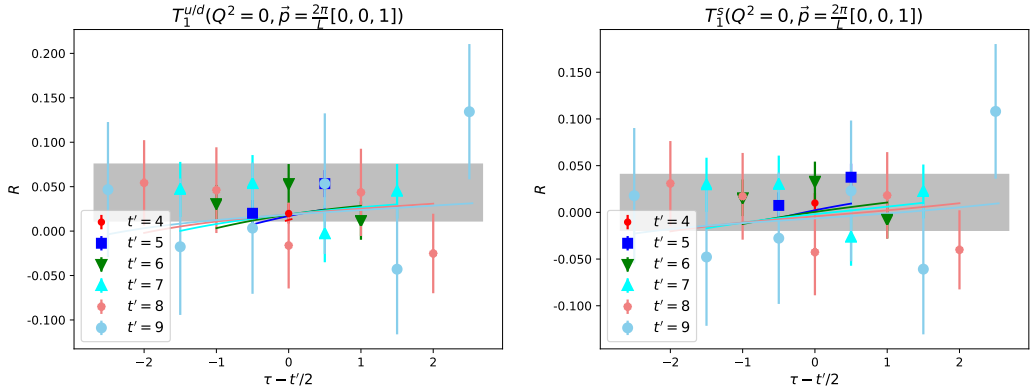

Figure 5.7: The ratio R of the DI three-point to two-point function for up/down (left panel) and strange quark (right panel) with valence pion mass 174 MeV at $\vec{q} = \frac{2\pi}{L}[0, 0, 1]$. The data points correspond to different source-sink separation t' and current position τ. In each plot, the bands are the fitting predictions with the gray band the ground state T_1 form factor.

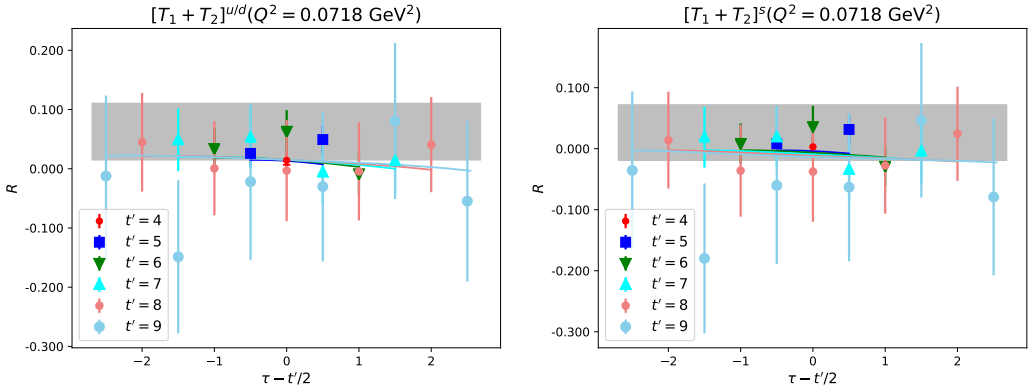

Figure 5.8: The ratio R of the DI three-point to two-point function for up/down (left panel) and strange quark (right panel) with valence pion mass 174 MeV at $Q^2 = 0.0718\ \mathrm{GeV}^2$. The data points correspond to different source-sink separation t' and current position τ. In each plot, the bands are the fitting predictions with the gray band the ground state $[T_1 + T_2]$ form factor.

We repeat this procedure for all of the other p, the DI T_1 form factor for up/down and strange quarks at different p_{num}. The results are shown in Fig. 5.5 with p_{num} being the label of lattice discrete momentum ordered according to $|\vec{p}|^2$. It can be seen that the results for $T_1(Q^2 = 0)$ from different p are consistent with each other within uncertainty. Thus we also use a simple constant fit of the data points to give the final predictions.

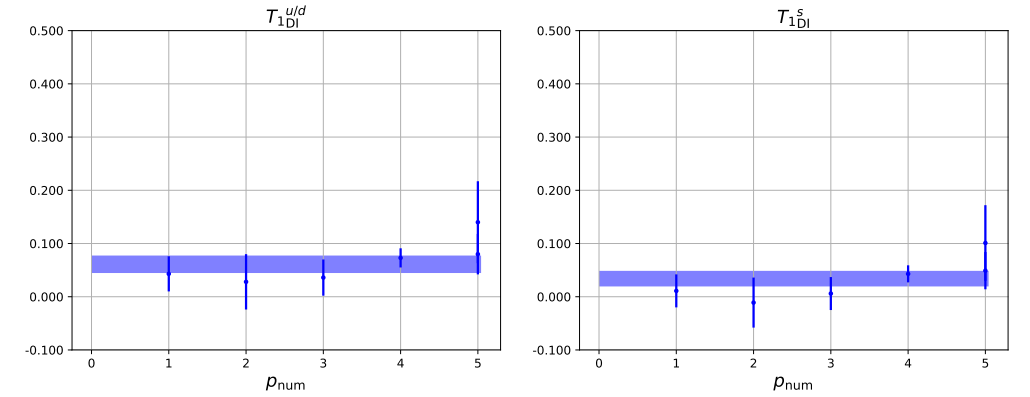

Figure 5.9: DI plots of T_1 form factor for up/down (left panel) and strange (right panel) quarks with p_{num} the label of lattice discrete momentum ordered according to $\vec{p}^2$. In each plot, the band corresponds to a constant fit of the data points.

The fitting of the DI $[T_1 + T_2]$ form factor for up/down and strange quarks is shown in Fig. 5.6. We used the z-expansion defined in Eq. (5.3.27) to fit the data points at $k_{\max} = 2$ without sum rules in Eq. (5.3.29) under current statistics. With such a fit, we can extrapolate to get $[T_1 + T_2](0)$ for up/down and strange quarks.

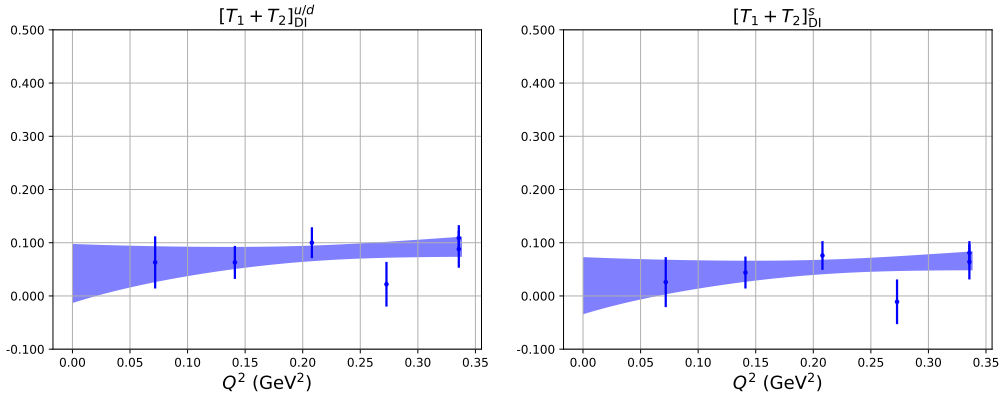

Figure 5.10: DI plots of $[T_1 + T_2]$ form factor for up/down (left panel) and strange (right panel) quarks as a function of Q^2. In each plot, the band corresponds to the z-expansion fit with $k_{\rm max} = 2$.

Glue disconnected insertions

The fittings of DI 3pt to 2pt ratios R for the T_1 and $[T_1 + T_2]$ form factors for the glue are shown in Fig. 5.7. Since the glue form factors have almost no signal at pion mass 174 MeV, we have chosen to show the plots at pion mass 391 MeV. We have also used the energy difference ΔE from 2pt to constrain our fits of Eq. (5.5.1) for all DI. We have used source sink separations $t' = 4, 5, 6, 7, 8, 9$ for both fits and dropped 4 points (2 points close to the source $t = 0$ and 2 points close to the sink t') for each separation.

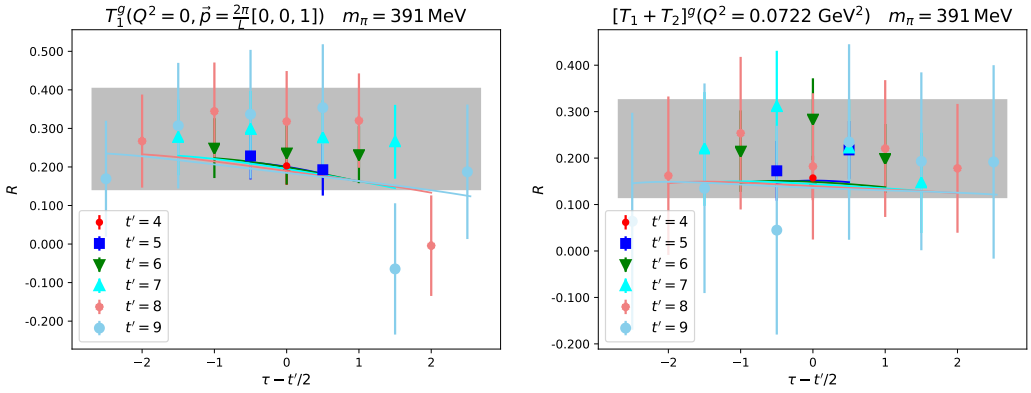

Figure 5.11: The ratio R of the DI three-point to two-point function of glue T_1 (left panel) and $[T_1 + T_2]$ (right panel) form factor with valence pion mass 391 MeV at $Q^2 = 0.0722$ GeV^2. The data points correspond to different source-sink separation t' and current position τ. In each plot, the bands are the fitting predictions with the gray band the ground state form factors.

After repeating this procedure for all other p, the DI T_1 and $[T_1 + T_2]$ form factor for the glue are shown in Fig. 5.10. We use a simple constant fit of the T_1 form factor

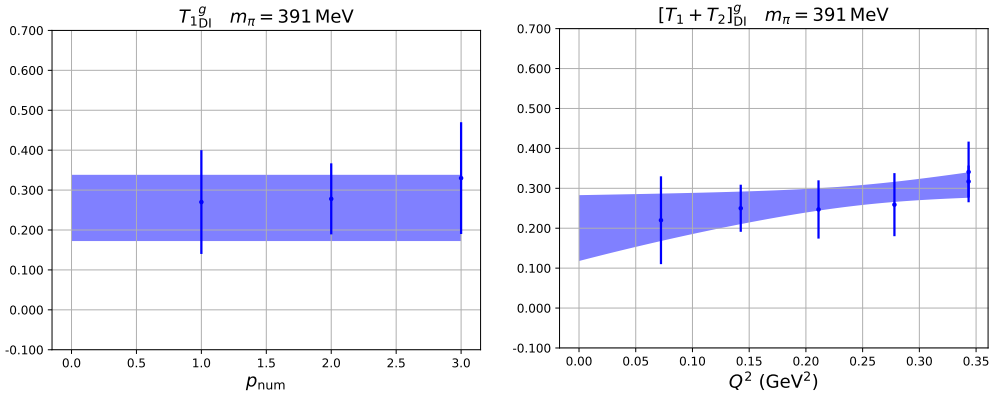

Figure 5.12: DI plots of the T_1 (left panel) and $[T_1+T_2]$ (right panel) form factors for the glue. The band in the left panel corresponds to a constant fit of the data points. The band in the right panel corresponds to the z-expansion fit with $k_{\max} = 2$.

data points to give the final predictions. z-expansion fitting of the DI $[T_1+T_2]$ glue form factor at $k_{\max} = 2$ without sum rules under current statistics is also shown in Fig. 5.10. With such a fit, we can extrapolate to get $[T_1+T_2](0)$ for up/down and strange quarks.

Final results

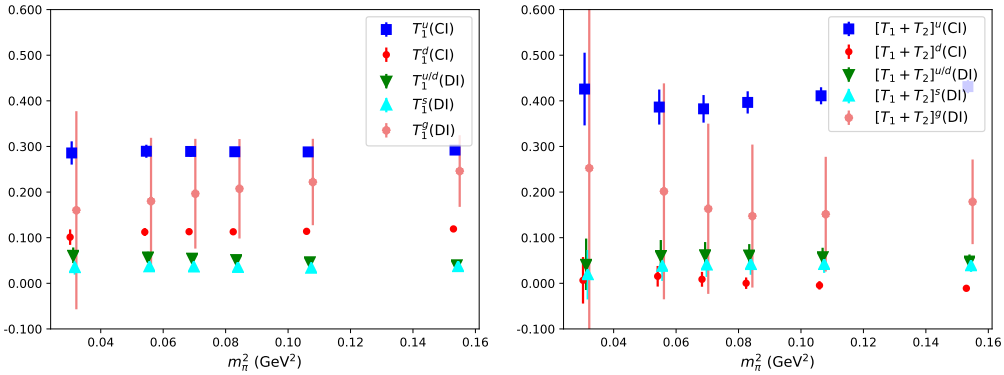

Figure 5.13: Plots of the $T_1(Q^2 = 0)$ (left panel) and $[T_1+T_2](Q^2 = 0)$ (right panel) form factors at different valence pion masses without renormalization and normalization. Different colors correspond to up quark CI, down quark CI, up/down quark DI, strange quark DI and glue DI.

Repeating the analysis for different valence pion masses, we gather the results of $T_1(Q^2 = 0)$ and $[T_1+T_2](Q^2 = 0)$ form factors at different valence pion masses without renormalization and normalization in Fig. 5.13. We see clear signals for up quark CI and down quark CI.

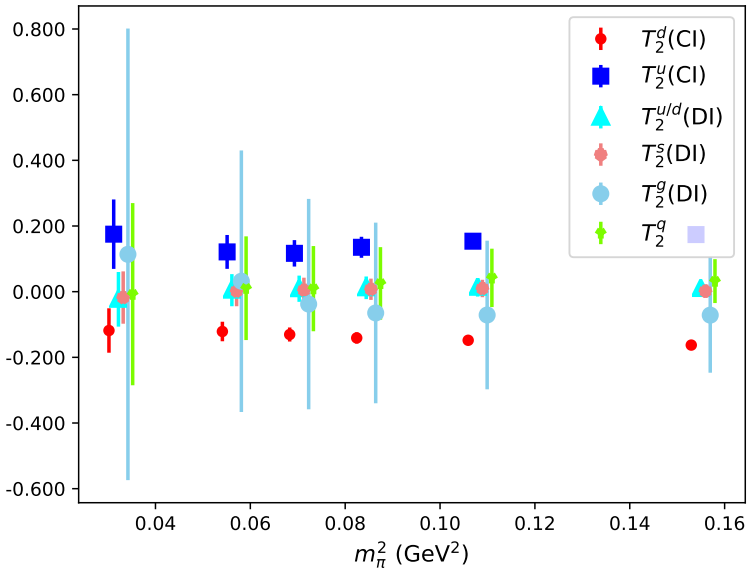

Figure 5.14: Plot of the $T_2(Q^2 = 0)$ form factor at different valence pion masses after renormalization without normalization. Different colors correspond to up quark CI and DI, down quark CI and DI and glue DI.

Since the normalization condition Eq. (5.4.15) is proportional to the T_2 form factor, we have shown the T_2 form factor after renormalization in Fig. 5.14. It can been seen that T_2^q and T_2^g have almost no signals under current statistics and so likewise for the normalization constants Z_q^L and Z_g^L. Thus we use the normalization constant A defined in Eq. (5.4.18) to normalize the T_1 form factor and test it on the $[T_1 + T_2]$ form factor with Eq. (5.4.19).

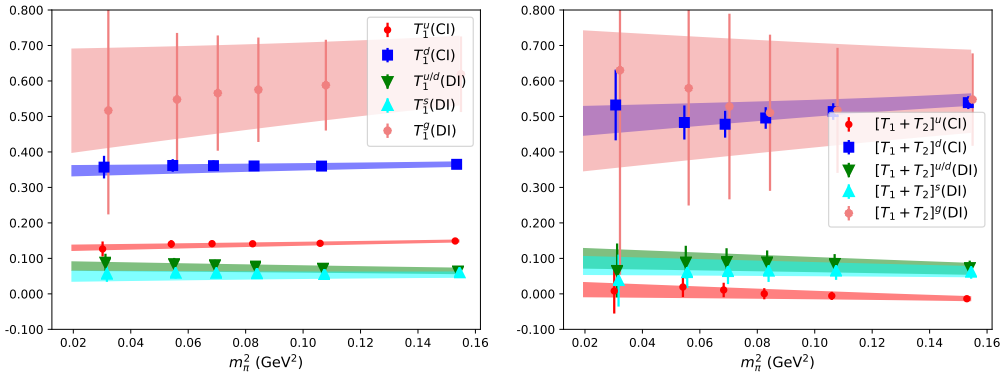

Figure 5.15: Plots of momentum fractions $\langle x \rangle$ (left panel) and angular momentum fractions J (right panel) at different valence pion masses after renormalization without normalization. Different colors correspond to up quark CI and DI, down quark CI and DI, strange DI and glue DI. The band is a linear fit of the data points to extrapolate to the physical pion mass.

The extrapolated results to the physical point with a simple linear fit under current statistics are shown in Fig. 5.15. The results at the physical pion mass are gathered in Table. 5.2 after renormalization without normalization. Thus we have the normalization constant $A = 0.81(11)$ for the T_1 form factor and test A on the $[T_1+T_2]$ form factor to get $C = 1.08(25)$ which is consistent with 1 within error. This justifies using the normalization constant A for the T_1 form factor on the $[T_1 + T_2]$ form factor with current statistics.

Table 5.2: Renormalized values of T_1, $[T_1 + T_2]$ and T_2 form factors extrapolated to the physical pion mass without normalization. Sum_q in the table is the sum of all the quark CI and DI contributions. Sum in the table is the sum of all the quark and glue contributions.

	u(CI)	d(CI)	u/d(DI)	s(DI)	glue	Sum_q	Sum
T_1	0.347(16)	0.1298(91)	0.078(14)	0.050(16)	0.54(15)	0.683(46)	1.23(17)
$[T_1 + T_2]$	0.488(42)	0.012(22)	0.100(29)	0.080(27)	0.54(20)	0.78(10)	1.32(25)
T_2	0.141(44)	-0.118(24)	0.022(32)	0.030(30)	-0.0003(2479)	0.10(11)	0.10(31)

The final renormalized and normalized momentum fractions $\langle x \rangle$ and angular momentum fractions $2J$ are listed in Table. 5.3. We have also listed the quark spin g_A^0 from Ref. [1] at $\overline{\text{MS}}(\mu = 2\text{ GeV})$. The orbital angular momentum fractions $2L$ are calculated with $2L = 2J - g_A^0$. Our predictions of the momentum fractions $\langle x \rangle^R$ (listed in Table. 5.4) are consistent with the phenomenological global fits at $\overline{\text{MS}}(\mu = 2\text{ GeV})$ such as CT14 [2] values (also listed in the same table) which are also consistent with other global fits results [109, 110, 111, 112, 113].

Table 5.3: Renormalized and normalized values of momentum fractions $\langle x \rangle$ and angular momentum fractions $2J$ at $\overline{\text{MS}}(\mu = 2\text{ GeV})$. The quark spin g_A^0 is from Ref. [1] at $\overline{\text{MS}}(\mu = 2\text{ GeV})$. The orbital angular momentum fractions $2L$ are calculated with $2L = 2J - g_A^0$. Sum in the table is the sum of all the contributions.

	u(CI)	d(CI)	$[u+d]$(CI)	u/d(DI)	s(DI)	glue	Sum
$\langle x \rangle$	0.283(39)	0.106(16)	0.388(54)	0.0638(89)	0.041(11)	0.443(61)	1.0
$2J$	0.397(62)	0.010(18)	0.407(67)	0.082(26)	0.065(24)	0.44(17)	1.08(25)
g_A^0	0.917(34)	-0.337(20)	0.580(39)	-0.070(12)	-0.035(9)	–	0.405(44)
$2L$	-0.520(71)	0.347(27)	-0.173(77)	0.152(29)	0.100(25)	–	0.23(13)

Table 5.4: Renormalized and normalized values of momentum fractions $\langle x \rangle$ at $\overline{\text{MS}}(\mu = 2\text{ GeV})$ compares with the CT14 [2] values. And the angular momentum fractions $2J$ at $\overline{\text{MS}}(\mu = 2\text{ GeV})$.

	u	d	$[u-d]$	s	glue
$\langle x \rangle$	0.346(42)	0.170(20)	0.177(26)	0.041(11)	0.443(61)
$\langle x \rangle_{\text{CT14}}$	0.348(5)	0.190(5)	0.158(6)	0.035(9)	0.416(9)
$2J$	0.479(76)	0.091(34)	0.387(63)	0.065(24)	0.44(17)

5.6 Conclusion and future work

In summary, we have carried out a complete calculation of proton momentum and angular momentum fractions at several overlap valence pion masses on a $32^3 \times 64$ domain wall lattice with overlap fermions. The energy-momentum tensor three-point function calculations include both the connected insertion (CI) for up and down quarks and disconnected insertion (DI) for up/down quark, strange quark and glue. We have used complex Z_3 grid sources to increase signals of the nucleon correlation functions and Z_4 noise to estimate the quark loops. We have also used FFT on CI three-point functions along with low mode substitution (LMS) on both the source and sink nucleon. With the non-perturbative renormalization and normalization using momentum and angular momentum sum rules, we find the momentum fractions and angular momentum fractions listed in Table. 5.3 at $\overline{\text{MS}}(\mu = 2 \text{ GeV})$. We have seen clear signals for up and down quark CI, whereas the up/down quark, strange quark and glue DI need improvement through cluster-decomposition error reduction (CDER) [114, 90]. With such an improvement, we will have clear signals for the T_2 form factor which should be able to stabilize normalizations. Finally, this work should be extended to include other lattices with different volume and lattice spacing to control systematic errors from finite volume and lattice spacing.

Chapter 6 Summary and outlook

As an *ab initio* calculation, Lattice Quantum Chromodynamics (QCD) provides the possibility to study hadron structures from first principles and make predictions of the less-known quantities. From this perspective, this dissertation first focuses on a precise calculation of the pion form factor using overlap fermions on six ensembles of 2+1-flavor domain-wall configurations with pion masses varying from 137 to 339 MeV. Taking advantage of the fast Fourier transform (FFT) and other techniques to access many combinations of source and sink momenta, we find the pion mean square charge radius to be $\langle r_\pi^2 \rangle = 0.433(9)(13)$ fm^2, which agrees well with the experimental result, which includes the systematic uncertainties from chiral extrapolation, lattice spacing and finite volume dependence. We also find that $\langle r_\pi^2 \rangle$ depends on both the valence and sea quark masses strongly and predict the pion form factor up to $Q^2 = 1.0$ GeV^2 which agrees with experiments very well.

Then we use the nucleon matrix element of the traceless, symmetric energy-momentum tensor (EMT) to calculate the momentum and angular momentum fractions of up, down, strange quarks and glue inside the nucleon. Since the EMT of each parton species are not separately conserved, we summarized their final angular momentum fractions by considering mixing and non-perturbative renormalization at $\overline{\text{MS}}(\mu = 2$ GeV) and use the momentum and angular momentum sum rules to normalize them. In order to improve the signals for the nucleon correlation functions with source momenta, we developed new contractions for the grid sources to have better statistics. Moreover, we have also developed the usage of FFT on CI three-point functions along with low-mode substitution (LMS) on both the source and sink nucleon. With these improvements, we report the renormalized momentum fractions for the quarks and glue to be 0.557(61) and 0.443(61), respectively, and the renormalized total angular momentum fractions for quarks and glue to be 0.320(60) and 0.220(85), respectively (the sum is to be compared to 1/2).

However, there are still much more which could be done. As the largest systematic uncertainties come from excited-state fitting, larger separations at good statistics are needed to improve the predictions of the pion form factor calculation. Also, the signal to noise ratio at near physical pion masses is much larger than the fitted band, so increasing statistics here would give more reliable results. Besides more precise predictions under $Q^2 = 1$ GeV^2, we could also move our scope to $Q^2 \sim 10$ GeV^2 which is of great interest for experiments and theories. This could be done by using momentum smearing on the source side along with all the techniques used in this dissertation to have precise predictions from low momentum transfer to the perturbative region.

Due to the lack of cluster-decomposition error reduction (CDER) for disconnected insertions, the current calculation of proton momentum and angular momentum fractions may suffer from large systematic errors from excited-state contaminations and a normalization issue which need to be solved in future calculations. Also, the current non-perturbative renormalization procedure has large systematic uncertainties

which need to be improved for a more precise calculation. Then we can proceed to the calculations on more ensembles with different pion masses, lattice spacings and volumes to have a reliable extrapolation to the physical limit.

Bibliography

[1] Jian Liang, Yi-Bo Yang, Terrence Draper, Ming Gong, and Keh-Fei Liu. Quark spins and Anomalous Ward Identity. *Phys. Rev. D*, 98(7):074505, 2018.

[2] Sayipjamal Dulat, Tie-Jiun Hou, Jun Gao, Marco Guzzi, Joey Huston, Pavel Nadolsky, Jon Pumplin, Carl Schmidt, Daniel Stump, and C.P. Yuan. New parton distribution functions from a global analysis of quantum chromodynamics. *Phys. Rev. D*, 93(3):033006, 2016.

[3] S.R. Amendolia et al. A Measurement of the Space - Like Pion Electromagnetic Form-Factor. *Nucl. Phys. B*, 277:168, 1986.

[4] G.M. Huber et al. Charged pion form-factor between Q**2 = 0.60-GeV**2 and 2.45-GeV**2. II. Determination of, and results for, the pion form-factor. *Phys. Rev. C*, 78:045203, 2008.

[5] H.P. Blok et al. Charged pion form factor between Q^2=0.60 and 2.45 GeV^2. I. Measurements of the cross section for the ^{1}H$(e, e'\pi^+)n$ reaction. *Phys. Rev. C*, 78:045202, 2008.

[6] T. Horn et al. Scaling study of the pion electroproduction cross sections and the pion form factor. *Phys. Rev. C*, 78:058201, 2008.

[7] T. Horn et al. Determination of the Charged Pion Form Factor at Q**2 = 1.60 and 2.45-(GeV/c)**2. *Phys. Rev. Lett.*, 97:192001, 2006.

[8] J. Volmer et al. Measurement of the Charged Pion Electromagnetic Form-Factor. *Phys. Rev. Lett.*, 86:1713–1716, 2001.

[9] D. Brmmel et al. The Pion form-factor from lattice QCD with two dynamical flavours. *Eur. Phys. J. C*, 51:335–345, 2007.

[10] R. Frezzotti, V. Lubicz, and S. Simula. Electromagnetic form factor of the pion from twisted-mass lattice QCD at N(f) = 2. *Phys. Rev. D*, 79:074506, 2009.

[11] S. Aoki et al. Pion form factors from two-flavor lattice QCD with exact chiral symmetry. *Phys. Rev. D*, 80:034508, 2009.

[12] Bastian B. Brandt, Andreas Jttner, and Hartmut Wittig. The pion vector form factor from lattice QCD and NNLO chiral perturbation theory. *JHEP*, 11:034, 2013.

[13] C. Alexandrou et al. Pion vector form factor from lattice QCD at the physical point. *Phys. Rev. D*, 97(1):014508, 2018.

[14] H. Fukaya, S. Aoki, S. Hashimoto, T. Kaneko, H. Matsufuru, and J. Noaki. Computation of the electromagnetic pion form factor from lattice QCD in the ϵ regime. *Phys. Rev. D*, 90(3):034506, 2014.

[15] S. Aoki, G. Cossu, X. Feng, S. Hashimoto, T. Kaneko, J. Noaki, and T. Onogi. Light meson electromagnetic form factors from three-flavor lattice QCD with exact chiral symmetry. *Phys. Rev. D*, 93(3):034504, 2016.

[16] Xu Feng, Yang Fu, and Lu-Chang Jin. Lattice QCD calculation of the pion charge radius using a model-independent method. *Phys. Rev. D*, 101(5):051502, 2020.

[17] J. Koponen, F. Bursa, C.T.H. Davies, R.J. Dowdall, and G.P. Lepage. Size of the pion from full lattice QCD with physical u , d , s and c quarks. *Phys. Rev. D*, 93(5):054503, 2016.

[18] M. Tanabashi et al. Review of Particle Physics. *Phys. Rev. D*, 98(3):030001, 2018.

[19] J. E. Campbell. On a Law of Combination of Operators (Second Paper). *Proceedings of the London Mathematical Society*, s1-29:1432, 1897.

[20] Henri Poincare. Sur les groupes continus. *Transactions of the Cambridge Philosophical Society*, 18:220255, 1899.

[21] K. G. Wilson. Quarks: From Paradox to Myth. *in New Phenomena in Subnuclear Physics, Plenum Press*, pages 13–32, 1977.

[22] Herbert Neuberger. More about exactly massless quarks on the lattice. *Phys. Lett.*, B427:353–355, 1998.

[23] J. van den Eshof, A. Frommer, T. Lippert, K. Schilling, and H. A. van der Vorst. Numerical methods for the QCD overlap operator. I. Sign function and error bounds. *Comput. Phys. Commun.*, 146:203–224, 2002.

[24] Martin Luscher. Exact chiral symmetry on the lattice and the Ginsparg-Wilson relation. *Phys. Lett.*, B428:342–345, 1998.

[25] Ting-Wai Chiu. GW fermion propagators and chiral condensate. *Phys. Rev.*, D60:034503, 1999.

[26] Ting-Wai Chiu and Sergei V. Zenkin. On solutions of the Ginsparg-Wilson relation. *Phys. Rev.*, D59:074501, 1999.

[27] S. J. Dong, J. F. Lagae, and K. F. Liu. Pi N sigma term, anti-s s in nucleon, and scalar form-factor: A Lattice study. *Phys. Rev.*, D54:5496–5500, 1996.

[28] Keh-Fei Liu. Heavy and light quarks with lattice chiral fermions. *Int. J. Mod. Phys.*, A20:7241–7254, 2005.

[29] A. Li et al. Overlap Valence on 2+1 Flavor Domain Wall Fermion Configurations with Deflation and Low-mode Substitution. *Phys. Rev.*, D82:114501, 2010.

[30] Robert G. Edwards, Urs M. Heller, and Rajamani Narayanan. A Study of practical implementations of the overlap Dirac operator in four-dimensions. *Nucl. Phys.*, B540:457–471, 1999.

[31] S. J. Dong, F. X. Lee, K. F. Liu, and J. B. Zhang. Chiral symmetry, quark mass, and scaling of the overlap fermions. *Phys. Rev. Lett.*, 85:5051–5054, 2000.

[32] S. Tamhankar et al. Charmonium spectrum from quenched QCD with overlap fermions. *Nucl. Phys. B Proc. Suppl.*, 140:434–436, 2005.

[33] S. Tamhankaret et al. Charmonium spectrum from quenched QCD with overlap fermions. *Phys. Lett. B*, 638:55–60, 2006.

[34] K. Rummukainen and Steven A. Gottlieb. Resonance scattering phase shifts on a nonrest frame lattice. *Nucl. Phys. B*, 450:397–436, 1995.

[35] Walter Wilcox, Terrence Draper, and Keh-Fei Liu. Chiral limit of nucleon lattice electromagnetic form-factors. *Phys. Rev. D*, 46:1109–1122, 1992.

[36] S. Gusken, U. Low, K.H. Mutter, R. Sommer, A. Patel, and K. Schilling. Nonsinglet Axial Vector Couplings of the Baryon Octet in Lattice QCD. *Phys. Lett. B*, 227:266–269, 1989.

[37] C. Best, M. Gockeler, R. Horsley, Ernst-Michael Ilgenfritz, H. Perlt, Paul E.L. Rakow, A. Schafer, G. Schierholz, A. Schiller, and S. Schramm. Pion and rho structure functions from lattice QCD. *Phys. Rev. D*, 56:2743–2754, 1997.

[38] M. Gong et al. Strangeness and charmness content of the nucleon from overlap fermions on 2+1-flavor domain-wall fermion configurations. *Phys. Rev. D*, 88:014503, 2013.

[39] Shao-Jing Dong and Keh-Fei Liu. Stochastic estimation with Z(2) noise. *Phys. Lett. B*, 328:130–136, 1994.

[40] Yi-Bo Yang, Andrei Alexandru, Terrence Draper, Ming Gong, and Keh-Fei Liu. Stochastic method with low mode substitution for nucleon isovector matrix elements. *Phys. Rev. D*, 93(3):034503, 2016.

[41] Terrence Draper, R.M. Woloshyn, Walter Wilcox, and Keh-Fei Liu. The Pion Form-factor in Lattice QCD. *Nucl. Phys. B*, 318:319–336, 1989.

[42] Claude W. Bernard, Terrence Draper, G. Hockney, A.M. Rushton, and A. Soni. Lattice Calculation of Weak Matrix Elements. *Phys. Rev. Lett.*, 55:2770, 1985.

[43] G. Martinelli and Christopher T. Sachrajda. A Lattice Study of Nucleon Structure. *Nucl. Phys. B*, 316:355–372, 1989.

[44] E.B. Dally et al. Elastic Scattering Measurement of the Negative Pion Radius. *Phys. Rev. Lett.*, 48:375–378, 1982.

[45] Ivo M. Gough Eschrich et al. Measurement of the Sigma- Charge Radius by Sigma- Electron Elastic Scattering. *Phys. Lett. B*, 522:233–239, 2001.

[46] B. Ananthanarayan, Irinel Caprini, and Diganta Das. Electromagnetic charge radius of the pion at high precision. *Phys. Rev. Lett.*, 119(13):132002, 2017.

[47] Gilberto Colangelo, Martin Hoferichter, and Peter Stoffer. Two-pion contribution to hadronic vacuum polarization. *JHEP*, 02:006, 2019.

[48] William R. Frazer and Jose R. Fulco. Effect of a Pion-Pion Scattering Resonance on Nucleon Structure. II. *Phys. Rev.*, 117:1609–1614, 1960.

[49] W.G. Holladay. Nucleon Anomalous Moments via Pion-Pion Attraction. *Phys. Rev.*, 101:1198–1201, 1956.

[50] J. Gasser and H. Leutwyler. Low-Energy Expansion of Meson Form-Factors. *Nucl. Phys. B*, 250:517–538, 1985.

[51] J. Bijnens, G. Colangelo, and P. Talavera. The Vector and scalar form-factors of the pion to two loops. *JHEP*, 05:014, 1998.

[52] G. Martinelli and Christopher T. Sachrajda. A Lattice Calculation of the Pion's Form-Factor and Structure Function. *Nucl. Phys. B*, 306:865–889, 1988.

[53] Frederic D.R. Bonnet, Robert G. Edwards, George Tamminga Fleming, Randy Lewis, and David G. Richards. Lattice computations of the pion form-factor. *Phys. Rev. D*, 72:054506, 2005.

[54] P.A. Boyle, J.M. Flynn, A. Juttner, C. Kelly, H.Pedroso de Lima, C.M. Maynard, C.T. Sachrajda, and J.M. Zanotti. The Pion's electromagnetic form-factor at small momentum transfer in full lattice QCD. *JHEP*, 07:112, 2008.

[55] Oanh Hoang Nguyen, Ken-Ichi Ishikawa, Akira Ukawa, and Naoya Ukita. Electromagnetic form factor of pion from $N_f = 2+1$ dynamical flavor QCD. *JHEP*, 04:122, 2011.

[56] Yi-Bo Yang, Jian Liang, Yu-Jiang Bi, Ying Chen, Terrence Draper, Keh-Fei Liu, and Zhaofeng Liu. Proton Mass Decomposition from the QCD Energy Momentum Tensor. *Phys. Rev. Lett.*, 121(21):212001, 2018.

[57] Raza Sabbir Sufian, Yi-Bo Yang, Andrei Alexandru, Terrence Draper, Jian Liang, and Keh-Fei Liu. Strange Quark Magnetic Moment of the Nucleon at the Physical Point. *Phys. Rev. Lett.*, 118(4):042001, 2017.

[58] Yi-Bo Yang, Raza Sabbir Sufian, Andrei Alexandru, Terrence Draper, Michael J. Glatzmaier, Keh-Fei Liu, and Yong Zhao. Glue Spin and Helicity in the Proton from Lattice QCD. *Phys. Rev. Lett.*, 118(10):102001, 2017.

[59] James W. Cooley and John W. Tukey. An algorithm for the machine calculation of complex Fourier series. *Mathematics of Computation*, 19(90):297–301, 1965.

[60] Y. Aoki et al. Continuum Limit Physics from 2+1 Flavor Domain Wall QCD. *Phys. Rev. D*, 83:074508, 2011.

[61] T. Blum et al. Domain wall QCD with physical quark masses. *Phys. Rev. D*, 93(7):074505, 2016.

[62] P.A. Boyle et al. Low energy constants of SU(2) partially quenched chiral perturbation theory from N_f=2+1 domain wall QCD. *Phys. Rev. D*, 93(5):054502, 2016.

[63] Thomas A. DeGrand and Richard D. Loft. Wave function tests for lattice QCD spectroscopy. *Comput. Phys. Commun.*, 65:84–91, 1991.

[64] C.R. Allton, Christopher T. Sachrajda, V. Lubicz, L. Maiani, and G. Martinelli. A lattice computation of the decay constant of the B meson. *Nucl. Phys. B*, 349:598–616, 1991.

[65] Jian Liang, Yi-Bo Yang, Keh-Fei Liu, Andrei Alexandru, Terrence Draper, and Raza Sabbir Sufian. Lattice Calculation of Nucleon Isovector Axial Charge with Improved Currents. *Phys. Rev. D*, 96(3):034519, 2017.

[66] Gabriel Lee, John R. Arrington, and Richard J. Hill. Extraction of the proton radius from electron-proton scattering data. *Phys. Rev. D*, 92(1):013013, 2015.

[67] M. Lujan, A. Alexandru, Y. Chen, T. Draper, W. Freeman, M. Gong, F.X. Lee, A. Li, K.F. Liu, and N. Mathur. The Δ_{mix} parameter in the overlap on domain-wall mixed action. *Phys. Rev. D*, 86:014501, 2012.

[68] G.Peter Lepage and Stanley J. Brodsky. Exclusive Processes in Quantum Chromodynamics: Evolution Equations for Hadronic Wave Functions and the Form-Factors of Mesons. *Phys. Lett. B*, 87:359–365, 1979.

[69] Glennys R. Farrar and Darrell R. Jackson. The Pion Form-Factor. *Phys. Rev. Lett.*, 43:246, 1979.

[70] Daniel Arndt and Brian C. Tiburzi. Charge radii of the meson and baryon octets in quenched and partially quenched chiral perturbation theory. *Phys. Rev. D*, 68:094501, 2003.

[71] T.B. Bunton, F.-J. Jiang, and B.C. Tiburzi. Extrapolations of Lattice Meson Form Factors. *Phys. Rev. D*, 74:034514, 2006. [Erratum: Phys.Rev.D 74, 099902 (2006)].

[72] F.-J. Jiang and B.C. Tiburzi. Flavor twisted boundary conditions, pion momentum, and the pion electromagnetic form-factor. *Phys. Lett. B*, 645:314–321, 2007.

[73] Daniel de Florian, Rodolfo Sassot, Marco Stratmann, and Werner Vogelsang. Global Analysis of Helicity Parton Densities and Their Uncertainties. *Phys. Rev. Lett.*, 101:072001, 2008.

[74] Daniel de Florian, Rodolfo Sassot, Marco Stratmann, and Werner Vogelsang. Extraction of Spin-Dependent Parton Densities and Their Uncertainties. *Phys. Rev. D*, 80:034030, 2009.

[75] Johannes Blumlein and Helmut Bottcher. QCD Analysis of Polarized Deep Inelastic Scattering Data. *Nucl. Phys. B*, 841:205–230, 2010.

[76] Elliot Leader, Aleksander V. Sidorov, and Dimiter B. Stamenov. Determination of Polarized PDFs from a QCD Analysis of Inclusive and Semi-inclusive Deep Inelastic Scattering Data. *Phys. Rev. D*, 82:114018, 2010.

[77] Richard D. Ball, Stefano Forte, Alberto Guffanti, Emanuele R. Nocera, Giovanni Ridolfi, and Juan Rojo. Unbiased determination of polarized parton distributions and their uncertainties. *Nucl. Phys. B*, 874:36–84, 2013.

[78] Alexandre Deur, Stanley J. Brodsky, and Guy F. De Tramond. The Spin Structure of the Nucleon. *Rept. Prog. Phys.*, 82(076201), 2019.

[79] E.C. Aschenauer et al. The RHIC Spin Program: Achievements and Future Opportunities. 3 2013.

[80] Pibero Djawotho. Gluon polarization and jet production at STAR. *Nuovo Cim. C*, 036(05):35–38, 2013.

[81] A. Adare et al. Inclusive double-helicity asymmetries in neutral-pion and eta-meson production in $\vec{p}+\vec{p}$ collisions at $\sqrt{s} = 200$ GeV. *Phys. Rev. D*, 90(1):012007, 2014.

[82] S.J. Dong, J.-F. Lagae, and K.F. Liu. Flavor singlet g(A) from lattice QCD. *Phys. Rev. Lett.*, 75:2096–2099, 1995.

[83] Constantia Alexandrou, Martha Constantinou, Kyriakos Hadjiyiannakou, Karl Jansen, Christos Kallidonis, Giannis Koutsou, and Alejandro Vaquero Aviles-Casco. Nucleon axial form factors using $N_f = 2$ twisted mass fermions with a physical value of the pion mass. *Phys. Rev. D*, 96(5):054507, 2017.

[84] C. Alexandrou, M. Constantinou, K. Hadjiyiannakou, K. Jansen, C. Kallidonis, G. Koutsou, A. Vaquero Avils-Casco, and C. Wiese. Nucleon Spin and Momentum Decomposition Using Lattice QCD Simulations. *Phys. Rev. Lett.*, 119(14):142002, 2017.

[85] Huey-Wen Lin, Rajan Gupta, Boram Yoon, Yong-Chull Jang, and Tanmoy Bhattacharya. Quark contribution to the proton spin from 2+1+1-flavor lattice QCD. *Phys. Rev. D*, 98(9):094512, 2018.

[86] S. Aoki et al. FLAG Review 2019: Flavour Lattice Averaging Group (FLAG). *Eur. Phys. J. C*, 80(2):113, 2020.

[87] M. Deka et al. Lattice study of quark and glue momenta and angular momenta in the nucleon. *Phys. Rev. D*, 91(1):014505, 2015.

[88] Constantia Alexandrou, Martha Constantinou, Kyriakos Hadjiyiannakou, Karl Jansen, Haralambos Panagopoulos, and Christian Wiese. Gluon momentum fraction of the nucleon from lattice QCD. *Phys. Rev. D*, 96(5):054503, 2017.

[89] P.E. Shanahan and W. Detmold. Gluon gravitational form factors of the nucleon and the pion from lattice QCD. *Phys. Rev. D*, 99(1):014511, 2019.

[90] Yi-Bo Yang, Ming Gong, Jian Liang, Huey-Wen Lin, Keh-Fei Liu, Dimitra Pefkou, and Phiala Shanahan. Nonperturbatively renormalized glue momentum fraction at the physical pion mass from lattice QCD. *Phys. Rev. D*, 98(7):074506, 2018.

[91] C. Alexandrou, S. Bacchio, M. Constantinou, J. Finkenrath, K. Hadjiyiannakou, K. Jansen, G. Koutsou, H. Panagopoulos, and G. Spanoudes. Complete flavor decomposition of the spin and momentum fraction of the proton using lattice QCD simulations at physical pion mass. *Phys. Rev. D*, 101(9):094513, 2020.

[92] Yi-Bo Yang. A Lattice Story of Proton Spin. *PoS*, LATTICE2018:017, 2019.

[93] J.D. Bjorken. Asymptotic Sum Rules at Infinite Momentum. *Phys. Rev.*, 179:1547–1553, 1969.

[94] J.D. Bjorken and Emmanuel A. Paschos. Inelastic Electron Proton and gamma Proton Scattering, and the Structure of the Nucleon. *Phys. Rev.*, 185:1975–1982, 1969.

[95] John C. Collins. Light cone variables, rapidity and all that. 5 1997.

[96] K.G. Wilson and W. Zimmermann. Operator product expansions and composite field operators in the general framework of quantum field theory. *Commun. Math. Phys.*, 24:87–106, 1972.

[97] Xiang-Dong Ji. Breakup of hadron masses and energy - momentum tensor of QCD. *Phys. Rev. D*, 52:271–281, 1995.

[98] Stanley J. Brodsky, Dae Sung Hwang, Bo-Qiang Ma, and Ivan Schmidt. Light cone representation of the spin and orbital angular momentum of relativistic composite systems. *Nucl. Phys. B*, 593:311–335, 2001.

[99] I.Yu. Kobzarev and L.B. Okun. GRAVITATIONAL INTERACTION OF FERMIONS. *Zh. Eksp. Teor. Fiz.*, 43:1904–1909, 1962.

[100] G.Peter Lepage and Stanley J. Brodsky. Exclusive Processes in Perturbative Quantum Chromodynamics. *Phys. Rev. D*, 22:2157, 1980.

[101] Jeffrey E. Mandula and Edward Shpiz. Doubled Valued Representations of the Four-dimensional Cubic Lattice Rotation Group. *Nucl. Phys. B*, 232:180–188, 1984.

[102] M. Gockeler, R. Horsley, Ernst-Michael Ilgenfritz, H. Perlt, Paul E.L. Rakow, G. Schierholz, and A. Schiller. Lattice operators for moments of the structure functions and their transformation under the hypercubic group. *Phys. Rev. D*, 54:5705–5714, 1996.

[103] J.A. Gracey. Three loop anomalous dimension of the second moment of the transversity operator in the MS-bar and RI-prime schemes. *Nucl. Phys. B*, 667:242–260, 2003.

[104] Yi-Bo Yang, Michael Glatzmaier, Keh-Fei Liu, and Yong Zhao. The 1-loop correction of the QCD energy momentum tensor with the overlap fermion and HYP smeared Iwasaki gluon. 12 2016.

[105] Zhaofeng Liu, Ying Chen, Shao-Jing Dong, Michael Glatzmaier, Ming Gong, Anyi Li, Keh-Fei Liu, Yi-Bo Yang, and Jian-Bo Zhang. Nonperturbative renormalization of overlap quark bilinears on 2+1-flavor domain wall fermion configurations. *Phys. Rev. D*, 90(3):034505, 2014.

[106] C. Alexandrou, M. Constantinou, T. Korzec, H. Panagopoulos, and F. Stylianou. Renormalization constants for 2-twist operators in twisted mass QCD. *Phys. Rev. D*, 83:014503, 2011.

[107] Walter Wilcox. Noise methods for flavor singlet quantities. In *Interdisciplinary Workshop on Numerical Challenges in Lattice QCD*, pages 127–141, 8 1999.

[108] Yi-Bo Yang et al. Charm and strange quark masses and f_{D_s} from overlap fermions. *Phys. Rev. D*, 92(3):034517, 2015.

[109] L.A. Harland-Lang, A.D. Martin, P. Motylinski, and R.S. Thorne. Parton distributions in the LHC era: MMHT 2014 PDFs. *Eur. Phys. J. C*, 75(5):204, 2015.

[110] H. Abramowicz et al. Combination of measurements of inclusive deep inelastic $e^{\pm}p$ scattering cross sections and QCD analysis of HERA data. *Eur. Phys. J. C*, 75(12):580, 2015.

[111] A. Accardi, L.T. Brady, W. Melnitchouk, J.F. Owens, and N. Sato. Constraints on large-x parton distributions from new weak boson production and deep-inelastic scattering data. *Phys. Rev. D*, 93(11):114017, 2016.

[112] S. Alekhin, J. Blmlein, S. Moch, and R. Placakyte. Parton distribution functions, α_s, and heavy-quark masses for LHC Run II. *Phys. Rev. D*, 96(1):014011, 2017.

[113] Richard D. Ball et al. Parton distributions from high-precision collider data. *Eur. Phys. J. C*, 77(10):663, 2017.

[114] Keh-Fei Liu, Jian Liang, and Yi-Bo Yang. Variance Reduction and Cluster Decomposition. *Phys. Rev. D*, 97(3):034507, 2018.

Vita

Gen Wang

Education

- **M. S. (Physics):** University of Kentucky, KY, USA
- **B. Sc. (School of Physics, Applied Physics):** Huazhong University of Science and Technology, Wuhan, China, 2012

Publications and conference proceedings

- "Lattice Calculation of Pion Form Factor with Overlap Fermions" **Gen Wang**, J. Liang, T. Draper, K.-F. Liu, Y.-B. Yang, arXiv:2006.05431 [hep-ph]
- "Roper State from Overlap Fermions" Mingyang Sun, Ying Chen, **Gen Wang**, *et al.*, Phys. Rev. D 101, 054511 (2020), arXiv:1911.02635 [hep-ph]
- "Pion Form Factor with Overlap Fermions" **Gen Wang**, J. Liang, T. Draper, K.-F. Liu, Y.-B. Yang, arXiv:1810.12824 [hep-lat]